

國立交通大學

物理研究所

博士論文

觀察奈米結構之物理性質：

- I. 自組裝碲化鉛量子點陣列之電荷集體傳輸行為
- II. 氧化鋅摻雜鈷奈米線之鐵磁性

Probing Physical Properties in Nanostructures:

- I. Collective Transport in Self-Assembled PbSe Quantum Dot Arrays
- II. Ferromagnetism in $\text{Zn}_{1-x}\text{Co}_x\text{O}$ Nanowires

研究生：歐逸青

指導教授：簡紋濱 教授

林志忠 教授

中華民國一百年一月

觀察奈米結構之物理性質：

I. 自組裝硒化鉛量子點陣列之電荷集體傳輸行為

II. 氧化鋅摻雜鈷奈米線之鐵磁性

Probing Physical Properties in Nanostructures:

I. Collective Transport in Self-Assembled PbSe Quantum Dot Arrays

II. Ferromagnetism in $Zn_{1-x}Co_xO$ Nanowires

研究生：歐逸青

Student : Yi-Ching Ou

指導教授：簡紋濱

Advisor : Wen-Bin Jian

林志忠

Juhn-Jong Lin



A Thesis
Submitted to Institute of Physics
College of Science
National Chiao Tung University
in partial fulfillment of the Requirements
for the Degree of
Doctor
in

Physics

December 2010

Hsinchu, Taiwan

中華民國一百年一月

觀察奈米結構之物理性質：

I. 自組裝硒化鉛量子點陣列之電荷集體傳輸行為

II. 氧化鋅摻雜鈷奈米線之鐵磁性

學生：歐逸青

指導教授：簡紋濱 教授
林志忠 教授

國立交通大學物理研究所博士班

摘要

在這本論文當中，我們主要研究三個在奈米結構的物理現象。首先是硒化鉛量子點的自組裝行為，接著是硒化鉛量子點陣列中的電荷集體傳輸行為，最後一部份探討的是氧化鋅摻雜鈷奈米線中的鐵磁性。

由於溶凝膠技術的發展，科學家們可以大量地製造出尺寸為數奈米到數十奈米的半導體量子點，並以此研究奈米尺度下的各種物理現象，諸如量子侷限效應、庫倫阻滯效應、人造原子能態、以及自組裝行為。為了瞭解量子點自組裝行為的各種機制以及量子點間由於相互耦合所產生的集體效應，我們利用一種簡單的方法來製造二維量子點島嶼。此方法僅須將含有量子點的溶液滴在預先加熱好的基板上，待溶劑揮發後，量子點即自組裝而形成各種大小的二維島嶼。觀察二維島嶼的島嶼密度和溫度及覆蓋度的關係，我們可研究各種島嶼成長的機制，包括 spinodal 相分離、尺度函數及擴散限制聚集。將實驗的統計數據和各種成長的理論進行擬合後，可以推算出量子點間相互之間的鍵結能和形成穩定核種的臨界尺寸，並且決定出各種成長圖形在相圖中的位置。經由控制基板的溫度和溶液的濃度，我們可以在 spinodal 分解和擴散限制聚集兩種機制之間相互調制而產生出不同形貌的二維量子點島嶼。這兩種機制的相互作用使得 spinodal 圖形的特徵波長和碎形島嶼的維度發生變化。我們利用上述的方法在石墨和金的平面上製造出各種大小和形狀的二維自組裝量子點島嶼。

二維或三維量子點陣列的電性傳輸行為至今仍是一個熱門的主題。有許多的理論工作在討論量子點陣列當中的庫倫作用力和集體庫倫阻滯的現象，而相關的實驗工作也同時在進行，特別是針對半導體量子點。為了研究陣列當中量子點相互的耦合作用，我們在金的平面上製造出不同大小的二維硒化鉛量子點陣列，再利用掃描穿隧電流顯微鏡量測室溫及液態氮溫度下的穿隧電流能譜。我們首先利用雙穿隧接面模型對各種大小陣列的穿隧電流能譜進行擬合，並且求得量子點陣列和基板之間的等效電容。結果顯示此等效電容並不隨著陣列的大小而成正比的增加，以此整個陣列並不能被視為一個整體導電的島嶼。我們計算了探針和陣列之間、陣列和基板之間以及在陣列當中兩子點相互之間的電容，發現可以用集體傳輸的理論對電壓-電流曲線進行分析。電流曲線隨著電壓呈現指數的變化，並且此指數會隨陣列的尺寸增加，顯示量子點彼此之間具有電容式耦合。

在氧化鋅摻雜鈷奈米線中的鐵磁性的主題中，我們利用氣相傳輸法製備出各種不同尺寸的氧化鋅奈米線，其直徑可由奈米金催化顆粒的大小來控制。接著以離子佈植法將鈷離子摻雜入奈米線而形成稀磁性半導體奈米線，並利用掃描式電子顯微鏡及穿透式電子顯微鏡觀察奈米線的外觀形貌及內部的晶格結構，再以超導量子干涉儀進行磁性的量測。摻雜鈷後的奈米線呈現微弱的鐵磁性，而且飽和磁化量和矯頑力隨著奈米線的直徑而增加。在經過真空環境下的退火處理後，氧化鋅摻雜鈷奈米線呈現出明顯的室溫鐵磁性，由穿透式電子顯微鏡的影像顯示此鐵磁性並非來自於鈷的金屬團簇。我們進一步發現真空退火處理對較細的奈米線會有較大的鐵磁增強效果。另外，由零場冷卻和帶場冷卻磁化率曲線的分歧以及隨溫度變化的矯頑力等現象顯示此奈米線具有超順磁的特性亦即表示單磁疇的存在。我們推測此奈米線鐵磁性的來源是由於真空退火所產生的氧空缺將奈米線中的鈷離子耦合起來而產生。利用磁力顯微鏡對單一的奈米線進行觀察，我們發現奈米線的磁疇結構分為橫向磁化及縱向磁化兩種。而單一奈米線的磁化強度可由雙磁偶極模型估算出。

Probing Physical Properties in Nanostructures:

I. Collective Transport in Self-Assembled PbSe Quantum Dot Arrays

II. Ferromagnetism in $\text{Zn}_{1-x}\text{Co}_x\text{O}$ Nanowires

Student : Yi-Ching Ou

Advisor : Prof. Wen-Bin Jian
Prof. Juhn-Jong Lin

Institute of Physics
National Chiao Tung University

Abstract

In the thesis we study three physical phenomena in nanostructures: self-assembly of PbSe quantum dot array, collective transport in PbSe quantum dot arrays, and ferromagnetism in $\text{Zn}_{1-x}\text{Co}_x\text{O}$ nanowires.

Semiconductor quantum dots with diameters of several to tens of nanometers have been largely synthesized through colloidal techniques for nanoscience exploration of quantum confinement, Coulomb staircase, and artificial-atom states in individual quantum dots and self-assembling growth behavior. To learn about the underlying physics of self-assembly, growth mechanisms, and coupling-induced collective properties, here we report a facile way of preparing nanocrystal-assembled 2D islands by drop-casting nanocrystal suspension on a hot substrate. Growth mechanisms such as scaling function, spinodal decomposition phase separation, and diffusion-limited aggregation are investigated based on the observation of quasi-monolayer coverage. After a curve fitting to several theoretical growth models, the pair bond (interaction) energy, critical nucleus size, and the phase of growth

patterns were determined. Moreover, by heating the substrate and controlling the concentration of nanocrystal suspension, the spinodal decomposition and diffusion-limited aggregation can be tuned to modulate growth patterns of 2D nanocrystal islands. The interplay of these two mechanisms results in a variation of wavelength in spinodal growth patterns and of fractal pattern dimensions. By using this experimental approach, various sizes and shapes of nanocrystal-assembled 2D islands can be deposited on a flat surface of either graphite or gold.

Although charge transport of three-dimensional quantum dot arrays has been attempted for study on the micron scale, the electrical properties of a nanoscale array, self-assembled from a single quantum dot through a bottom-up procedure, have not been explored yet. Inter-dot Coulomb interactions and collective Coulomb blockade were theoretically argued to be a newly important topic, and experimentally identified in semiconductor quantum dots. To study the interdot coupling, we control growth parameters to self-assemble different sizes of PbSe quantum dot arrays on flat gold surface for scanning tunneling spectroscopy measurements at both room and liquid-nitrogen temperatures. The current-voltage curves of the arrays are analyzed using a double-barrier tunnel junction model to acquire the shunt capacitance between the array and the gold substrate. The increment of this capacitance is small as the particle number increases extremely from 1 to 80. Thus the array cannot be taken as a simple semiconductor island. The tip-to-array, array-to-substrate, and interdot capacitances are evaluated and the tunneling spectra of quantum-dot arrays are analyzed by the theory of collective Coulomb blockade. The current-voltage of PbSe quantum-dot arrays conforms properly to a scaling power law function. The dependence of tunneling spectra on the sizes (numbers of quantum dots) of arrays is reported and the capacitive coupling between quantum dots in the arrays is explored.

In the topic of ferromagnetism in $Zn_{1-x}Co_xO$ nanowires, diameter controllable ZnO nanowires have been fabricated by thermal evaporation (vapor transport) with various sizes of gold nanoparticles as catalysts. Diluted magnetic semiconductor (DMS) $Zn_{1-x}Co_xO$ nanowires were then made by high energy Co ion implantation. The morphology and crystal structure of the nanowires were inspected by use of scanning and transmission electron microscopes. Magnetic properties of the $Zn_{1-x}Co_xO$ nanowires were measured by employing a SQUID magnetometer. The as-implanted $Zn_{1-x}Co_xO$ nanowires displayed weak ferromagnetism and size dependent behavior has been observed in the magnetic field and temperature dependences of magnetization. The shrinkage of the nanowire diameter reduced the spontaneous magnetization as well as the hysteresis loops. After high-vacuum annealing, $Zn_{1-x}Co_xO$ nanowires exhibited strong ferromagnetic ordering at room temperature. Electron microscopy analysis was used to ensure the absence of Co nanocrystals in the annealed nanowires. The effect of annealing on the creation of a strong ferromagnetic state is much more pronounced in thinner nanowires. From field cooled and zero-field cooled magnetization and coercivity measurements between 2 and 300 K, superparamagnetic features were observed in the $Zn_{1-x}Co_xO$ nanowires. We argue that the generation of point defects by vacuum annealing is the origin for the enhanced ferromagnetism in the $Zn_{1-x}Co_xO$ nanowires. We employed magnetic force microscopy to verify the ferromagnetism in individual $Zn_{1-x}Co_xO$ nanowires. Two kinds of domain structure, transverse and longitudinal, were observed in ferromagnetic nanowires and the magnetic dipole moment of individual nanowires was estimated by fitting to a two magnetic point dipole moment model.

Acknowledgement

取得博士學位是我人生的一個里程碑，我首先必須感謝我的指導教授簡紋濱老師，在我碩士班至博士班這六年多的時間裡，他所給予的指導、督促、鼓勵，以及提供一份足以維持簡單生活的薪水，我由衷的感激。也必須感謝林志忠教授無私的提供良好的實驗環境及儀器設備讓我能完成學位。另外我要感謝一路上幫我釋疑解惑的林永翰博士、葉勝玄博士、邱劭斌博士、吳忠益博士、林彥甫博士，以及眾多無法一一列出的實驗室夥伴。感謝林登松老師、林俊源老師、鄭舜仁老師、羅榮立老師能夠擔任我的口試委員，給予我批評與指教。

這本論文是我研究所這幾年來工作的集結，除了簡老師的指導外，還有歷屆碩士班同學的努力付出才得以完成。在量子點自組裝的部份，我要感謝廖泰慶、侯朝振和紀彥羽。在掃描穿隧電流顯微鏡的工作，我要感謝郭融學、吳俊吉、鄭淞芳和莊維倫。在氧化鋅奈米線磁性量測的部份，我必須感謝陳怡然、曾祥一和陳昶廷，以及宋竹芸在磁力顯微鏡方面的工作。

感謝吾友江森正先生在我工作低潮時給予我安慰並讓我一圓埃及旅遊的夢想。最後，感謝我的爸爸、哥哥、嫂嫂及所有家人，您們的鼓勵與關懷是我最重要的動力。

Contents

摘要.....	i
Abstract.....	iii
Acknowledgement.....	vi
Contents.....	vii
List of Figures.....	ix
Chapter 1 Introduction.....	1
1.1 Overview.....	1
1.2 Outline of work.....	5
Chapter 2 Self-assembly of PbSe quantum dot arrays.....	7
2.1 Introduction.....	7
2.2 Theoretical background.....	10
2.2.1 Phase diagram and phase separation.....	10
2.2.2 Scaling theory.....	12
2.2.3 Diffusion-limited aggregation and fractal dimension.....	13
2.3 Experiment.....	15
2.4 Results and discussion.....	17
2.4.1 Growth pattern and phase diagram.....	19
2.4.2 Growth mechanisms.....	25
Chapter 3 Collective transport in PbSe quantum dot arrays.....	33
3.1 Introduction.....	33
3.2 Theoretical background.....	35
3.2.1 Coulomb blockade and double tunnel junction model.....	35
3.2.2 Collective transport: MW model.....	39
3.3 Experiment.....	42
3.4 Results and discussion.....	44
3.4.1 Double tunnel junction model.....	46
3.4.2 MW model.....	50
Chapter 4 Ferromagnetism in $Zn_{1-x}Co_xO$ nanowires.....	56
4.1 Introduction.....	56
4.2 Theoretical background.....	59
4.2.1 Ferromagnetism in diluted magnetic semiconductor.....	60
4.2.2 Superparamagnetism.....	62
4.2.3 Magnetic force microscopy.....	64
4.3 Experiment.....	65

4.4	Results and discussion	67
4.4.1	Growth behavior and chemical composition	68
4.4.2	Annealing effects on magnetic properties.....	74
4.4.3	Characterization of magnetic domains by MFM	84
Chapter 5	Conclusion	91
Reference	94
Curriculum vitae	103



List of Figures

- Figure 2.1:** (a) The two-dimensional Lennard-Jones phase diagram showing fluid(F), gas(G), liquid(L), solid(S), and coexistence phases. The dashed line in gas-liquid coexistence phase separates metastable and unstable regions. (b) The free energy versus concentration with $\partial^2 G/\partial c^2 < 0$. The mean free energy (gray circle) of two compositions (hollow circle) after phase separation is less than the free energy before phase separation (black circle). **11**
- Figure 2.2:** (a) Analytic form of Eq. (2.3) for the scaled island-size distribution for $i = 1$ to 3. (b) A typical aggregation of WS DLA model showing a fractal-like structure. The black circle represents the seed particle in the origin. **14**
- Figure 2.3:** (a) TEM image of PbSe QDs. (b) High-resolution TEM image of an individual PbSe QD. (c) Statistical distribution of QD sizes and a red curve fitted with Gaussian function. **18**
- Figure 2.4:** SEM images of PbSe QD patterns grown at substrate temperatures of 100°C (a-d), 50°C (e-g), and 180°C (h-j). The QD coverage is (a) 30%, (b) 13%, (c) 66%, (d) 90%, (e) 4%, (f) 41%, (g) 68%, (h) 6%, (i) 20%, and (j) 61%. **20**
- Figure 2.5:** (a) Island density as a function of QD coverage grown at various different temperatures indicated on graph. (b) Phase diagram of a 2D Lennard-Jones system, reproduced from refs 14 and 67. The symbols, a-g, point to the growth conditions of the patterns shown in Figure 2.2. The dotted line indicates the boiling point (110.6°C) of the toluene solvent. **24**
- Figure 2.6:** Occurrence as a function of aggregation number (n , number of QDs) corresponding to small islands with 3-9 QDs at (a) 50, (b) 100, and (c) 180°C. The solid lines present the fitting results. Scaled island size distributions at (d) 70, (e) 100, and (f) 130°C. The coverage are (d) 4, (e) 13, and (f) 16%. The dashed lines are guides to eyes. The solid line in Figure (e) represents the scaling function corresponding to a critical nucleus size $n = 1$ and a stable cluster size $n \geq 2$ **27**
- Figure 2.7:** (a) SEM image of a spinodal pattern grown with coverage of ~38% at 100°C. (b) SEM image of a spinodal pattern grown with coverage of 45% at 50°C. The insets show fast-Fourier-transformed and radial

averaged intensity as a function of inverse wavelength. (c) Wavelength at maximum intensity, estimated from the intensity distribution, like the inserts of parts (a) and (b), for QD growth with coverage of ~42% and at different temperatures.30

Figure 2.8: Gyration radius, R_g , has a power law dependence on the aggregation number, n , in double logarithm scales for QD growth at (a) 100°C and (b) 180°C with coverage of 21% and 18%, respectively. Corresponding SEM images are displayed in the insets. Schemes of (c) cluster diffusion and d) single-particle diffusion models.....32

Figure 3.1: Schematic diagram of an STM geometry which is modeled as a double tunnel junction system. The two junctions of capacitances C_1 and C_2 , and resistances R_1 and R_2 , are driven by a voltage source V37

Figure 3.2: (a) A schematic illustrating the build of charges in a one-dimensional array as the voltage is progressively increased to threshold. (b) A scheme of branched channel in a $N \times N$ two-dimensional array.....41

Figure 3.3: (a) STM image of PbSe QD arrays dispersing on a gold surface. (b) A two-dimensional PbSe QD array with 229 QDs on the Au(111) surface. (c) Radially averaged intensity of the two-dimensional Fourier transformed image displayed in the inset.....45

Figure 3.4: $I-V$ curve of the single PbSe QD on the gold surface. The open circles denote experimental data, and the red line gives the best fit to the orthodox theory. The insert gives a scheme of a tip and an STM image ($44 \times 44 \text{ nm}^2$) showing the single PbSe QD on which the $I-V$ curve is taken. A circuit diagram is shown in the insert as well.47

Figure 3.5: Shunt capacitances C_1 and C_2 (a) and resistances R_1 and R_2 (b), estimated from fittings with the orthodox theory, revealing a dependence on the number of QDs. The approaching lines only give a guide to the eye.49

Figure 3.6: (a) Schematic illustration of the model of collective transport. The spheres denote PbSe QDs. The black and gray thin lines indicate the interdot and dot-to-substrate capacitances, respectively. The dashed thick lines with arrows illustrate electron transport (b) The $I-V$ curve of an array consisting of 43 PbSe QDs. The inset displays its STM topography image with a 50 nm scale bar. (c) Experimental data (open circles) and a fitting curve (solid line) according to the indicative power law function. The nonlinear least square fitting gives the parameters of the threshold voltage and the scaling exponent designated in the inset.51

Figure 3.7: Threshold voltages V_{th} ((a) and (c)) and scaling exponents ζ ((b) and (d)) as a function of the QD number. The data in (a) and (b) ((c) and (d)) are

estimated from fitting to $I-V$ curves taken at room temperature (78 K). The solid lines in (a) and (b) give the best linear least square fits to our data.54

Figure 4.1: The schematic diagram of bound magnetic polaron in ZnO doped with Co ions. The white circles represent Zn atom. Co ions are represented by red circles with an arrow representing a magnetic moment. The rectangles represent the oxygen vacancies which donate excess electron to form hydrogenic orbitals, which is represented by large blue circles.61

Figure 4.2: The typical FC-ZFC curve of a superparamagnetic system with Lambda shape. The branch point of the curve indicates the blocking temperature.63

Figure 4.3: The schematic for modeling the tip and sample as two point magnetic dipoles. The origin of this coordinate is at the center of sample.63

Figure 4.4: FESEM images of as-grown ZnO NWs with average diameters of (a) 12 nm, (b) 19 nm, (c) 38 nm, and (d) 113 nm. The corresponding statistical distributions are (e), (f), (g), and (h).69

Figure 4.5: (a) High resolution TEM image of an as-grown ZnO NW with the diameter of 10 nm. The inset shows its corresponding nano beam electron diffraction pattern. High resolution TEM images of (b) as-implanted and (c) high-vacuum annealed $Zn_{1-x}Co_xO$ NWs. The inset in (b) and (c) displays corresponding electron diffraction patterns. (d) TEM image of a ZnO NW sheathed in carbon amorphous with Co clusters after high-vacuum annealing. The inset of (d) is the statistical distribution of Co-cluster diameters estimated from TEM images. The average diameter and standard deviation are 9.4 and 6.0 nm, respectively.71

Figure 4.6: Bright-field image with compositional EELS mapping of the Co L, O K, and Zn L edges of the high-vacuum annealed $Zn_{0.92}Co_{0.08}O$ nanowires with an average diameter of 38 nm.73

Figure 4.7: (a) FC and ZFC behaviors of temperature dependent magnetization of as-implanted $Zn_{0.92}Co_{0.08}O$ NWs with average diameters of 10, 20, and 40 nm. (b) FC and ZFC magnetizations of as-implanted and high-vacuum annealed $Zn_{0.92}Co_{0.08}O$ NWs with an average diameter of 40 nm. The annealing time is 12 h.75

Figure 4.8: (a) Hysteresis loops of as-implanted $Zn_{0.92}Co_{0.08}O$ NWs with three different average diameters marked on graph. The data were taken at 5 K. (b) Hysteresis loops of as-implanted $Zn_{0.96}Co_{0.04}O$ NWs with two different average diameters marked on graph. The data were taken at 2 K.

.....	77
Figure 4.9: (a) Hysteresis loops, taken at 10 K, of as-implanted, 6-h vacuum annealed, and 12-h vacuum annealed $Zn_{0.92}Co_{0.08}O$ NWs with a 38-nm average diameter. (b) Hysteresis loops, taken at 2 K, of as-implanted, 3-h vacuum annealed, and 6-h vacuum annealed $Zn_{0.92}Co_{0.08}O$ NWs with a 19-nm average diameter. (c) Hysteresis loops, taken at 300 K, of as-implanted, 12-h vacuum annealed, 6-h oxygen annealed, and 6-h vacuum annealed $Zn_{0.92}Co_{0.08}O$ NWs with a 100-nm average diameter.	79
Figure 4.10: (a) Hysteresis loops of $Zn_{0.92}Co_{0.08}O$ NWs with (a) 38-nm and (c) 19-nm average diameter at several temperatures after annealing in a high vacuum for 6 h and 3 h, respectively. (b) and (d) are the coercive field, estimated from Fig. 13(a) and Fig. 13(c) respectively, as a function of square root of temperature.	81
Figure 4.11: (a) FC and ZFC magnetization of ZnO sheathed in amorphous carbon with Co clusters. The Co ion dose and average diameter of ZnO are $4 \times 10^{16} \text{ cm}^{-2}$ and 38 nm, respectively, for this sample. (b) Hysteresis loops of ZnO sheathed in amorphous carbon with Co clusters. The inset shows the coercive field as a function of square root of temperature.....	83
Figure 4.12: MFM images of (b) non-ferromagnetic, (d) longitudinally magnetized, and (f) transversely magnetized NWs with their simultaneous AFM images (a), (c), and (e). (h) Topographic (black line) and phase signal (red dot) profiles of (e) and (f) with fitting curve (red line). (g) Schematic for modeling the origin of the ferromagnetism in $Zn_{1-x}Co_xO$ NWs and their relative orientation of magnetization between a transverse single-domain and a MFM tip. (i) Calculated magnetic dipole moment of NWs as a function of their size. (j) Phase difference of MFM data as a function of NW diameter.	85
Figure 4.13: Successive magnetization reversal of a 50 nm diameter $Zn_{0.89}Co_{0.11}O$ NWs resulted from continuous scanning by a magnetic tip, in order of (a), (b), (c), and (d). MFM images of longitudinally magnetized NWs (e) before and (f) after applying a field by a magnet and the white arrows indicate the place where the bright-dark contrasts change.	88
Figure 4.14: MFM images of $Zn_{0.89}Co_{0.11}O$ a NW (b) before and after heating up to (c) 373 K and (d) 673 K. (e) Phase difference of MFM data of an individual $Zn_{0.89}Co_{0.11}O$ NW as a function of heating temperature. (f) Phase difference of MFM data of different transversely magnetized NWs represented as black squares and a longitudinally magnetized NW represented as red circles.	90

Chapter 1

Introduction

1.1 Overview

Nanostructure can be defined as the structure with at least one dimension that is on the nanometer length scale and with its properties influenced by quantum confinement effect. The emergence of confinement effect results in a transitional electronic structure which differs from the discrete states in atom and the continuous band in bulk. The unusual electronic structure and high surface-to-volume ratio of nanostructures make a dramatic change in their physical properties and provide a potential route for application. For example, while gold is noble metal, its nanoparticle is a kind of active catalyst which is widely applied nowadays. The intense interest in nanostructure is motivated not only for its extensive potential application but also for the intriguingly special phenomenon, such as quantum confinement and Coulomb blockade, exhibited in nanometer scale. With the help of various kinds of technology and instruments, including scanning probe microscope, scanning electron microscope, transmission electron microscopy, and e-beam lithography, we can directly observe the dimension and morphology of nanostructures and investigate their novel properties.

Usually the nanostructures with quantized electronic structure in all three spatial dimensions are called “quantum dots (QDs). For the analogy with the quantized states of an atom, the QDs are also termed as “artificial atoms” [1]. If a QD is viewed as “artificial atom”, then a superlattice of QDs can be viewed as an “quantum dot solid” or “artificial solid”. In recent years, “quantum dot (QD) solids” formed by closed-packed two- and three-dimensional arrays of monodispersed metallic or semiconductor nanocrystals have provided opportunities for fabricating novel materials. The coupled nanocrystals within QD solids exhibit collective properties which enable the application on electronics and optoelectronics [2-5]. Manufacturing of QD solids merely needs to drop the suspension of nanocrystals on a substrate, and therefore it is much easier and cheaper than the traditional lithographic devices. The process that nanocrystals in the suspension were spontaneously formed closed-packed arrays is usually referred as “self-assembly”.

Based on self-assembly, there are many different methods have been employed to fabricate colloidal, especially for two-dimensional, QD arrays [6-11]. In those methods, the solvent properties, i.e. surface tension, evaporation rate, and convection, are dominated factors and the self-assembly takes place before the solvent dries out from the substrate. In addition, the interaction between QDs and the substrate also plays an important role on self-assembly. In atomistic thin film growth process, competition of binding energy between atom-to-atom and atom-to-substrate determines three growth modes, island, layer, or layer plus island [12]. Since QDs are regarded as artificial atoms, it is reasonable to expect the similar behavior in the growth of QD solids. In QD assemblies, van der Waals force provides the binding energy to determine the structure of the quantum dot solids. A phase diagram of two-dimensional Lennard Jones particle system has been adopted to describe the two-dimensional QD system [13,14]. For different coverage and binding energy

between QDs, a two-dimensional QD system exhibits specific phase, and the QD assembly in each phase has distinct morphology. We can obtain ordered, disordered, large, small, separated or continuous two-dimensional QD islands when the system is situated in different phases.

The colloidal synthesis as a bottom-up approach has been employed to fabricate quantum dots (QDs) in different materials [15]. The QDs can be considered as an artificial atom because of their discrete electronic structure, which is resulted from the quantum confinement effects and dependent on their size [16]. Experimentally, the discrete electronic structure was observed in some kinds of isolated semiconductor QDs with the scanning tunneling microscopy (STM) at low temperature [17-20]. The narrow size distribution facilitates the QDs to constitute closed-packed two- and three-dimensional QD solids through self-assembly for application to novel optoelectronic and electronic devices. The electronic properties of the QD solids were strongly influenced by inter-dot spacing, coupling strength between QDs, and charging energy. Tuning the inter-dot spacing, the metal-insulator transition was observed by optical and STM measurements in quantum solids of silver QDs [21, 22]. In semiconductor QD solids, the delocalization of electron and hole giving rise to the coupling of the QDs was also measured by STM [23, 24].

At high temperatures, at which quantum effects are totally destroyed by thermal fluctuation, QD solids could exhibit either an electron hopping or a thermally activated transport [25, 26]. The collective behavior of electrons in the Coulomb blockade region has been experimentally demonstrated in systems of 2DEG QD [27], and of metal island [28], arrays. In addition, Middleton and Wingreen [29] proposed a model (MW model) to describe collective transport in arrays of small metallic dots in the Coulomb blockade region. They suggested a stray field to induce different polarization charges in QDs and to render a quenched disorder. The disorder leads to

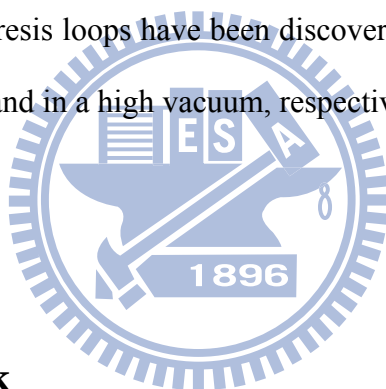
a threshold voltage V_{th} below which the current is suppressed. At voltages well above V_{th} , they predicted that the current through the QD array will behave as a power law function of a reduced voltage $(V/V_{th} - 1)$ with a scaling exponent ζ . They calculated the dependence of V_{th} and ζ on the dimension of, and the inter-dot coupling in, the array. Recently, collective transport in the Coulomb blockade region has been experimentally inspected in quasi-one-dimensional wires [30, 31], two-dimensional films [2, 32], and three-dimensional solids [33, 34] self-assembled by colloidal QDs.

As for the magnetism properties in nanostructures, diluted magnetic semiconductors (DMS) are believed to be promising candidate materials for emerging applications in spintransfer electronics (spintronics) [35, 36] and nanomagnetic devices. Among all the characteristics of DMS, a high Curie temperature ensuring room-temperature ferromagnetism (RTFM) is the most important feature for the development of practical devices. The existence of RTFM has been argued in both p-type and n-type ZnO host materials with transition metal impurities [37, 38]. These theoretical concepts and arguments for RTFM have recently been sustained by several experiments, [39, 40] especially with the ZnO-based DMS, which has attracted much attention.

Due both to a large magnetic moment per 3d dopant [41] and to the stability of the ferromagnetic state with electron doping, [38] which reconciles with the intrinsic n-type nature of ZnO, the magnetic properties of $Zn_{1-x}Co_xO$ have recently been intensely studied. Ueda et al. [39] and several other groups [42, 43] have demonstrated RTFM in $Zn_{1-x}Co_xO$, while other groups reported either the absence of ferromagnetism or even the presence of paramagnetism [44] or antiferromagnetism [45, 46] in this material. There are also authors who argued for extrinsic ferromagnetism resulting from second phases of Co clusters or nanocrystals [47, 48]. Indeed, a full understanding of the magnetic properties and the mechanism of

ferromagnetism in $Zn_{1-x}Co_xO$ is still lacking. Jian et al. have experimentally demonstrated that planar and point defects in ZnO can strongly affect the magnetic properties of $Zn_{1-x}Co_xO$ [49, 50]. Either zinc interstitials [43, 51] or oxygen vacancies [50, 52, 53] have been proposed to play crucial roles on inducing intrinsic RTFM in this material. A bound magnetic polaron model [54] is thought to likely provide an explanation for RTFM as well.

Quasi-one-dimensional nanostructures (e.g., nanorods and nanowires) are basic building blocks for nanoscale electronics. Among them, $Zn_{1-x}Co_xO$ nanowires are potentially useful in spintronic and possibly other applications. Recently, a weak magnetic state displaying noticeable hysteresis loops and an enhanced ferromagnetic state displaying large hysteresis loops have been discovered at a low temperature of 2 K after annealing in argon and in a high vacuum, respectively [49].



1.2 Outline of work

The thesis is organized as follows. At first mechanisms of self-assembly of PbSe QDs on a HOPG substrate at different temperatures is investigated and described in chapter 2. Based on the results of chapter 2, we prepared two-dimensional QD arrays with desired sizes on gold substrates by adjusting the self-assembly conditions. We used scanning tunneling microscopy to observe the electron transport in these QD arrays and found the capacitive coupling among QDs resulted in a collective transport behavior. The results are presented in chapter 3. In chapter 4, we switch our samples to ZnO nanowires and study their magnetic properties. After implanting Co ions and thermal treatment, ZnCoO nanowires exhibit RTFM and the magnetization depends

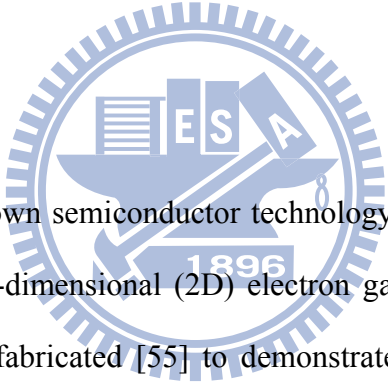
on their size. Magnetic force microscopy was employed to directly observe magnetic domains in individual nanowires at room temperatures. In chapter 5, we give our conclusion.



Chapter 2

Self-assembly of PbSe quantum dot arrays

2.1 Introduction



With the help of the top-down semiconductor technology, lithography, to reduce the lateral dimension of a two-dimensional (2D) electron gas, the quantum dots (QDs) have been experimentally fabricated [55] to demonstrate their atomic-like physical properties which have been introduced in theory for a long time [56]. Later on, a colloidal synthesis strategy [15] has been developed to fabricate QDs (or nanocrystals) which have been examined to show artificial atom features in optical properties [4], magnetic properties due to orbital electrons [58], and electronic structures [17]. Bearing a resemblance to atomic combination of forming a periodic crystal structure in a solid, these colloidal QDs and metal nanoparticles are able to self-organize to form either two- or three-dimensional superlattices [59-61]. Thus, collective physical phenomena were proposed in theory and investigated in the QD-assembled superlattices. Recently, Ge and Brus illuminated that a system of 2D QD self-assembly can be suitably described by a 2D Lennard-Jones model which may

consist of two coexisting phases, resulting in a spinodal phase separation [13]. The same group (Brus's group) also demonstrated nucleation and growth behaviors [14], and solvent-drying mediated self-assemblies of QDs at room temperature [62]. On the other hand, Jaeger's group reported their study aimed to a formation of long-range-ordered self-assembly [63] and a highly ordered QD monolayer [7]. More excitingly, binary nanocrystal superlattices [64], coarsening [65], and nanopatterning by moulding [66] in QD formed superlattices have recently been conducted in experiments.

Theoretically, molecular-dynamic calculations of 2D Lennard-Jones model were applied to simulations of physisorbed systems, such as rare gases on graphite, to show interesting snapshots of island morphologies, particle trajectories, or growth patterns [67, 68]. The fruitful phases of this 2D Lennard-Jones system illustrate various kinds of growth behaviors. These phases were commonly presented on the reduced temperature and coverage (ρ^* , T^*) plane. Here $\rho^* = \rho\sigma^2$ and $T^* = kT/\varepsilon$, where ρ is the particle density per unit area, σ is the hard-core diameter, k is the Boltzmann constant, T is the temperature, and ε is the pair bond energy (or the pair interaction energy). At a low coverage ($\rho^* \cong 10\%$), the critical nucleus size and the small cluster occurrences in thermal equilibrium can be learned and explored on the initial growth stage of a nucleation process [69]. In addition, the scaling function of the cluster size distribution [70, 71] can be studied. With an increase of coverage, e.g. ρ^* up to $\sim 40\%$, and at a temperature lower than the critical-point temperature of this system, a coexistence of liquid-gas or solid-gas phases should result in a spinodal decomposition of phase separation that could be obtained and recorded on microscopy images. The spinodal patterns have been discovered and observed in several systems such as quenched glass [72] and dried-up colloidal QDs [13, 14, 62] through a rapid

cooling and solvent drying processes, respectively. In these cases, it mainly focuses on diffusion-mediated motion and aggregation of the colloidal QDs.

On the other hand, in the case of colloidal QDs which are normally dispersed in a solvent, the solvent can play another important role in the growth and nucleation processes. The solvent is evaporated quickly when it is heated near its boiling point. Though the growth temperature is fixed at the boiling point, the rapid evaporation of the solvent shall lead to reduce the QD mobility on substrates and introduce an additional growth mechanism, diffusion-limited aggregation [73]. This effect could be enhanced and dominant especially when the QD assembly takes place on a substrate heated above the solvent boiling point. In previous reports [13, 14, 62], the QD assembly was carried out at a room temperature and the solvent was kept to evaporate very slowly (up to one hour). The slow evaporation rate of the solvent drives a variation of the pair bond energy between QDs and a change of state from a high to a low reduced temperature. Unlike Brus's experiments [13, 14, 62], we attempt to study the temperature effect on the (ρ^*, T^*) plane. By heating the substrate, the temperature dependence of growth behavior as well as the phase diagram of the colloidal QD system should exhibit. In this work, the solvent was evaporated rapidly (less than one minute) and the growth process can be quenched at such a high temperature. Thus, we can study the growth pattern at a fixed state, rather than transition states at different reduced temperatures. Other than an investigation on long-rang ordered QD film, we concentrated our study on growth mechanisms of the spinodal decomposition and the diffusion-limited aggregation, and their application to syntheses of 2D QD islands. The QD-assembled 2D islands can be adopted as an approach to study collective properties in mesoscopic physics.

2.2 Theoretical background

In this section, we briefly introduce phase separation, scaling theory, and diffusion-limited aggregation which are applied to analyze our results at different coverages and temperatures.

2.2.1 Phase diagram and phase separation

Two-dimensional Lennard-Jones particle system was investigated for modeling the behavior of rare gas atoms adsorbed on basal planes [80]. The particles in the system interact by the Lennard-Jones potential

$$\phi(r) = 4\varepsilon \left[\left(\frac{\sigma}{r} \right)^{12} - \left(\frac{\sigma}{r} \right)^6 \right], \quad (2.1)$$

where r is the distance between two particles, ε is the pair interaction energy, and σ is the hard-core diameter. Phase diagrams for the two-dimensional Lennard-Jones system were constructed by Monte Carlo simulation. In phase diagrams, the particle system exhibits different phases for specific thermodynamic states, *i.e.* pressure, density, and temperature. Fig. 2.1(a) shows a phase diagram in the (ρ^*, T^*) plane, where $\rho^* = \rho\sigma^2$ is the density (coverage) and $T^* = k_B T / \varepsilon$ is the reduced temperature, with regions of fluid(F), gas(G), liquid(L), solid(S), and coexistence [67]. With a mediate coverage, the decreasing temperature (T^*) gives raise to a phase separation that makes the system transits from the fluid phase to the gas-liquid coexistence phase.

As a homogeneous binary system decomposes into two regions of different

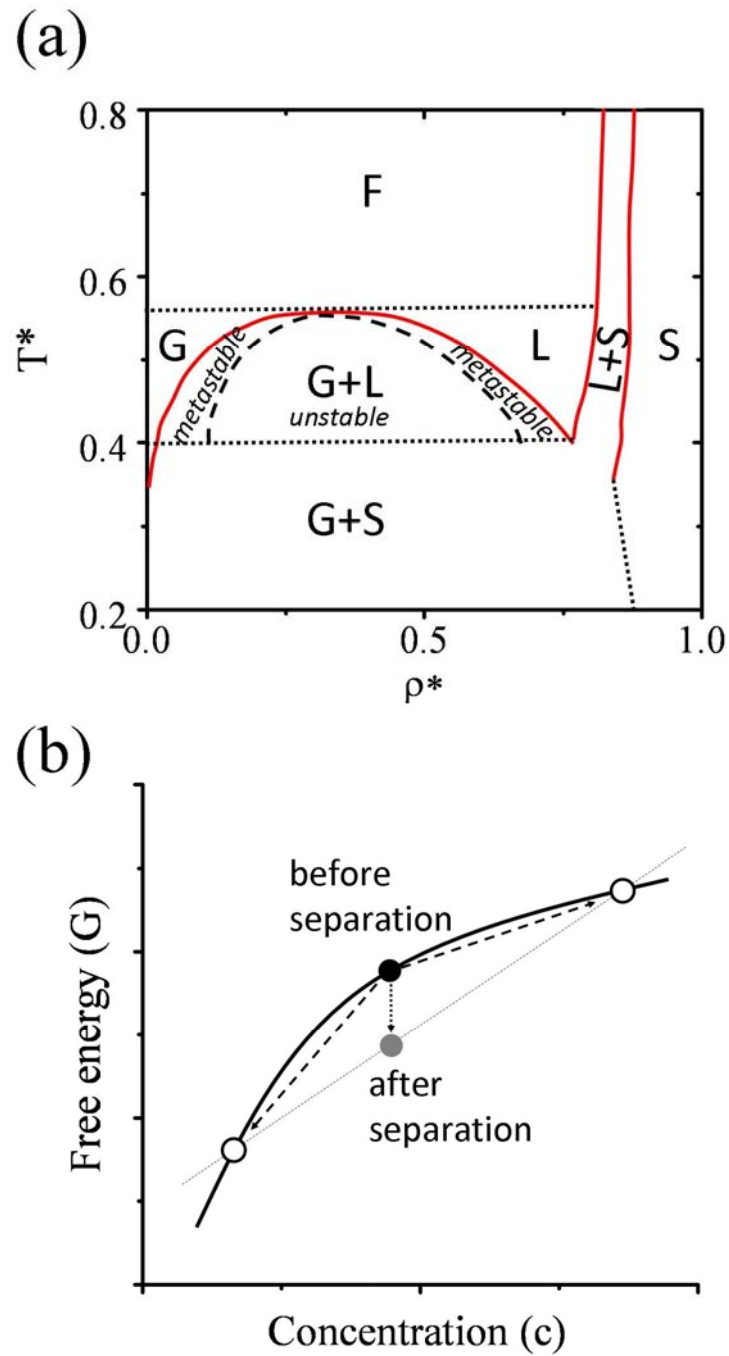


Figure 2.1: (a) The two-dimensional Lennard-Jones phase diagram, reproduced from refs 14 and 67, showing fluid(F), gas(G), liquid(L), solid(S), and coexistence phases. The dashed line in gas-liquid coexistence phase separates metastable and unstable regions. (b) The free energy versus concentration with $\partial^2 G / \partial c^2 < 0$. The mean free energy (gray circle) of two compositions (hollow circle) after phase separation is less than the free energy before phase separation (black circle).

compositions by phase separation, there are two possible mechanisms. When the binary system is situated at a state that the secondary derivative of free energy with respect to concentration is minus, *i.e.* $\partial^2 G / \partial c^2 < 0$, the average free energy of each composition after phase separation will be lower than that before separation, as shown in Fig. 2.1(b). Thus the system is unstable and the phase separation will take place spontaneously to lower down the total free energy. This mechanism of phase separation is called spinodal decomposition [72]. Phase separation by spinodal decomposition is a long-range behavior with an onset of infinitesimal fluctuation. The system eventually forms a labyrinth pattern which possesses a correlation wavelength and the wavelength depends on the temperature. On the other hand, if $\partial^2 G / \partial c^2 > 0$, the system is situated in a metastable region. The phase separation cannot take place until the fluctuation is large enough to overcome the barrier of free energy. This mechanism is called nucleation and growth. In this mechanism, clusters have a critical size below which the cluster is unstable and cannot exist for long time. The formed clusters must be larger than the critical size.

2.2.2 Scaling theory

In surface physics, the scaling function was studied to understand the nucleation and growth behavior of epitaxial deposition. The critical size i , which is one less than the number of atoms needed to form a stable island, is a dominant parameter for the scaling behavior. Amar and Family have proposed an analytic expression of the scaling function by which we can find out the critical size with the known island size distribution [71]. Provided an assumption that the mean island size $S(\theta)$ is the only one characteristic size, they derived a general scaling form

$$N_s(\theta) = \theta S^{-2} f_i(s/S), \quad (2.2)$$

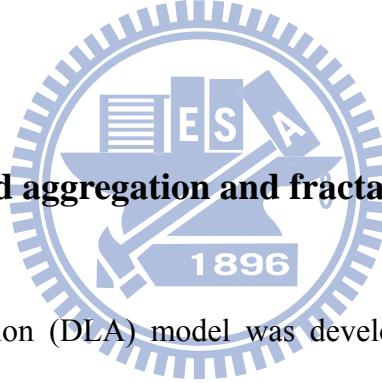
where $N_s(\theta)$ is the density of island containing s atoms at coverage θ and $f_i(s/S)$ is the scaling function which satisfies $\int_0^\infty f_i(u) du = \int_0^\infty f_i(u) u du = 1$. Based on the experimental observation, the conjectured the scaling function for $i \geq 1$

$$f_i(u) = C_i u^i \exp(-ia_i u^{1/a_i}) \quad (2.3a)$$

where C_i and a_i satisfy the expressions

$$\frac{\Gamma[(i+2)a_i]}{\Gamma[(i+1)a_i]} = (ia_i)^{a_i}, \quad \frac{(ia_i)^{(i+1)a_i}}{a_i \Gamma[(i+1)a_i]}. \quad (2.3b)$$

Fig. 2.2(a) shows each curve of analytical form of $f_i(u)$ for $i = 1, 2,$ and 3 . By matching experimental data to these curves, the critical size i can be decided.



2.2.3 Diffusion-limited aggregation and fractal dimension

Diffusion-limited aggregation (DLA) model was developed by Witten and Sander (WS) to study the formation of dendritic structures [73]. The model is started with a seed particle located at the origin of a two-dimensional lattice. Another particle is put into the lattice and walk randomly from far away until it reaches the site that is adjacent to the seed particle. Then it is stopped and another particle is put into for random walking until it reaches the occupied sites, and so forth. A typical aggregation showing a fractal-like structure is presented in Fig. 2.2(b). The particle number N and the aggregation size have the relation

$$N \sim R_g^D, \quad (2.4)$$

where R_g is the radius of gyration and D is its fractal dimension. The radius of gyration R_g is the root mean square distance between the particles and the center of

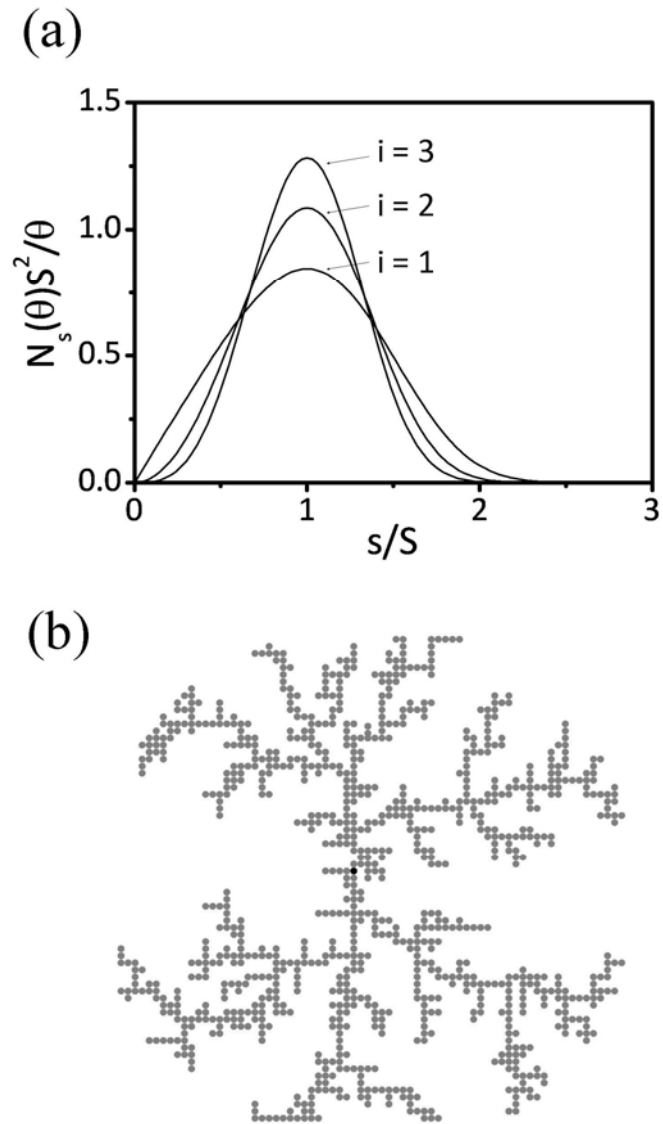



Figure 2.2: (a) Analytic form of Eq. (2.3) for the scaled island-size distribution for $i = 1$ to 3. (b) A typical aggregation of WS DLA model showing a fractal-like structure. The black circle represents the seed particle in the origin.

mass of the aggregation. The fractal dimension D can be obtained by log-log plots of R_g as a function of N . By computer simulation, they predicted the fractal dimension D of DLA is ~ 1.7 . On the basis of WS model, subsequent modifications were suggested which allow the formed aggregation to diffusion instead of being static in WS model [78, 79]. When the moving aggregations contact with each other, they merge into a larger aggregation and keep growing. These modified models were referred to cluster-cluster (CLCL) model and the fractal dimension was about 1.4-1.5 which is less than that of WS model. The models mentioned above are mainly focused on the two-dimensional case.

2.3 Experiment



PbSe QDs were prepared using a high-temperature organic solution approach by adopting a method in previous report [15]. To synthesize PbSe QDs, trioctylphosphine-selenium solution (TOP-Se, 1.0 M for Se) was prepared as Se-source by dissolving 7.90 g of selenium powder (99.99%) into 100 mL of TOP (90%) in a glovebox and stirring for overnight. In a typical experiment, 1.081 g of lead acetate trihydrate ($\text{PbAc}_2 \cdot 3\text{H}_2\text{O}$, 99.99%, 2.85 mmol), 3.6 mL of oleic acid (90%), and 15 mL of phenyl ether (>99%) were loaded into a flask and heated to 140°C for 20 min under an argon stream. After the moisture-free solution was cooled to $\sim 40^\circ\text{C}$, it was transferred into a glovebox and mixed with 5.0 mL of the TOP-Se stock solution in a syringe. This mixed solution was then rapidly injected into vigorously stirred phenyl ether (15 mL) that was preheated to 200°C in a three-neck flask equipped with a condenser under argon atmosphere. After the injection, the

temperature of the mixture dropped to $\sim 160^{\circ}\text{C}$ because of the addition of the room-temperature reagents. Once the solution temperature increased to $\sim 200^{\circ}\text{C}$ in ~ 5 min, the QD growth was terminated by an immediate removal of the heating source. A size-selective precipitation [74, 75] was subsequently performed by centrifugation using a pair of solvents consisting of anhydrous hexane (98.5%, BDH) and anhydrous ethanol (200 proof, AAPER). Before the size-selection, the QD average size can also be roughly tuned by varying the QD growth temperature [15] after the injection of the reagents into the hot phenyl ether because raising the solution temperature accelerates the QD growth rate. Solution temperature between 150 and 220°C was usually chosen to grow the QDs in the desired range of size. The resultant PbSe QDs were identified using various characterizations including X-ray diffraction study, inductively coupled plasma analysis, transmission electron microscope (TEM, JEOL JEM-2010F) imaging, and energy dispersive spectroscopy evaluation. These PbSe QDs generally present in a spherical shape. However, some cubic particles could be detected when the QDs were grown at a temperature of 200°C or higher. All of the chemicals mentioned above were purchased from Sigma-Aldrich and used as received, except those specified.

The as-synthesized PbSe QDs were stored by dispersing them in toluene. At least three drops of the QD suspension were put on a graphite substrate, which was heated on a hot plate above room temperature. PbSe QDs were deposited on the flat surface of highly oriented pyrolytic graphite (HOPG) substrates after a solvent evaporation. Raising the substrate temperature resulted in agitation of the QDs and varied the distribution of growth pattern coverage on a macroscopic scale. The resultant samples were subsequently studied using a field-emission scanning electron microscope (SEM, JEOL JSM-7000F). All SEM images were taken in a high vacuum at room temperature. The coverage of growth patterns was estimated based on the

SEM images, and usually an area of $5 \times 5 \mu\text{m}^2$ was selected for our studies. The coverage was calculated by using $\rho^* = \rho\sigma^2$, as described in the section 2.1. The windows of SEM imaging areas were varied on a millimeter scale, to broadly sample the coverage in QD growth patterns.

2.4 Results and discussion

The as-synthesized PbSe QDs are capped with TOP and oleic acid to prevent aggregation. As shown in Fig. 2.3(a), the TEM image demonstrates a cluster of PbSe QDs. These QDs exhibit either cubic or spherical shapes. A high resolution TEM image of an individual PbSe QD is given in Fig. 2.3(b). The image confirms a single crystalline structure with a lattice fringe spacing of 3.05 \AA which is in agreement with the lattice constant of the rock salt structure in PbSe bulk. The distribution of QD diameters determined in the TEM images is estimated and presented in Fig. 2.3(c). The size distribution can be fitted with Gaussian distribution, yielding a uniform and average diameter of $\sim 14.6 \text{ nm}$ and a standard deviation of 17%.

Several drops of the PbSe solution were cast on graphite substrates that were preheated above room temperature. After the solvent was evaporated, the QDs formed 2D islands (clusters) with either ordered (solid phase) or disordered (fluid phase) arrangements. After a coverage variation of QD assembly on different places of the substrate, the 2D islands can be imaged using an SEM. Moreover, the difference in coverage and temperature lead to a change of island size and distribution on the growth patterns, and to an observation of various growth mechanisms. The reduced coverage was estimated from the ratio of the island area to the SEM image area and then multiplied by 0.9165 [14].

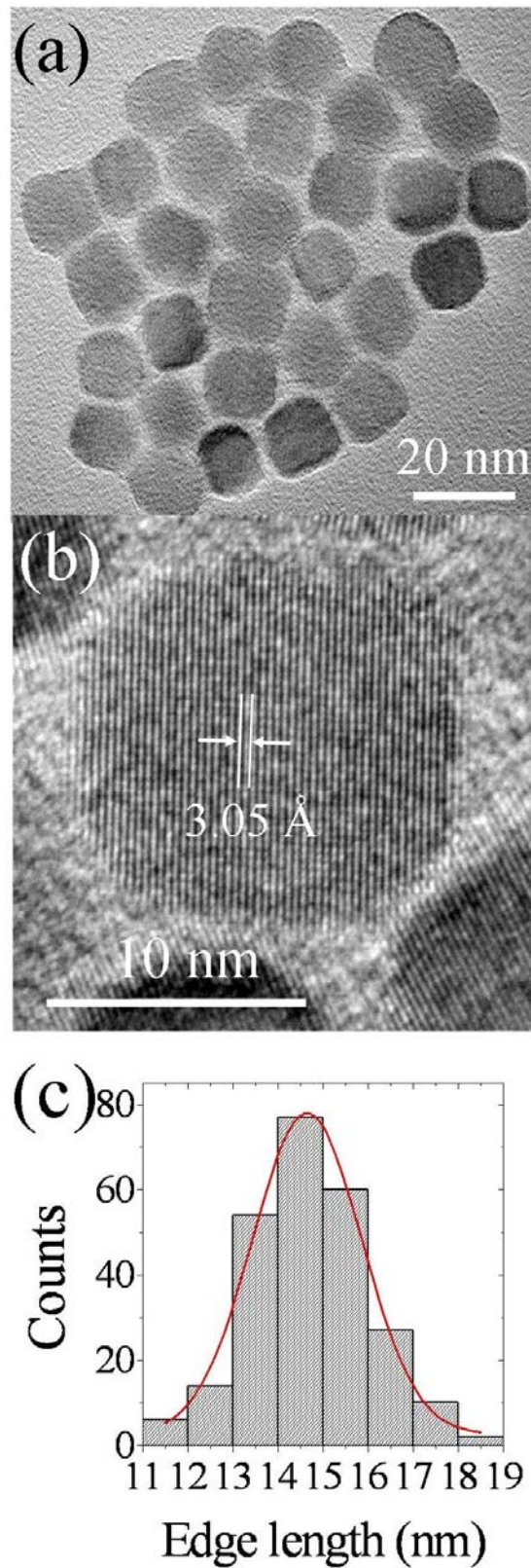


Figure 2.3: (a) TEM image of PbSe QDs. (b) High-resolution TEM image of an individual PbSe QD. (c) Statistical distribution of QD sizes and a red curve fitted with Gaussian function.

2.4.1 Growth pattern and phase diagram

Various different growth patterns of QD islands on graphite surfaces are displayed in Fig. 2.4. To understand and separate these growth patterns from each other, the following guidelines may be taken into account. The island number, island shape, island size distribution, and voids or holes on islands are important features to categorize the growth patterns. There are several growth mechanisms including diffusion-mediated nucleation [67-72] and diffusion-limited aggregation [73] on the (ρ^*, T^*) plane. In the nucleation process of the growth, a large fluctuation in island size and a rounded, streamline island shape are important features. On the contrary, the diffusion-limited aggregation results in a growth pattern showing a comparatively uniform size and a dendritic, straight line in shape. In addition, gas, liquid, and solid phases and the spinodal phase decomposition process shall engage to modulate the final morphology of the growth pattern. The gas phase shall show a large number of tiny islands or a complementary pattern containing a large number of voids (smaller holes), whereas the solid phase will exhibit a large area of single islands with few holes and voids. The solid phase should further demonstrate an ordered lattice points on fast-Fourier-transformed images, in comparison with a ring structure existed in the liquid phase. Finally, the spinodal decomposition shall reveal a long-range order and a sinusoidal composition (QD area density) modulation.

Fig. 2.4(a) shows an interconnected network, labyrinthine island pattern extending up to $40 \times 25 \mu\text{m}^2$. The growth pattern with $\sim 39\%$ coverage was prepared at 100°C . This pattern indicates undoubtedly a spinodal decomposition behavior scaling up to submillimeter that has never been observed in a room-temperature QD assembly yet. Other growth patterns achieved at the same temperature with varied coverage of 13%, 66%, and 90% are presented in Fig. 2.4(b)-(d). A complementary feature of

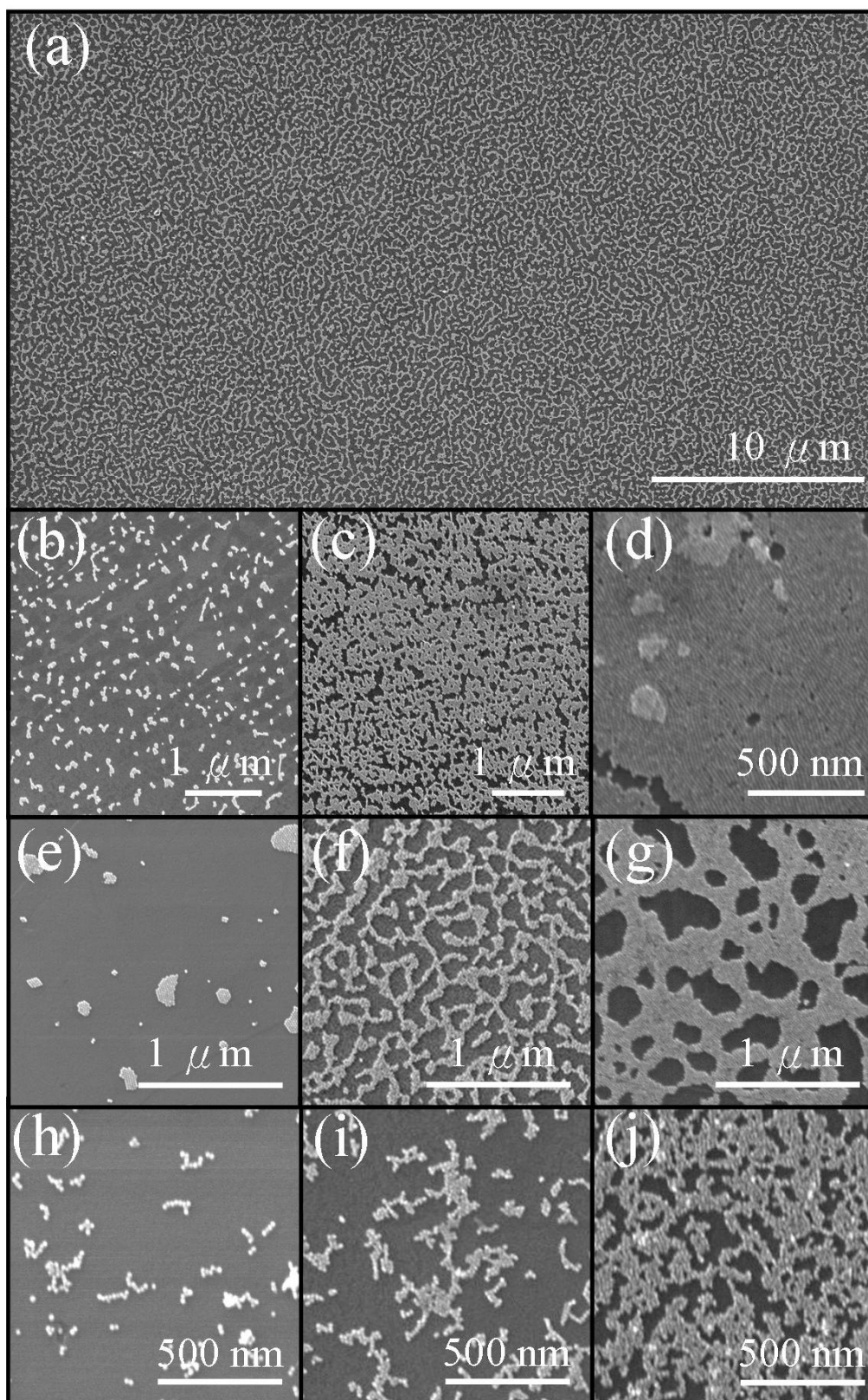


Figure 2.4: SEM images of PbSe QD patterns grown at substrate temperatures of 100°C (a-d), 50°C (e-g), and 180°C (h-j). The QD coverage is (a) 30%, (b) 13%, (c) 66%, (d) 90%, (e) 4%, (f) 41%, (g) 68%, (h) 6%, (i) 20%, and (j) 61%.

small islands and voids illustrated in Fig. 2.4(b) and (c) shows gas- and fluid-like phases, whereas a large island with few big holes, presented in part d of Fig. 2.4, reveals a solid phase at a growth temperature as high as 100°C.

When the substrate temperature was reduced to 50°C, a nucleation behavior was observed in the island pattern change. Fig. 2.4(e)-(g) illustrate a pattern variation with coverages of 4%, 41%, and 68%, respectively. An interconnected labyrinthine characteristic, signifying a spinodal decomposition behavior, can still be determined at such a low temperature (Fig. 2.4(f)). Moreover, a complementary manner of islands and holes in Fig. 2.4(e) and (g) demonstrate a nucleation process that unveils rounded islands or holes, and a large variation of island sizes implies a broadened island size distribution. Comparing Fig. 2.4(e) with Fig. 2.4(b), it can evidently be detected that a considerably large number of small islands with a uniform size appear in Fig. 2.4(b), whereas several area-unequal islands with a rounded shape show up in Fig. 2.4(e), although the coverage in both cases are of the same order. As a result, the gas phase and the nucleation growth behavior can definitely be differentiated from each other. Furthermore, as the *substrate temperature* was raised much higher than the boiling point of the solvent, the diffusion length of the QDs becomes shorter which in turn makes a transition from diffusion-mediated to diffusion-limited growth or aggregation. The shorter diffusion length mainly comes from a shorter time of solvent evaporation. As shown in Fig. 2.4(h)-(j), the growth patterns were formed at a substrate temperature of 180°C with different coverage areas of 6%, 20%, and 61%. The substrate temperature indicates that the growth temperature shall be no lower than the boiling point of toluene, whereas the elevated substrate temperature must cause rapid evaporation of the solvent, resulting in a diffusion-limited growth behavior. Unlike the gas phase and the nucleation growth patterns, Fig. 2.4(h) demonstrates a few of straight, chainlike islands, showing that an increase of the coverage results in a

formation of chain-like islands or dendritic islands. Further increase of the coverage (refer to Fig. 2.4(j)) shows a dendritic islands as dominant structure and a shape of straight line on the edge of islands. To compare with those prepared at 100 and 50°C (Fig. 2.4(d) and (g)), the growth pattern in Fig. 2.4(j) reveals a thin strip rather than rounded holes.

Unlike the growth at room temperature that a drying process could induce an increase of pair bond energy ϵ (a decrease of reduced temperature) and change the state from a high to a low reduced temperature [13, 14], the high temperature growth causes a rapid evaporation of the solvent so that the resultant patterns could be quenched. To put all growth patterns (Fig. 2.4) on the (ρ^*, T^*) plane, we need to determine the pair bond energy. Here, the island number variation as a function of coverage at various temperatures (Fig. 2.5(a)) for the same image size of $5 \times 5 \mu\text{m}^2$ is used to determine the pair bond energy, which can be verified further in another analysis in the following paragraphs. We found that the growth pattern at 50°C reveals the lowest island density and a decrease of island density from ~ 100 to $\sim 10 \mu\text{m}^{-2}$ as the coverage is raised from 10% to 40%. This low island density is mainly due to the nucleation growth and the spinodal decomposition behaviors. As shown in Fig. 2.4(e)-(g), islands can be counted individually only when a coverage is much lower than $\sim 50\%$. With higher coverage, the spinodal decomposition process drives the islands to coalesce into one or few large islands. With much higher coverage, the nucleation mechanism turns on again and we can observe many large holes in a single, large island in Fig. 2.4(g). Conversely, when the coverage is about 10-20% and the temperature is increased up to 100°C (Fig. 2.4), the island density is doubled or tripled in number, probably owing to a transition from the state in nucleation region to a gas (fluid) state on the phase diagram. The island density increases further but not so much when the substrate temperature is of 130 or 180°C. Again, the growth

temperature is around the boiling point of toluene and the elevated substrate temperature only causes toluene to evaporate quickly and induces diffusion-limited aggregation. It was observed that the island density decreases exponentially with coverage at almost all temperatures, whereas it shows a steepest descent with a coverage of $\sim 35\%$ for the growth at 100°C . This great deal of island density variation is attributed to a phase transition from the gas phase, featured a large island density, to the states in spinodal decomposition regime, revealing few coalesced islands and low island density. It is noted that the data at 50°C probably reveal a state variation on the phase diagram from the nucleation to the spinodal decomposition regime. States on both of those two regions share the same feature of a small amount of islands. Moreover, the data at 130 and 180°C imply a phase transition from the gas to the liquid phases, sharing the same feature of a larger amount of islands. Through this island density analysis, we conjecture that the temperature of 100°C shall be very close to the critical-point temperature of this 2D QD system. We therefore propose a reduced temperature T^* of 0.5418 (slightly lower than the critical-point temperature, $T^* = 0.55$) to be at 100°C then the pair bond energy ε of $690k \cong 59$ meV can be estimated.

After the pair bond energy is determined, those states of growth patterns (Fig. 2.4) can be assigned and marked on the 2D Lennard-Jones phase diagram of Fig. 2.5(b). On this phase diagram, the top point of solid curve near the symbol **a** is close to the gas-liquid critical-point temperature ($T^* = 0.55$) [67] and the dashed line indicates the triple-point temperature ($T^* = 0.41$) [67]. The area between solid and dashed curves belongs to a nucleation growth process and the area under the dashed curve and the dashed line belongs to a spinodal decomposition region. The identification of states on the phase diagram gives reasonable explanation of growth patterns shown in Fig. 2.4(a)-(g). As pointed out, only the substrate temperature of the

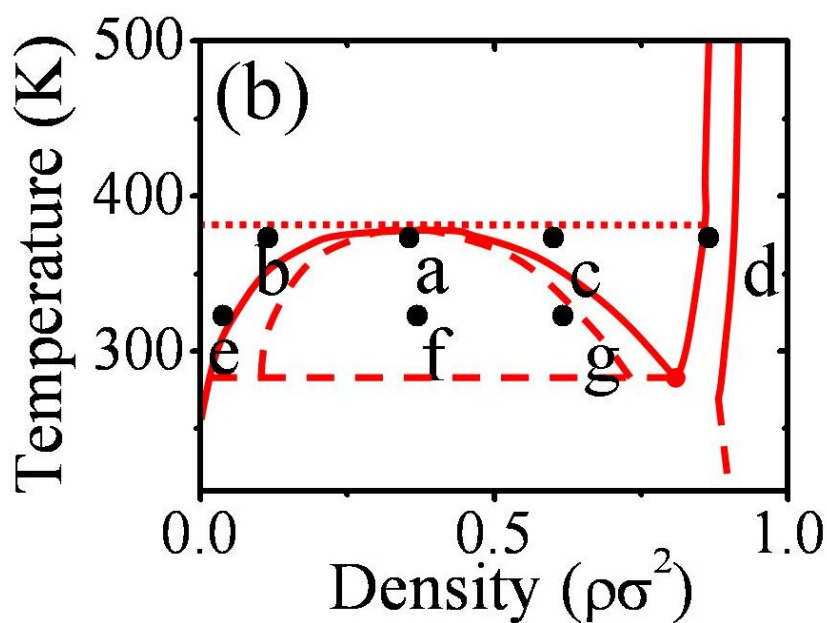
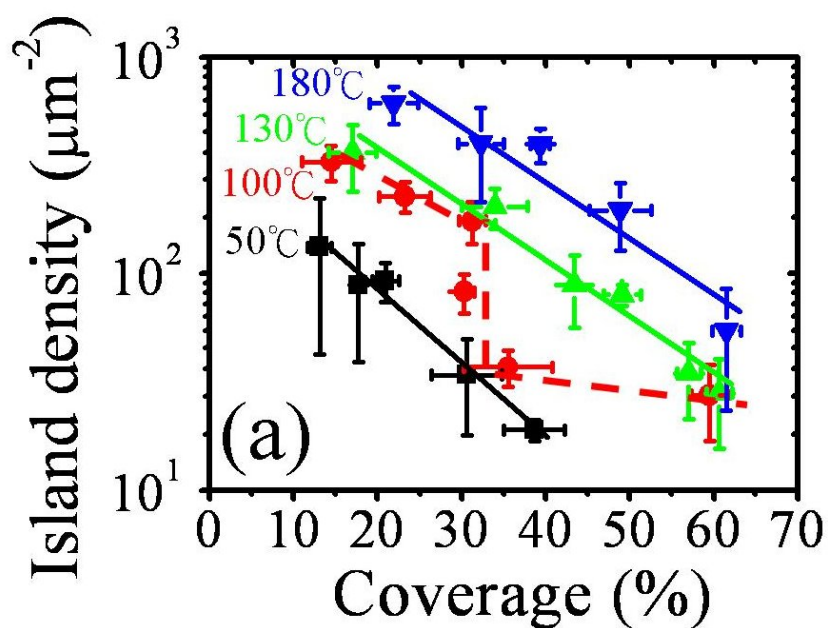


Figure 2.5: (a) Island density as a function of QD coverage grown at various different temperatures indicated on graph. (b) Phase diagram of a 2D Lennard-Jones system, reproduced from refs 14 and 67. The symbols, a-g, point to the growth conditions of the patterns shown in Figure 2.2. The dotted line indicates the boiling point (110.6°C) of the toluene solvent.

growth patterns shown in Fig. 2.4(h)-(j) is specified, so their states are not presented in Fig. 2.5(b). A dotted line indicates the boiling point of toluene solvent to emphasize that the diffusion-limited aggregation shall be enhanced at a substrate temperature above this line.

2.4.2 Growth mechanisms

Several growth mechanisms play important roles to modulate the growth pattern. In the initial growth stage, the cluster occurrence correlates with a decrease of free energy in cluster formation. Moreover, the scaling function can be used to evaluate the critical nucleus size. As the coverage increases, a growth mechanism of the spinodal decomposition is involved. Moreover, as for our case of the QD growth in solution, a higher substrate temperature and the rapid evaporation of solvent shall induce a diffusion-limited aggregation.

Fig. 2.6(a)-(c) show the occurrence N of small clusters as a function of the cluster aggregation number n , calculated on the basis of fifty SEM images with an area of $2.8 \times 2.1 \mu\text{m}^2$. The occurrence of single QD, 2-QD, 3-QD, and n -QD clusters are denoted as N_1 , N_2 , N_3 , and N_n , respectively. The data present with n in a range from 3 to 9. Because the formation of n -QD cluster from isolated QDs makes a decrease of energy ($-E_n$) and affects the occurrence (possible configurations) through a thermal equilibrium process, the occurrence shall follow the form [69]

$$N_n = N_0 (N_1 / N_0)^n \exp(E_n / kT) \quad (2.5)$$

where N_0 is the total number of QDs to cover the whole area of the SEM image. Using the same assumption in ref 14, each bond causes a decrease of free energy (akT) and

the formation of n -QD cluster for $n > 1$ leads to a lowering of free energy ($E_n = (2n - 3)\alpha kT$). This gives

$$N_n = N_0 (N_1 / N_0)^n \exp((2n - 3)\alpha) \quad (2.6)$$

Usually the occurrence of a single QD is not easy to be counted possibly due to the limit of the image resolution. The other reason could be attributed to the fact that the stable nucleus size is larger than one, and therefore a single QD has a high tendency to coalesce on big islands. A nonlinear least-squares fitting was used to evaluate N_1 and α . The fitting results are displayed as solid curves in Fig. 2.6(a)-(c). It is noted that Eq. 2 is valid only for $n \geq 2$. A straight line is therefore given to simply connect the two calculated values of N_1 and N_2 . The parameter α was determined to be 1.13, 0.99, and 0.85 for growth data at 50, 100, and 180°C, respectively. Thus the pair bond energies (αkT) were estimated to be 31, 32, and 33 meV for clusters grown at 50, 100, and 180°C. This gives an average value of about 32 meV, which is about one-half of the pair bond energy $\varepsilon = 59$ meV estimated from Fig. 2.5(a). In particular, the pair bond energy is very close to the calculated attraction energy of 40 meV ($1.6 kT$) and experimentally evaluated value of 88 meV ($3.5 kT$), as reported in ref 14.

On the other hand, the critical nucleus size can be determined by a scaled island size distribution. The island size distribution, which is normally N_n as a function of the QD number n , is scaled to $N_n n_{\text{avg}}^2 / \theta$ as a function of n/n_{avg} , where θ is the coverage and n_{avg} is the average size of the QD-formed islands. The scaled island size distributions with specified coverage of 5-15% and at different temperatures are displayed in Fig. 2.6(d)-(f). Because it is analyzed at low coverage, we can ignore the spinodal decomposition behavior. Thus only the temperature and solvent drying effects will be taken into account. In Fig. 2.6(e), a solid line of scaling function is displayed to indicate a critical nucleus of one QD, which means that island size with

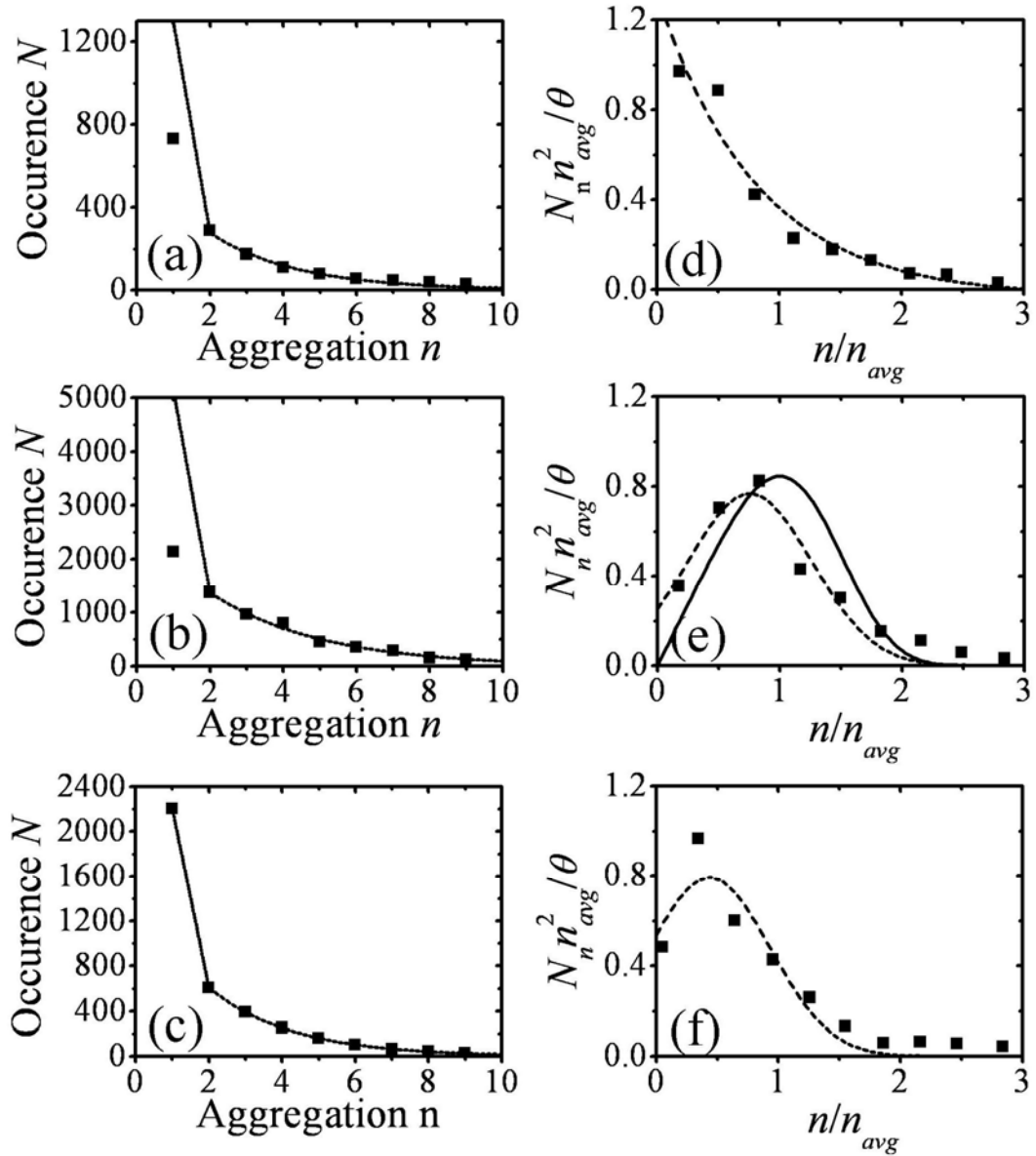


Figure 2.6: Occurrence as a function of aggregation number (n , number of QDs) corresponding to small islands with 3-9 QDs at (a) 50, (b) 100, and (c) 180°C. The solid lines present the fitting results. Scaled island size distributions at (d) 70, (e) 100, and (f) 130°C. The coverage are (d) 4, (e) 13, and (f) 16%. The dashed lines are guides to eyes. The solid line in Figure (e) represents the scaling function corresponding to a critical nucleus size $n = 1$ and a stable cluster size $n \geq 2$.

two more QDs are stable. Fig. 2.6(d) shows that, at 70°C, even a single QD can be stable and exist on the graphite surface. At a higher temperature of 100°C (Fig. 2.6(e)), the excess thermal energy makes single QD more mobile and islands having at least two QDs can stably exist in growth patterns. The critical nucleus size therefore increases and the smallest stable island must consist of at least two QDs. This result is in line with the temperature effect on critical nucleus reported for atomic growth behavior [76]. The critical nucleus size slightly changes back to one QD at an elevated temperature, 130°C (Fig. 2.6(f)). We believe that, at this high temperature, the solvent drying process should be taken into account. More interestingly, part e of Fig. 2.6 indicates a stable cluster of $n \geq 2$. This result can also be confirmed in the bonding energy analysis displayed in Fig. 2.6(b). We found that the experimental value is much lower than the calculated value of occurrence of single adsorbed QD for growth at 100°C. On the contrary, the measured occurrence of single QD is more close to the calculated value in Fig. 2.6(a) and (c). It is noticed that the growth behavior varies with a different substrate temperature above the solvent boiling point (Fig. 2.6(c) and (f)).

With an increase of coverage, owing to a coexistence of two phases, the growth mechanism of spinodal decomposition engages to modulate sinusoidally the compositional (QD density) variation that generates a macroscopically uniform island size distribution with an interconnection labyrinthine structure. Two spinodal growth patterns assembled at 100 and 50°C are exhibited in Fig. 2.7(a) and (b), respectively. Evidently, different wavelengths of the sinusoidal compositional modulation can be identified between the two SEM images. This wavelength variation has not been experimentally discovered in room-temperature QD assembly yet [13, 14, 62]. According to the spinodal phase separation theory [72], the wavelength is inversely proportional to the square root of the undercooling temperature, $\lambda \propto (T_C - T)^{-1/2}$, where

T_C is the critical-point temperature. To evaluate the wavelength of the sinusoidal composition modulation, the radial average intensity of fast-Fourier-transformed image was calculated (inserts of Fig. 2.7 as examples). The wavelengths at maximum intensity are 450 and 176 nm for growth patterns shown in Fig. 2.7(a) and (b), respectively. The temperature behavior of the wavelength at maximum intensity is thus summarized in Fig. 2.7(c). When the temperature is increased above room temperature, it was found that the wavelength increases up to a maximum value at 100°C. More excitingly, the spinodal growth patterns remain observable even if the substrate temperature is much higher than the critical-point temperature. This result is in contradiction to the gas or fluid phase above critical-point temperature that is predicted in the phase diagram (Fig. 2.5(b)). In addition, the wavelength at maximum intensity shown in Fig. 2.7(c) reveals a decline with an increase of the substrate temperature above the toluene boiling point. We therefore conclude that the elevated substrate temperature makes the solvent to evaporate and the growth mechanism of diffusion-limited aggregation is in turn employed to modify the growth pattern. Because of the rapid evaporation of toluene solvent, the decrease of wavelength at elevated temperature shall be resulted from a reduced evolution time [77] required for long-wavelength spinodal patterns such as that displayed in Fig. 2.7(a). The interplay between spinodal decomposition and diffusion-limited aggregation could be studied and further controlled by using substrate temperature and QD coverage (concentration of QD suspension) so as to grow 2D islands with specified sizes and shapes.

Because the solvent evaporation introduces a diffusion-limited growth mechanism, the analysis method used in atomic growth of diffusion-limited aggregation can certainly be implemented here. Either the density-density correlation function or the radius of gyration as a function of cluster size (aggregation number n) [73] can be applied to the investigation into the randomly aggregated fractal structure.

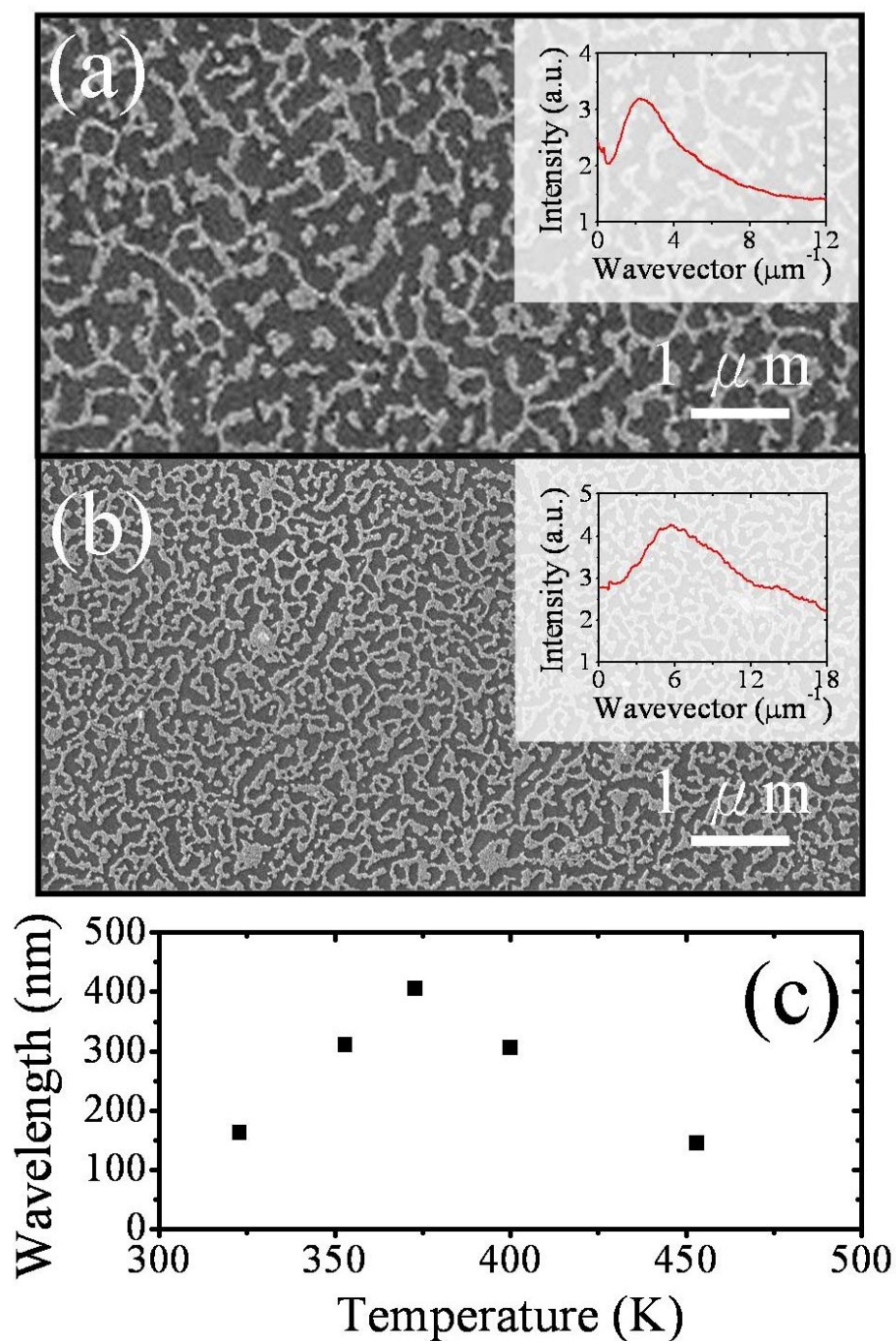


Figure 2.7: (a) SEM image of a spinodal pattern grown with coverage of $\sim 38\%$ at 100°C . (b) SEM image of a spinodal pattern grown with coverage of 45% at 50°C . The insets show fast-Fourier-transformed and radial averaged intensity as a function of inverse wavelength. (c) Wavelength at maximum intensity, estimated from the intensity distribution, like the inserts of parts (a) and (b), for QD growth with coverage of $\sim 42\%$ and at different temperatures.

The analysis using radius of gyration, R_g , which is a mean square distance between the particle and the center of mass of the cluster, is adopted in this study. A fractal dimension D is introduced in the expression $n \sim R_g^D$ [73]. Log-log plots of R_g as a function of aggregation number n are given in Fig. 2.8(a) and (b) for patterns (the inserts) grown at 100 and 180°C respectively, with coverage of ~20%. The fractal dimensions D 's are estimated to be 1.38 and 1.57 as indicated in the figure. This observable difference in D shall be originated from the substrate temperature. At the temperature of 100°C and below the toluene boiling point, the toluene solvent shall not be evaporated so quickly and the as-aggregated clusters may diffuse on surface and coalesce into larger ones. This experimental result of fractal dimension $D = 1.38$ is considerably close to the cluster diffusion models given by P. Meakin [78] ($D = 1.47$) and M. Kolb et al. [79] ($D = 1.38$). On the other hand, a high substrate temperature of 180°C leads to a random aggregate of cluster which by no means can diffuse on substrate anymore due to the solvent dry-up. This result of fractal dimension $D = 1.57$ is in line with the predicted value of 1.67 using the WS model [73]. The cluster diffusion at 100°C seems to be in connection with a long evolution time required to produce a long wavelength of spinodal growth patterns as discussed above. Here, the interplay between the spinodal decomposition and the diffusion-limited aggregation appears again. Two schemes to illustrate the cluster diffusion and single-particle diffusion models are given in Fig. 2.8(c) and (d). For the same aggregation number n , the cluster diffusion causes a longer radius of gyration and thus a smaller fractal dimension.

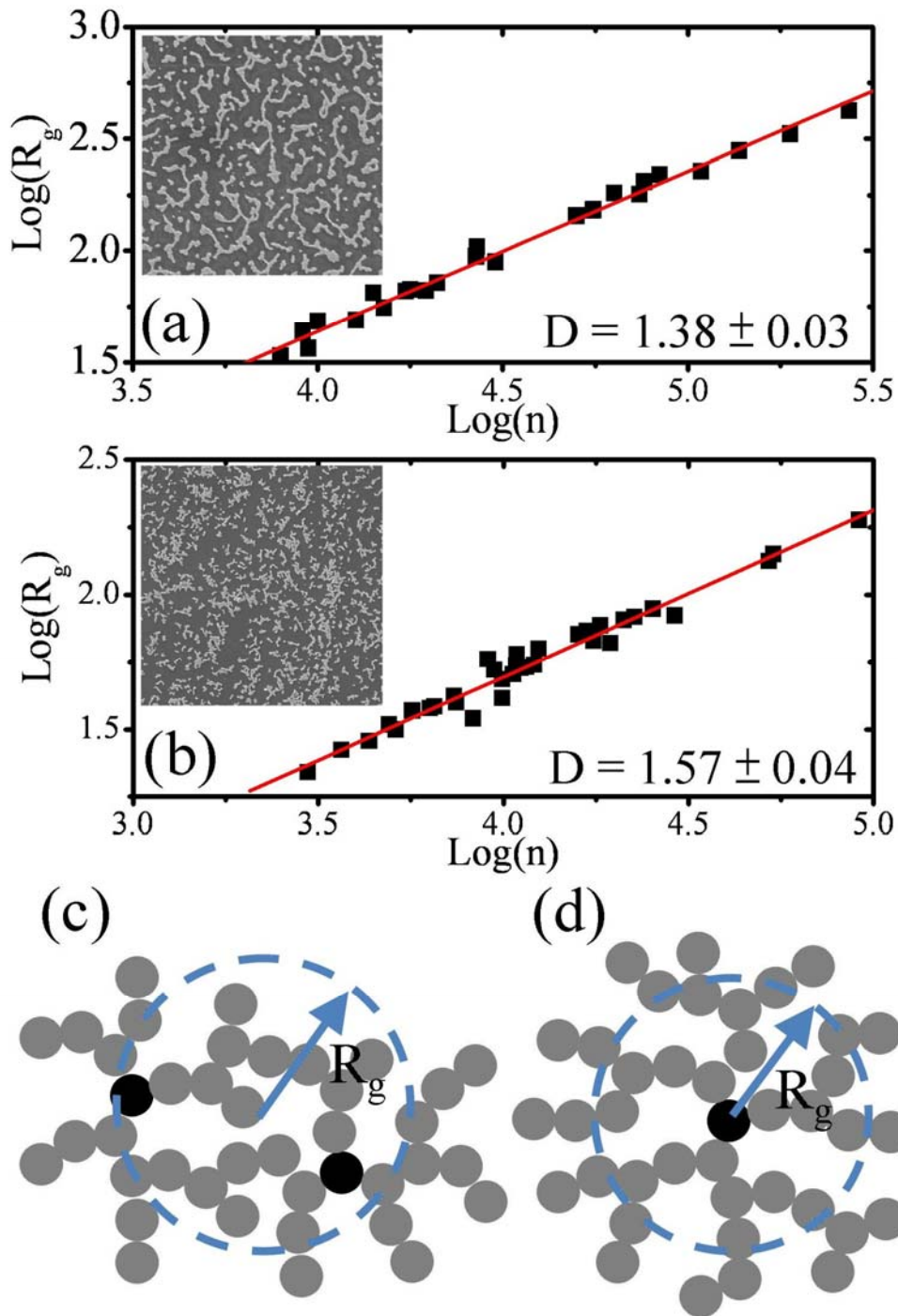


Figure 2.8: Gyration radius, R_g , has a power law dependence on the aggregation number, n , in double logarithm scales for QD growth at (a) 100°C and (b) 180°C with coverage of 21% and 18%, respectively. Corresponding SEM images are displayed in the insets. Schemes of (c) cluster diffusion and (d) single-particle diffusion models.

Chapter 3

Collective transport in PbSe quantum dot arrays

3.1 Introduction

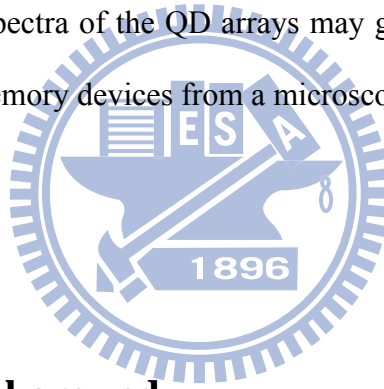
Few electrons stored on small metal particles or semiconductor quantum dots (QDs) will build a charging energy to block additional electrons' tunneling. This effect is called Coulomb blockage. It changes the conductivity of the current channel due to the small capacitance of the tiny-sized particles which give large blocking Coulomb energy [81, 82]. The few-electron charging effects have been applied not only to single-electron transistors but also to the fabrication of single-electron [83, 84] and nanocrystal based memories [6, 85] for operating at room temperatures. Moreover, another similar phenomenon of electrical bistability exhibits two conductivity states at the same voltage. This nonvolatile electrical bistability has been discovered and demonstrated in the system of nanoclusters embedded in organic or oxide layers [86, 87]. Recently, many organic bistable devices, containing different materials of metal particles or semiconductor QDs dispersed in organic layers, have displayed a large hysteresis in current- or capacitance-voltage curves that reveal bistable effects in conductivity and capacitance [86-89]. Although band diagram models have been

proposed to explore the device operation mechanism, investigation of the electrical coupling effect among particles from a microscopic viewpoint has not been intended yet.

In recent years, a high temperature organic solution-based wet-chemical strategy has been successfully developed in synthesizing high crystalline QDs in which the surface of particles is passivated by organic ligands [57]. These chemically generated QDs were introduced in a nanogap between metal electrodes for approaches to electrical studies of a single dot [90] and to a single-electron transistor [91]. Meanwhile, the QDs could self-assembled into quasi-one-dimensional chains and two- or three-dimensional arrays. The current-voltage (I - V) behavior at various temperatures has been measured for self-assembled chains of conducting carbon nanoparticles [30] and quasi-one-dimensional arrays of gold nanocrystals [31]. In addition, the transport of electrons has been studied in the two-dimensional systems of cobalt-nanocrystal superlattices [2], Au nanocrystal arrays [92], CdSe QD arrays [93], and the topographically complex Au nanoparticle network [35]. These studies reveal a nonlinear I - V curve and a temperature-dependent threshold voltage V_{th} at lower temperatures. In particular, the I - V curves at different temperatures can be collapsed to a single power-law $I(V-V_{th})$ curve by translation on the voltage scale above V_{th} . This behavior is recently exposed in a system of Au nanoparticles self-assembling in organic thin films as well [94]. On the other hand, the scaling behavior has been observed in the early research of lithographically patterned GaAs QDs and Al island arrays [27, 28]. A collective transport model considered by Middleton and Wingreen (MW) can be used to explain the aforementioned experimental results [29].

In the very early studies, scanning tunneling microscope (STM) has been used to observe the Coulomb blockade characteristics of staircase features on I - V curves of an individual metal droplet or cluster at a very low temperature [95] as well as at room

temperatures [96]. Recently, not only the Coulomb effect but also the electronic structures of artificial-atom states in the colloidal and semiconducting QDs were investigated by several research groups [17, 20] through measurements of tunneling spectroscopy with the aid of low-temperature STM. In addition to the single-QD electronic states, the interparticle Coulomb interactions [23] and the level structure of InAs QDs in two-dimensional assemblies [24] draw attention for tunneling spectroscopy characterizations. However, the array size effects, which might exhibit during the assembling process from a single QD to a two-dimensional QD array, and the capacitive coupling among the QDs have not been explored to date. In this study, we employ STM to probe the size effects in the coupled PbSe QD arrays. The size-dependent tunneling spectra of the QD arrays may give a clue to understand the operation mechanism of memory devices from a microscopic viewpoint.



3.2 Theoretical background

Based on the Coulomb blockade, a analytic form of tunneling current can be derived by a double tunnel junction model. As the junctions form an array, there will be a collective behavior of charge transport. We briefly introduce the double tunnel junction and collective transport model which are adopted to analyze our results.

3.2.1 Coulomb blockade and double tunnel junction model

The phenomenon ‘‘Coulomb blockade’’ was first observed in an assembly of double tunnel junction, which was made of small stannum particles embedded in an aluminum layer, by Giaever and Zeller [102]. In such a double tunnel junction system, the charged small island results in a large capacitance as well as electrostatic energy to block another electron from transporting into the island. Experimentally, there is a threshold voltage below which the current is suppressed. Under an appropriate bias, electron can tunnel through the junctions one by one. To observe Coulomb blockade, two conditions have to be met. Firstly, the charging energy of the small island $E_c = e^2/2C$ must exceed the thermal fluctuation $k_B T$, where C is the capacitance of the small island. Secondly, the tunneling junction must have a resistance R_T larger than the quantum resistance $\hbar/e^2 \cong 25.8 \text{ k}\Omega$ to satisfy the requirement of Heisenberg uncertainty principle $\Delta E \Delta t \geq \hbar/2\pi$ ($RC = \Delta t$).

On the basis of Coulomb blockade, there is an orthodox theory of double tunnel junction that provides an analytic form for the scanning tunneling spectroscopy [98, 99]. Fig. 3.1 illustrates an STM geometry which is modeled as a double tunnel junction system. Consider a small island placed between an STM tip and a substrate, which is biased with a voltage V , the junction (junction 1) between the tip and the island possesses a capacitance C_1 and a resistance R_1 . By analogy, C_2 and R_2 are the capacitance and resistance of the junction (junction 2) between the island and the substrate. With N extra electrons on the island, the voltage drops on junction 1 and 2 are

$$V_1 = \frac{C_2}{C_1 + C_2} V - \frac{Ne - Q_0}{C_1 + C_2} \quad (3.1a)$$

$$V_2 = \frac{C_1}{C_1 + C_2} V + \frac{Ne - Q_0}{C_1 + C_2} \quad (3.1b)$$

, where Q_0 is the residual charge. Physically, the Q_0 ranges only between $-e/2$ to $+e/2$ and the excess part will be incorporated in N . For a steady-state condition that the

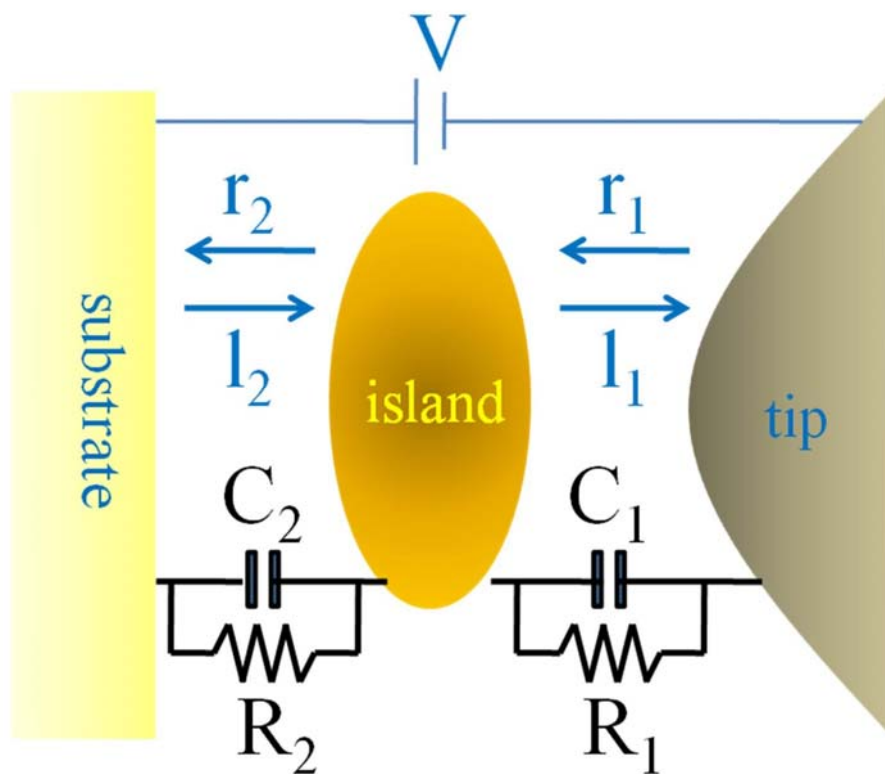


Figure 3.1: Schematic diagram of an STM geometry which is modeled as a double tunnel junction system. The two junctions of capacitances C_1 and C_2 , and resistances R_1 and R_2 , are driven by a voltage source V .

transition rate from the state N to $N+1$ is equal to the reverse rate, we have

$$(r_1(N, V) + l_2(N, V))p(N, V) = (l_1(N + 1, V) + r_2(N + 1, V))p(N + 1, V). \quad (3.2)$$

$r_i(N, V)$ and $l_i(N, V)$ are the electron tunneling rate from right and left on the junction i , and $p(N, V)$ is the probability that there are N electrons on the island with a bias V .

With the normalization condition

$$\sum_{N=-\infty}^{+\infty} p(N, V) = 1, \quad (3.3)$$

Eq. (3.2) can be solved to obtain that

$$p(N, V) = \frac{\left[\prod_{i=-\infty}^{N-1} (r_1(i, V) + l_2(i, V)) \right] \left[\prod_{i=N+1}^{+\infty} (l_1(i, V) + r_2(i, V)) \right]}{\sum_{j=-\infty}^{+\infty} \left[\prod_{i=-\infty}^{j-1} (r_1(i, V) + l_2(i, V)) \right] \left[\prod_{i=j+1}^{+\infty} (l_1(i, V) + r_2(i, V)) \right]}. \quad (3.4)$$

The average current is then

$$I = e \sum_{N=-\infty}^{+\infty} [r_1(N, V) - l_1(N, V)] p(N, V). \quad (3.5)$$

To calculate quantitative tunneling current I , we have to know the expression of the four tunneling rates, *i.e.* r_1 , l_1 , r_2 , and l_2 . From Fermi's golden rule, the tunneling rate can be derived as

$$\Gamma = \int_{-\infty}^{\infty} \frac{2\pi}{\hbar} |T(E)|^2 D'(E - E') f(E - E') D''(E - E'') [1 - f(E - E'')] dE. \quad (3.6)$$

Here E' and E'' are the Fermi energies of different sides, with extra electrons, of the junction. $f(E)$ is the Fermi-Dirac distribution $f(E) = 1/(1 + e^{E/k_B T})$. Taking the transmission coefficient $|T(E)|^2$, the density of states $D'(E)$, and $D''(E)$ as constants,

Eq. (3.6) is simplified to

$$\begin{aligned} \Gamma &= \frac{1}{e^2 R} \int_{-\infty}^{\infty} f(E - E') [1 - f(E - E'')] dE \\ &= \frac{1}{e^2 R} \frac{\Delta E}{(1 - e^{-\Delta E / k_B T})}. \end{aligned} \quad (3.7)$$

, where $R \equiv \hbar/2\pi e^2 D'_0 D''_0 |T_0|^2$ and $\Delta E = E' - E''$. The ΔE means the energy that electrons gain after tunneling through the junction and can be considered as the sum of the change in electrostatic energy and the work done by the applied voltage. For tunneling rate

$$\Delta E = \begin{cases} r_1(N, V) & \left[eV_1(N) - \frac{e^2}{2(C_1 + C_2)} = \frac{e^2}{C_1 + C_2} \left[-N - \frac{1}{2} + \frac{VC_2}{e} + \frac{Q_0}{e} \right] \right. \\ l_1(N, V) & \left. -eV_1(N) - \frac{e^2}{2(C_1 + C_2)} = \frac{e^2}{C_1 + C_2} \left[N - \frac{1}{2} - \frac{VC_2}{e} - \frac{Q_0}{e} \right] \right. \\ r_2(N, V) & \left[eV_2(N) - \frac{e^2}{2(C_1 + C_2)} = \frac{e^2}{C_1 + C_2} \left[N - \frac{1}{2} + \frac{VC_1}{e} - \frac{Q_0}{e} \right] \right. \\ l_2(N, V) & \left. -eV_2(N) - \frac{e^2}{2(C_1 + C_2)} = \frac{e^2}{C_1 + C_2} \left[-N - \frac{1}{2} - \frac{VC_1}{e} + \frac{Q_0}{e} \right] \right. \end{cases} \quad (3.8)$$

(Eq. (3.1a) and (3.1b) are used.) From Eq. (3.8), the voltage drops on each junction has to be the value larger than $e/2(C_1 + C_2)$ to have a non-zero ΔE for tunneling. Thus the V should exceed $(e/2 - Q_0)/C_>$, where $C_>$ is the greater of C_1 or C_2 , to have a current flow. The voltage with this value is called threshold voltage V_{th} , below which the current is suppressed.

3.2.2 Collective transport: MW model

Charge transport in an array which consists of small metallic dot exhibits a nonlinear behavior with a threshold. Middleton and Wingreen (MW) proposed a model to explain this collective charge transport behavior in one- and two-dimensional dot arrays [29]. Their model is based on the Coulomb blockade regime which means the electron transports among the dots in arrays by tunneling and the thermal fluctuation cannot exceed the charging energy. They predicted the current through a uniform

array behaves as

$$I \sim \left(\frac{V}{V_T} - 1\right)^\zeta \quad (3.9)$$

with $\zeta = 1$ and $5/3$ for one- and two-dimension arrays, respectively.

Fig. 3.2(a) presents a schematic illustrating the build of charges in a one-dimensional array between two electrodes as the voltage is progressively increased to threshold. Each square represents a potential e/C_g for adding an electron on a dot, where C_g is the capacitance between dot and substrate. With randomly distributed offset charge on a one-dimensional array, electron can spontaneously tunnel to the next dot or be blocked in a down-ward or up-ward step, respectively. The threshold voltage V_T means the potential difference $V_L - V_R$ is enough to drive electron transport from left to right electrode. As the array size N (number of dot) is very large, statistically, an electron has to overcome $N/2$ up-ward step, and thus we have

$$V_T = \frac{N e}{2 C_g} \quad (3.10)$$

From Eq. (3.7), the tunneling rate at very low temperature is approximately $\Delta E/e^2 R$. For the conduction state, $V > V_T$, since there are N dots in the array, the average energy difference ΔE is then $e(V - V_T)/N$ resulting a tunneling rate $(V - V_T)/eRN$. With Eq. (3.10), the current $I = e\Gamma$ is then given by $\frac{e}{2RC_g} \frac{V - V_T}{V_T}$ and therefore the $\zeta = 1$ in Eq. (3.9) for one-dimensional array.

For a two-dimensional array with the size $N \times N$, the extra charges driven by applied voltage penetrate the array and form an interface, at which the charges are blocked until the driving voltage is increased. Because of the disordered offset charge the interface is irregularly shaped and the voltage that makes the interface reach the other electrode is the threshold voltage V_T . At $V > V_T$, current-carrying channels are formed. Similar to one-dimensional array, there will be $(V - V_T)/(e/C_g)$ excess steps

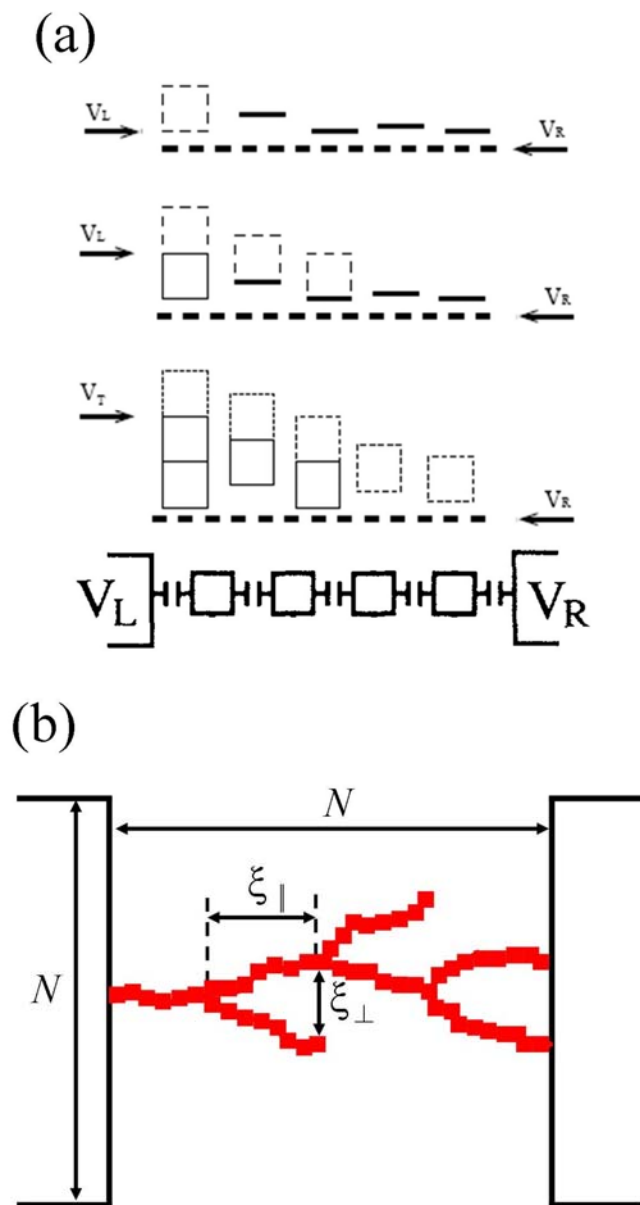


Figure 3.2: (a) A schematic illustrating the build of charges in a one-dimensional array as the voltage is progressively increased to threshold. (b) A scheme of branched channel in a $N \times N$ two-dimensional array.

(charges), on average, in a channel. Since the electrons can transport not only forward but also probably to lateral dots in the two-dimensional array, those excess steps can make a split in the channel. The average distance between each branch points is then $\xi_{\parallel} = eN/(V - V_T)C_g$. The Kardar-Parisi-Zhang (KPZ) equation [103], which describes the growth of interfaces, is adopted to give that the transverse deviation ξ_{\perp} will be $\xi_{\parallel}^{2/3}$ in a length ξ_{\parallel} . Fig. 3.2(b) shows a scheme of branched channel in an array. Thus the number of channel reaching right electrode will be $N/\xi_{\parallel}^{2/3} \sim N(\frac{V - V_T}{V_T})^{2/3}$. For a single channel, the current is $\frac{e}{2RC_g} \frac{V - V_T}{V_T}$, thus the total current in the array is given as $\frac{Ne}{2RC_g} (\frac{V - V_T}{V_T})^{5/3}$. From above, we know that the number of current channel is increased with the voltage. Before all the possible channels are turned on, the current will behave as $I \sim (V - V_T)^{5/3}$. This region can be view as a transition from an isolated state to a conducted state, at which the current is linearly depended on the voltage.

3.3 Experiment

Several drops of the solution were put on a conducting and flat substrate. The chosen substrate was atomically flat terraces, with several hundred nanometers in size, on Au(111) surfaces on a ball prepared by melting a 2-mm gold wire in a gas flame. The as-deposited PbSe QDs formed islands with QD numbers from one to several tens and the assembling process can be controlled by the growth conditions of the substrate temperature and the solution concentration which we described in chapter 2. The morphology of QD islands on Au(111) surfaces was inspected by field-emission

scanning electron microscope (JEOL, JSM-7000F) and atomic force microscope (Seiko Instruments Inc., SPA-300HV). The sample of as-assembled QD islands was loaded in a STM preparation chamber in an ultrahigh vacuum of 1×10^{-10} torr, and it was heated up to 100-150°C for more than 10 h. When annealing at 150°C, long time of thermal treatment helped to detach more organic ligands and to squeeze the distance between QDs. In addition, the PbSe QD islands liquefied and evaporated as the annealing temperature was increased up to 300°C. The thermal annealing converts the as-assembled QD islands to compact and ordering QD arrays as well. The sample of QD arrays on Au(111) surfaces was transferred to a STM main chamber and the STM analysis were carried out by Omicron LT STM. An electrochemically etched tungsten tip was used in our experiment. All STM images were taken in a constant current mode with a sample bias of 2.5 V and a tunneling current (setpoint) of 0.15 nA. After the PbSe QD array was specified in a STM topography image, current image tunneling spectroscopy (CITS) will be taken at the same place. The tunneling spectra were taken with voltages ramped from -1.5 to +1.5 V under a scanning condition of the sample bias 1.5 V and the tunneling current 0.15 nA. There were 100×100 points in a CITS image and every CITS image point contained an I - V curve having 200 steps. The STM images and CITS data were recorded at both room temperatures and 78 K. Since the slightly deviated separation distance between the STM tip and the sample could produce a large current fluctuation, the statistically averaged I - V curve from several tens or hundreds of CITS image points was evaluated for an individual PbSe QD array. All the data were analyzed using the software of scanning probe image processor (Image Metrology A/S, SPIP). The I - V was analyzed and fitted by the Levenberg-Marquardt nonlinear least squares method [78].

3.4 Results and discussion

The characterization of the PbSe QD size distribution is described in chapter 2 giving a uniform and average diameter of ~ 14.6 nm and a standard deviation of 17%. To investigate the electronic structure of these QD arrays using an STM, PbSe QDs are deposited on a conducting substrate. The QDs will form clusters as well as islands on the substrate with different sizes and shapes owing to different packing conditions. Fig. 3.3(a) shows a typical STM image of PbSe QD arrays on a flat Au(111) surface. Before annealing in an ultrahigh vacuum, PbSe QDs form a monolayer of two-dimensional islands demonstrating either disordered clusters or locally regular arrangements. The as-deposited QD islands seem to be mobile and cause a blurred image under the scanning measurements of STM. After annealing and removal of excess capping agents, the QD islands are organized as two-dimensional arrays and fixed on a flat gold surface to stabilize the STM scans. Fig. 3.3(b) shows a two-dimensional PbSe QD array with 229 QDs on the Au(111) surface. The arrays appear as a hexagonal or, sometimes, a square lattice in two dimensions and have a rounded shape. The average number of nearest neighbors of the PbSe QD in the arrays is about 6. The separation distance between the QDs is estimated: the STM topography image is transformed to a two-dimensional Fourier image like that shown in the inset of Fig. 3.3(c); the radially average intensity of the fast Fourier transform image is calculated and displayed in Fig. 3.3(c) to give a peak which indicates a special periodicity of ~ 16.3 nm between the centers of two PbSe QDs. In particular, the fast Fourier transform image in the inset of Fig. 3.3(c) clearly exhibits 6 dots, symptomatic of a hexagonal lattice. Since the average diameter of the PbSe QDs is 14.6 nm, the separation distance between two PbSe QDs is evaluated to be 1.7 nm,

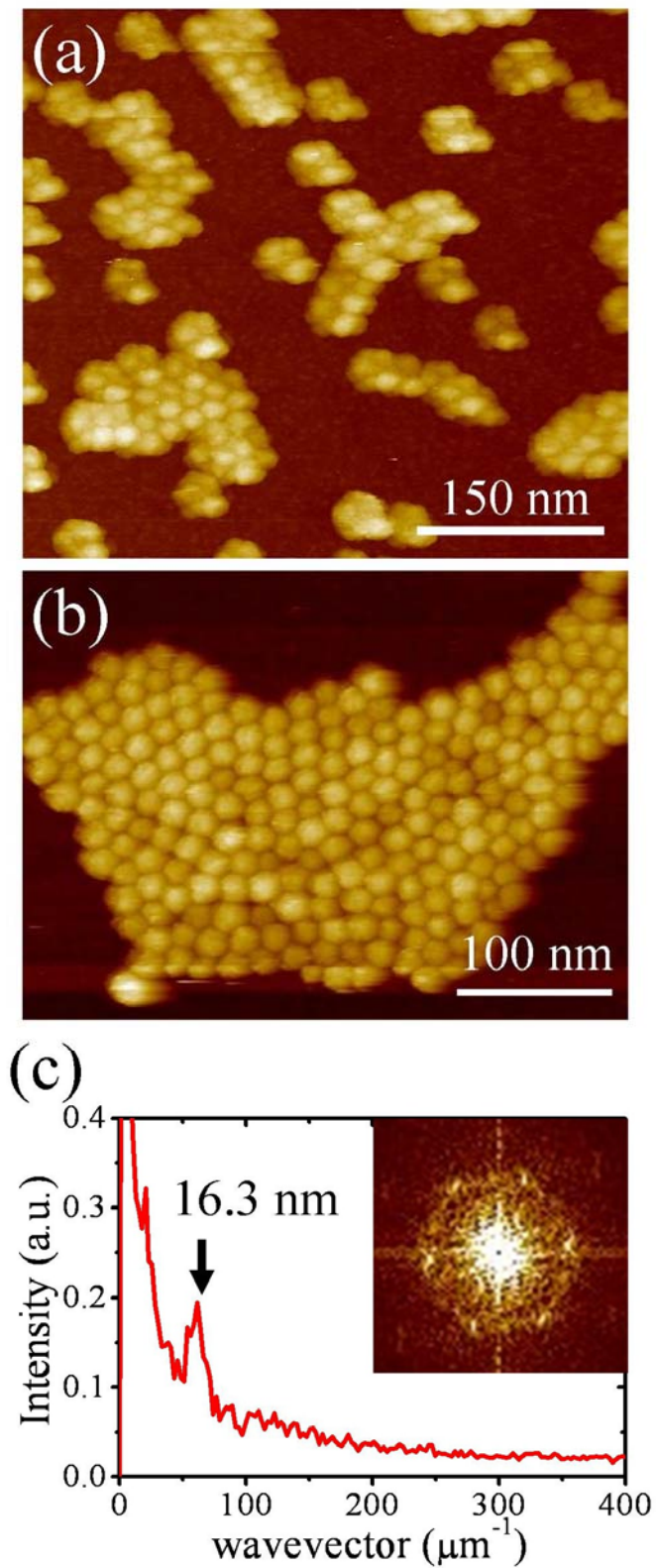


Figure 3.3: (a) STM image of PbSe QD arrays dispersing on a gold surface. (b) A two-dimensional PbSe QD array with 229 QDs on the Au(111) surface. (c) Radially averaged intensity of the two-dimensional Fourier transformed image displayed in the inset.

which is about one layer of organic molecules of the TOP and oleic acid.

3.4.1 Double tunnel junction model

We examined I - V behavior of a single QD and analyzed the data based on the orthodox theory [79] of correlated electron tunneling before investigating the electronic structure of the PbSe QD arrays. The STM image of a single QD and the double-barrier tunnel junction model for the orthodox theory are given in the inset of Fig. 3.4. A STM tip is schematically drawn above the STM image of the single QD to illustrate the corresponding tip-to-dot and the dot-to-substrate resistances (R_1 and R_2) and capacitances (C_1 and C_2) in the circuit diagram. Fig. 3.4 displays data points of an I - V curve for the single QD shown in the inset. The data are averaged from 221 I - V curves as well as CITS image points, and they exhibit a large Coulomb blockade with a V_{th} of about 1 V. In this study, gate voltage induced polarization charge Q_0 can be small enough so that a larger V_{th} was able to be observed. In addition, both experimental data and fitting curve show rounded I - V at V_{th} owing to thermal fluctuations at room temperatures. The experimental data can be fitted with the orthodox theory at 300 K to give a polarization charge Q_0 of 0.07 e, R_1 and R_2 of 2.18 and 1.14 G Ω , and C_1 and C_2 of 0.065 and 0.071 aF, respectively. The parameters justify the V_{th} of 0.96 V according to the relation $V_{th} = (0.5e + Q_0)/\max\{C_1, C_2\}$, where e is the electron charge [99]. Both R_1 and R_2 , the shunt resistances, are larger than the quantum resistance h/e^2 (where h is Plank's constant), to ensure the electron tunneling rather than the forming of conduction channels among the STM tip, PbSe QD, and substrate. The charging energy estimated from the shunt capacitances C_1 and C_2 is 588 meV, which is considerably large in contrast with a thermal energy of ~25 meV at

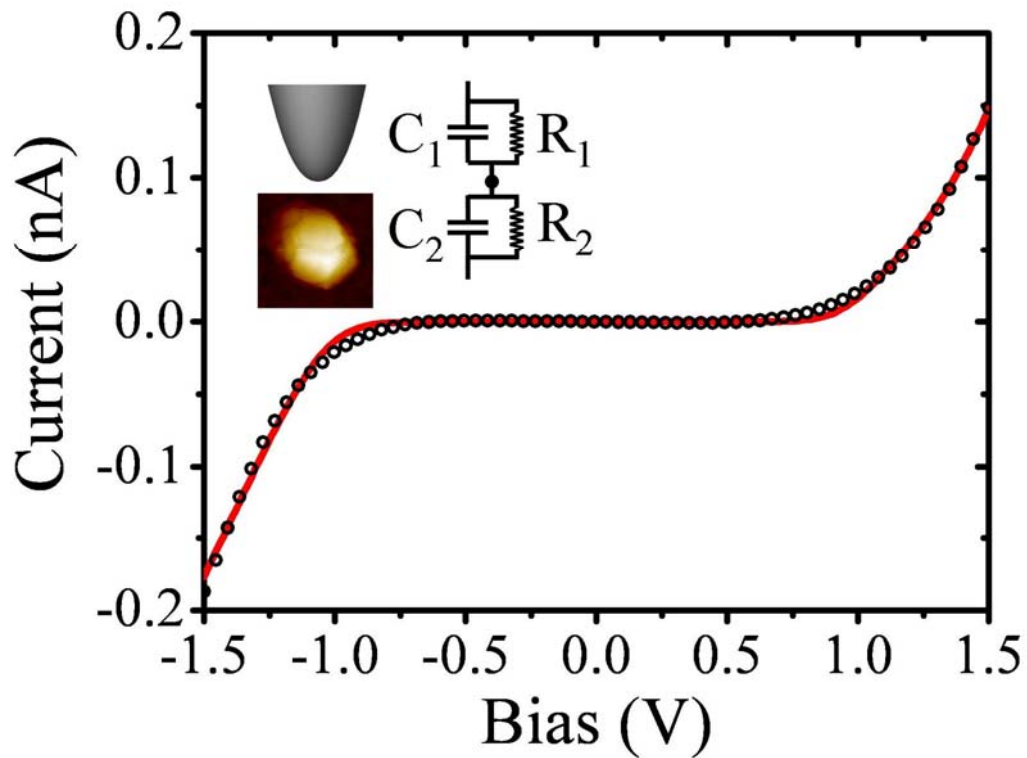


Figure 3.4: I - V curve of the single PbSe QD on the gold surface. The open circles denote experimental data, and the red line gives the best fit to the orthodox theory. The insert gives a scheme of a tip and an STM image ($44 \times 44 \text{ nm}^2$) showing the single PbSe QD on which the I - V curve is taken. A circuit diagram is shown in the insert as well.

room temperatures, so the Coulomb blockade effect is robust and detectable. In comparison with a previous report [96], the capacitances C_1 and C_2 are in the same order of magnitude while the resistance R_2 is 1000 times higher, implying an existence of organic ligands, such as TOP and oleic acid, between the QD and the substrate even after ultrahigh vacuum annealing.

The analysis of the tunneling spectrum of a single PbSe QD shows that our tip-QD-substrate system can be modeled by the double-barrier tunnel junction model and the orthodox theory. Thus, we turn to examine the tunneling spectra of QD arrays. To analyze the tunneling spectra using the orthodox theory, we start with the assumption of taking the QD array as a simple island. Several hundred of CITS image points (I - V curves) are averaged to get one characteristic I - V curve. The I - V curve of a specified QD array is fitted to obtain the double-junction parameters, C_1 , C_2 , R_1 , and R_2 . The parameters of shunt capacitances and resistances as a function of sizes (QD numbers) are given in Fig. 3.5, panels a and b, respectively. As the QD number increases from 1 to 80, the tip-to-array capacitance C_1 remains constant (~ 0.05 aF) while the array-to-substrate capacitance C_2 steadily rises from ~ 0.06 to ~ 0.10 aF. The constant C_1 suggests that the STM tip could be modeled as a sphere with a lateral dimension which is almost the same as the QD diameter. The increment of the QD number does not change the effective area of the tip-to-array capacitance so the C_1 keeps the same value. On the other hand, the effective area of the array-to-substrate capacitance expands about 80 times but the C_2 only duplicates its value. The retarded ascent of the C_2 implies that the QD array cannot be taken as a simple island. Unlike previously observed phenomena of delocalized electrons and holes among the QDs [23, 24], the electron and hole in the PbSe QD can only tunnel to, or introduce polarization charges in, neighboring QDs instead of forming direct conducting channels. The tunneling and capacitive coupling among PbSe QDs could lead to

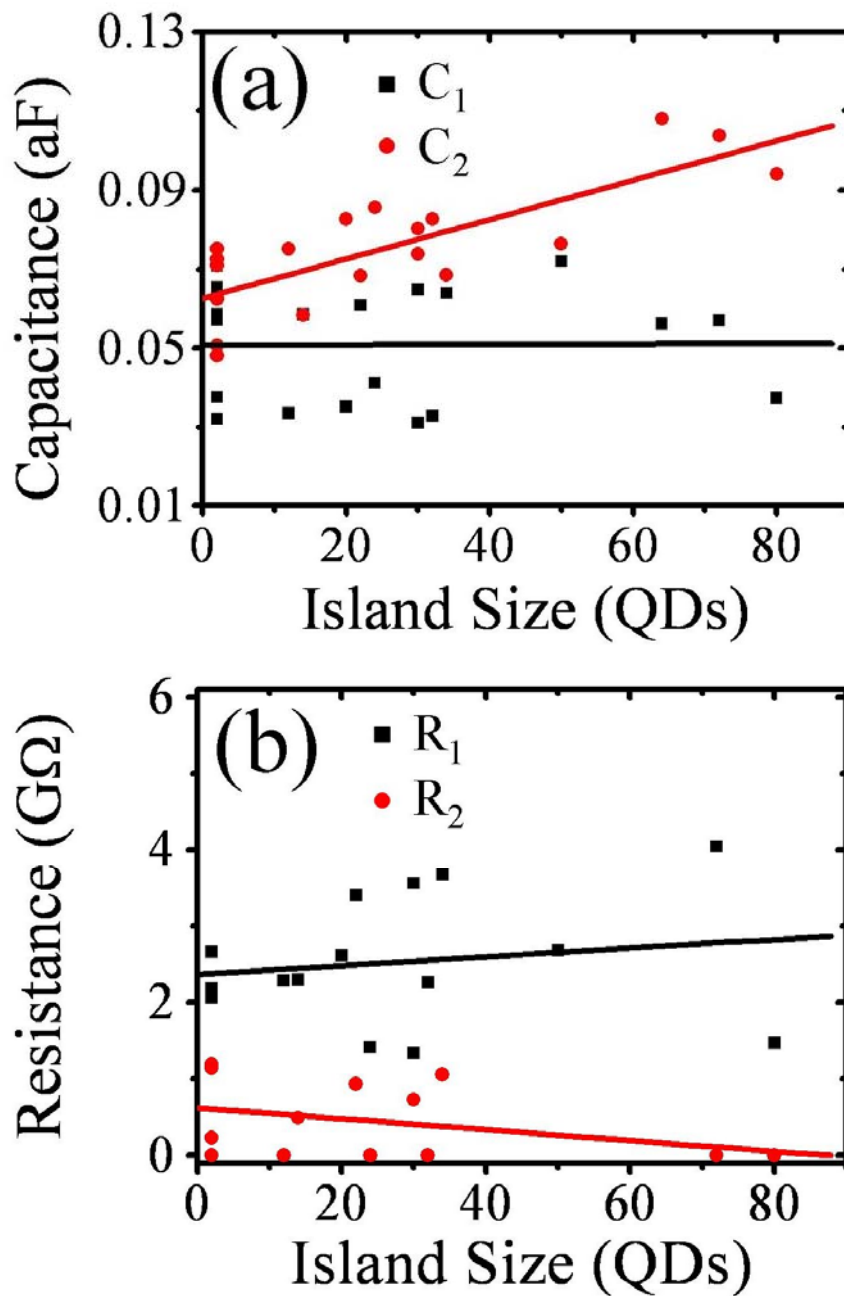


Figure 3.5: Shunt capacitances C_1 and C_2 (a) and resistances R_1 and R_2 (b), estimated from fittings with the orthodox theory, revealing a dependence on the number of QDs. The approaching lines only give a guide to the eye.

collective transport, which will be discussed later, in the QD arrays. Like the behavior of the C_1 , the tip-to-array resistance R_1 seems to be independent of the number of QDs in the array because the scanning parameters, such as the tunneling current and sample bias, remain the same to keep a separation distance between the STM tip and the QD array. On the other hand, the averaged array-to-substrate resistance R_2 decreases moderately from ~ 0.61 to ~ 0.056 G Ω . The apparent diminution of the R_2 could stem from parallel-connected tunneling resistances among the PbSe QDs and between the QDs and the substrate.

3.4.2 MW model

As mentioned above, the separation distance between two QDs can be evaluated to be about 1.7 nm which guarantees that the two QDs are still in the tunneling regime. In addition, we assume that the QDs have a cubic structure with a square face area A of ~ 214 nm² and the QDs are arranged to admit a face-to-face separation distance d of ~ 1.7 nm. By using the model of parallel plate capacitor, we can estimate the dot-to-dot coupling capacitance $C_{ij} = (\epsilon_r \epsilon_0 A)/d$ to be about 2.26 aF, where ϵ_0 is the dielectric constant in vacuum and ϵ_r is 2.1 for organic ligands (TOP) [2, 100, 101]. The interdot capacitance C_{ij} provides a charging energy of ~ 35 meV which supports the feasible observance of Coulomb blockade at room temperatures.

In Fig. 3.6(a), we illustrate electron transport in this particular system consisting of a STM tip, a PbSe QD array, and a substrate. The electrons tunnel from the STM tip to one of the PbSe QD in the array while the electrons in the tip-positioned PbSe QD couples to neighboring QDs through electron tunneling and interdot capacitor C_{ij} induced polarization. Since every QD may have a different polarization charge Q_0 to

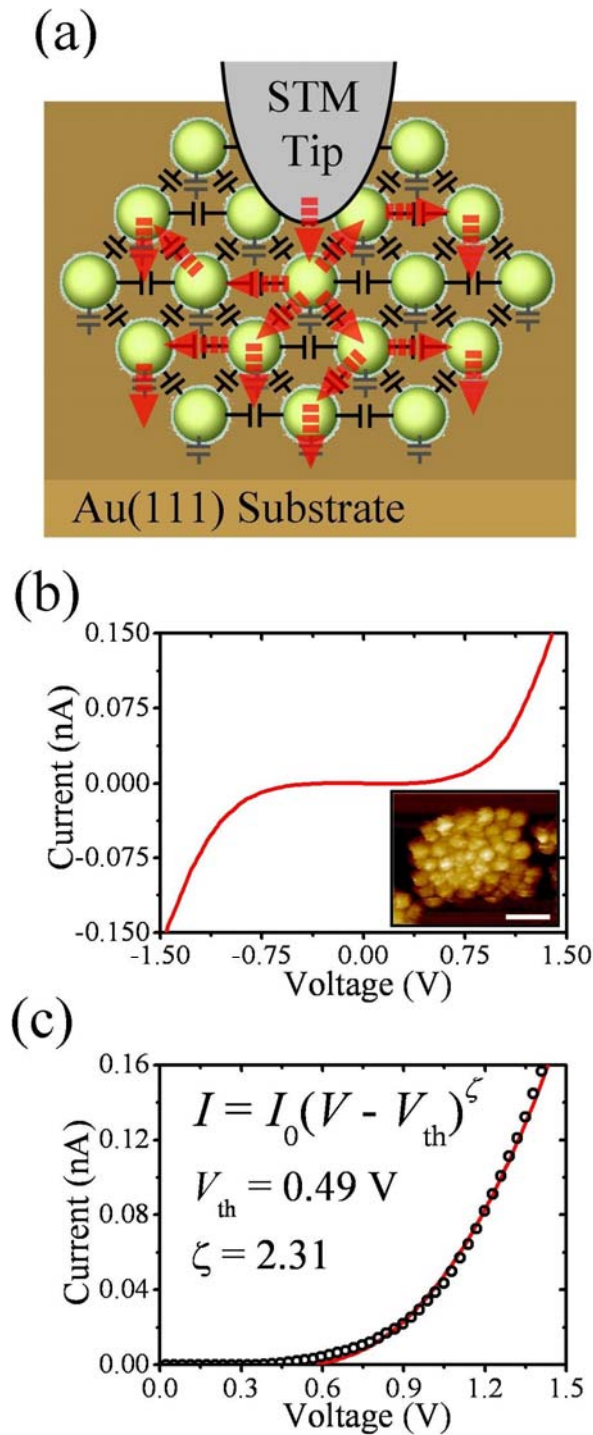


Figure 3.6: (a) Schematic illustration of the model of collective transport. The spheres denote PbSe QDs. The black and gray thin lines indicate the interdot and dot-to-substrate capacitances, respectively. The dashed thick lines with arrows illustrate electron transport (b) The I - V curve of an array consisting of 43 PbSe QDs. The inset displays its STM topography image with a 50 nm scale bar. (c) Experimental data (open circles) and a fitting curve (solid line) according to the indicative power law function. The nonlinear least square fitting gives the parameters of the threshold voltage and the scaling exponent designated in the inset.

render a disorder in the QD array, we may adopt MW model [29] to analyze collective transport in this system. As an electron tunnels from the STM tip to the QD array, it will tunnel to a QD having far less polarization charge in order to reduce the Coulomb charging energy. In addition, as compared with the tip-to-array and array-to-substrate capacitances, the interdot capacitance (2.26 aF) is two orders of magnitude larger to have a smaller Coulomb charging energy. The electron could tunnel to a nearest neighbor QD to reduce the high Coulomb charging energy in the PbSe QD situated in between the STM tip and the gold substrate. As pointed out in the MW model [29], a comparatively large interdot capacitance gives rise to a long screening length in the QD array and a decrease in the threshold voltage V_{th} per QD. When the bias voltage is higher than V_{th} , the electron will find the best way, shunting high charging energy, to transport between the STM tip and the substrate. When more and more current paths are opened with an increasing bias voltage, the $I-V$ will follow the proposed power law function. In particular, unlike the parallel array discussed in the model that has one dimension in parallel with electron transport direction, our system, comprising two dimensions in perpendicular to electron transport direction, can be regarded as a perpendicular array. Fig. 3.6(b) presents the characteristic tunneling spectrum ($I-V$) of a PbSe QD array consisting of 43 QDs on a flat gold surface at room temperatures. The characteristic $I-V$ reveals a symmetric feature about zero voltage and contains a zerocurrent, Coulomb blockade voltage range, a threshold voltage V_{th} above which the current starts to flow across the QD array, and a high voltage range with a large current implying, open conduction channels. The characteristic $I-V$ is symmetric so only the current in the positive voltage range is analyzed based on the scaling power law $I \propto (V - V_{th})^\zeta$ of the MW model. Fig. 3.6(c) shows experimental data (open circles) and a nonlinear least square fitting curve (a solid line) to demonstrate that our $I-V$ data are in concordance with the scaling law proposed in the MW model. The parameters,

the threshold voltage V_{th} and scaling exponent ζ , can be estimated after fitting. The threshold voltage $V_{th} = 0.49$ V seems to be in line with a Coulomb blocking voltage from the tip-toarray and array-to-substrate capacitances. Furthermore, the estimated scaling exponent $\zeta = 2.31$ is in the range of those obtained from two-dimensional arrays [2, 32], which give ζ between 2.2 and 2.7, and it is smaller than those evaluated from three-dimensional [35, 33] arrays ($2.5 < \zeta < 4.5$).

Characteristic I - V 's of PbSe QD arrays with various numbers of QDs were obtained at both room temperature and 78 K, and the data were fitted with the power law function $I \propto (V - V_{th})^\zeta$ to extract the V_{th} and ζ . Fig. 3.7(a) and (b) show the V_{th} and ζ dependences on the array size as well as the number of QDs at room temperatures. As the QD number of the array rises from 1 to 80, the threshold voltage V_{th} gradually decreases and the scaling exponent ζ goes up slightly. A large interdot capacitance implies a strong coupling between the QDs and a long screening length in the PbSe QD array, so the addition of extra QDs could be used to examine the reduction in V_{th} due to the interdot capacitive coupling. From about 0.7 V for a single QD, the V_{th} drops to 0.5 V for an array containing 71 PbSe QDs. Meanwhile, ζ goes up in value from about 2.1 to 2.3, suggesting more current paths opened in a high bias voltage with the addition of PbSe QDs into the array. The dependence of both V_{th} and ζ on the array size seems to be in line with the theoretical arguments of the MW model. In addition, the V_{th} and ζ estimated at room temperature are scattered and we thus repeat our experiments at 78 K and display the V_{th} and ζ in Fig. 3.7(c) and (d), respectively. The scattering in the V_{th} and ζ is, in particular, abated for data taken at 78K due to the reduced thermal fluctuation. Before we go ahead to discuss the low-temperature data, we should address the quantitative validity of our data. Fig. 3.7(a) and (b) present a rather large standard deviation in V_{th} and ζ and, thus, the least square fitting line can only give a rough tendency. The data shown in Fig.3.7(c) and (d), however,

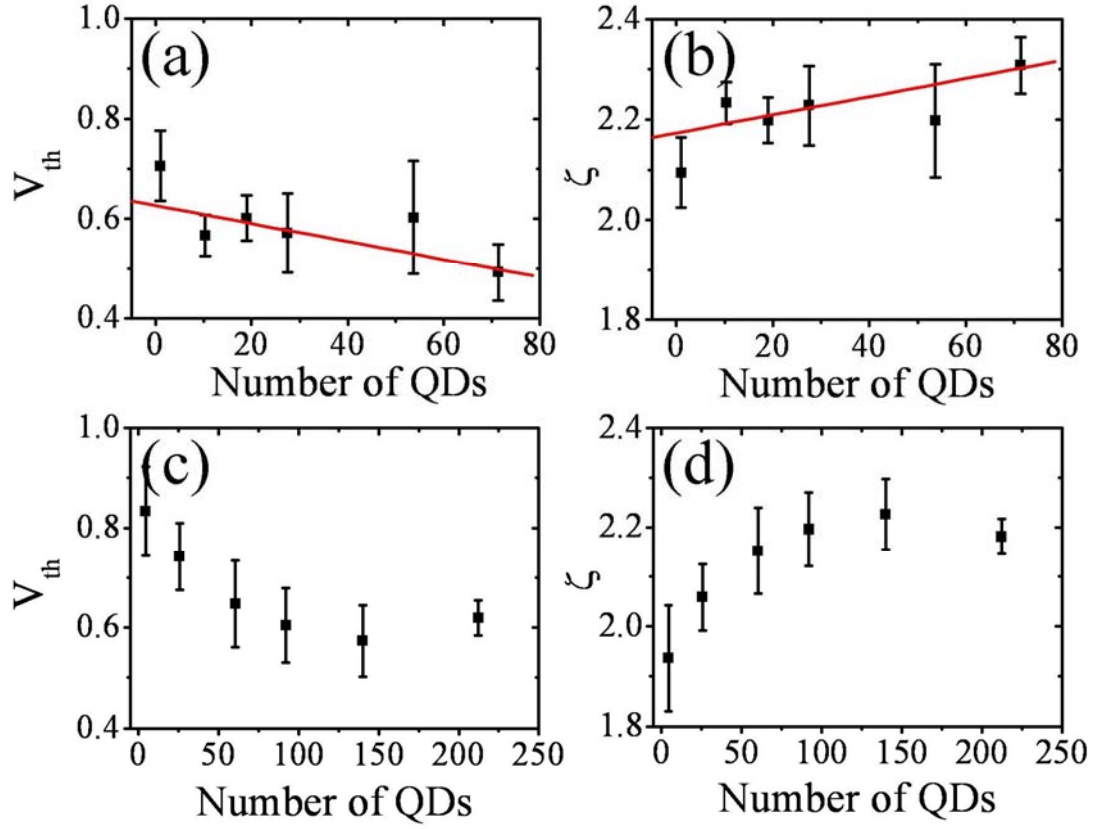


Figure 3.7: Threshold voltages V_{th} ((a) and (c)) and scaling exponents ζ ((b) and (d)) as a function of the QD number. The data in (a) and (b) ((c) and (d)) are estimated from fitting to I - V curves taken at room temperature (78 K). The solid lines in (a) and (b) give the best linear least square fits to our data.

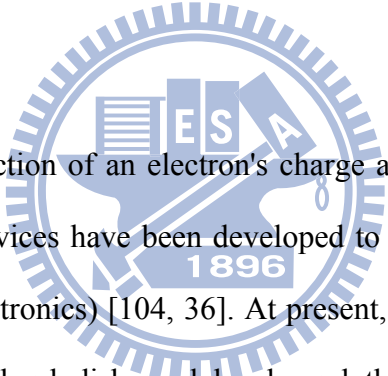
demonstrate a noticeable decrease and an increase in the V_{th} and ζ , respectively. The variation trend, which is in agreement with the room-temperature data, is much clearer since the change in the V_{th} and ζ as a function of a QD number is larger than the value of the standard deviations. We consequently confirm that our data can give a quantitative validity to examine the theoretical model. Additionally, it is noteworthy that the V_{th} and ζ at 78 K still reveal appreciable error bars, possibly resulting from the size distribution of PbSe QDs.

The single QD V_{th} and ζ taken at 78 K shift to about 0.8 V and 1.9 (Fig. 3.7(c) and (d)) in comparison with $V_{th} = 0.7$ V and $\zeta = 2.1$ at room temperatures (Fig. 3.7(a) and (b)). We believe that a small thermal fluctuation helps to widen the Coulomb blocking voltage (V_{th}) and to reduce the thermally excited current paths (ζ). For the data taken at 78 K, the V_{th} decrease from 0.8 to 0.6 V while the ζ increase from 1.9 to 2.2 when the QD number of the array increases from 1 to 220. The size dependency at 78 K conforms to that observed at room temperature when the QD number of the array is less than 100. In addition to the change in the V_{th} and ζ as a function of the QD number, we notice, as well, a saturation trend in both the V_{th} and ζ for PbSe QD arrays containing a number of QDs larger than 100. The result seems to agree well with the theoretical argument of a strong interdot coupling, resulting in a long capacitive screening length. When the QD number or size of the array is comparatively larger than the screening length, the collective Coulomb blockade effect will not be altered further and both the V_{th} and ζ will reach saturated values. The limit of collective transport appearing in a finite screening length is revealed for the first time.

Chapter 4

Ferromagnetism in $\text{Zn}_{1-x}\text{Co}_x\text{O}$ nanowires

4.1 Introduction



The manipulation and detection of an electron's charge and, simultaneously, its spin orientation in electronic devices have been developed to be a new emerging field of spintronics (or magnetoelectronics) [104, 36]. At present, the most notable spintronic applications could be the hard disk read heads and the magnetic random access memory which are based on metal magnetic materials and are assorted into metallic spintronic devices. The establishment of metallic spintronics might be ascribed to a discovery of giant magnetoresistance [105, 106] and, subsequently, understanding and exercise of a spin-valve scheme [107], and tunnelling magnetoresistance [108] in ferromagnetic multilayers. On the other hand, in order to integrate with the modern industrial technology, new semiconductor materials such as diluted magnetic semiconductors (DMSs) [109], also known as ferromagnetic semiconductors [110], have been searched for a supply of a spinpolarized carrier source. Those devices building on a transport of spin current in semiconductors are categorized into semiconductor spintronics. Spin injection, maintenance of a spin coherence, spin

detection, and a spin carrier source in semiconductors are all important issues for semiconductor spintronics.

The DMSs, based on host materials of II-VI and IV-VI semiconductors, have been studied for several decades. Although the indirect exchange mechanisms between $3d$ transition metal dopants in these semiconductors have been inspected experimentally and discussed theoretically [109, 111, 112] for a long time, the Curie temperature (T_C), below which a spontaneous magnetization and a spin-polarized current in the DMSs arise, was too low to be capable of employment. Until recent advance in III-V DMSs of (In,Mn)As and (Ga,Mn)As [113], T_C 's of some new DMSs such as (Ga,Mn)As have been raised up to ~ 110 K. These new III-V DMS materials were exploited to demonstrate tunneling magnetoresistance in (Ga,Mn)As ultrathin heterostructures [114], electrical spin injection in a ferromagnetic semiconductor heterostructure [115], electric-field control of ferromagnetism [116], electrical manipulation of magnetization reversal [117], and current-induced domain-wall switching [118]. On the other hand, the other approach of spin-current injection into semiconductors from ferromagnetic metals has recently been achieved, so as to realize semiconductor spintronics at room temperature.

By using Zener model description, Dietl et al. [38] have theoretically sustained the fact of a 110-K high T_C for p -type (Ga,Mn)As with a manganese concentration of just 5%. In addition, they argued the presence of a T_C above room temperature in Mn doped ZnO or GaN with hole carriers of $3.5 \times 10^{20} \text{ cm}^{-3}$. These theoretical arguments drew much attention on search for room-temperature ferromagnetism (RTFM) in new DMS materials. For example, Matsumoto et al. [119] discovered RTFM in Co doped TiO₂ with a magnetic moment of 0.32 Bohr magneton (μ_B) per Co atom and Toyosaki et al. [120] observed anomalous Hall effect in this particular material. Else, Ueda et al. described ferromagnetism and a T_C above 280 K in pulse laser deposited $\text{Zn}_{1-x}\text{Co}_x\text{O}$

films [39]. Cho et al. found ferromagnetic and antiferromagnetic ordering in $(\text{Zn}_{1-x}\text{Mn}_x)\text{GeP}_2$ at temperatures up to 312 K and below 47 K [121], respectively. Among all new as-proposed DMS materials, Co-doped metal oxides, such as $\text{Ti}_{1-x}\text{Co}_x\text{O}_2$ and $\text{Zn}_{1-x}\text{Co}_x\text{O}$, seem to be an appropriate candidate for a spin-polarized carrier source at room temperature [122].

ZnO is recently a hot material and it is proposed to be valuable in many application fields such as blue/ultraviolet optoelectronics [123, 124]. It is a direct and wide band gap semiconductor and can be easily over-doped to form conductive and transparent films. ZnO is natively *n*-type doped to show relatively lower resistivity due to difficulties in control of point defects during the growth process. In addition, it shows ultraviolet (near band edge) and green (or blue) defect emission at ~ 3.2 and ~ 2.5 eV, respectively, in photoluminescence (PL) spectra. It is proposed that oxygen vacancies [125], zinc interstitials [126], $\text{Zn}_i\text{-N}_o$ complexes [127], metastable conductive states [128], or hydrogens [129] can lead to the native *n*-type doping, the coloration, and the green emission. The point defects not only result in an increase of conductivity but also modulate magnetic ordering after ZnO is doped with paramagnetic 3*d* transition metal dopants.

There are so many experimental and theoretical reports on claiming that Co-doped ZnO is an intrinsically DMS [43-44, 130-131]. Very recently, different magnetic mechanisms are uncovered in insulating and magnetic regimes [132]. In particular, magnetic resistance has been observed in a magnetic tunnel junction fabricated by using Co-doped ZnO as one ferromagnetic electrode [133]. There are, however, other contradictory reports exposing antiferromagnetism [134], secondary phases in crystalline structure, clustering of Co metals or ions [46], or absence of ferromagnetism in this material. On the other hand, even for similar conclusions of ferromagnetism in this material, the Curie temperature either above or below the room temperature is

another issue. As we have emphasized, it is difficult to control point defects in ZnO during growth. Moreover, electrical resistivity and PL emission of a pure ZnO, and a magnetic ordering of a Co-doped ZnO can all be altered by thermal annealing after growth. Here we propose the employment of nanowires (NWs) for an exploration into magnetism because, after converted to a nanophase, the nanomaterials have a large surface to volume-ratio, feasible for thermal treatments, and they are handy for a structural characterization by using transmission electron microscopy.

In our previous reports, we have observed the structure and annealing effect on ferromagnetic ordering in $Zn_{1-x}Co_xO$ NWs [49, 50]. In this chapter, we present characterizations, including structure and magnetic property measurements on pure ZnO NWs, as-implanted $Zn_{1-x}Co_xO$ NWs, annealed $Zn_{1-x}Co_xO$ NWs, and a comparative sample of ZnO NWs sheathed in amorphous carbon with Co clusters, so as to explore the mechanism of RTFM in the DMS of $Zn_{1-x}Co_xO$ NWs and their size dependent behavior. Furthermore, we have employed magnetic force microscopy to observe the magnetic domain structure in individual $Zn_{1-x}Co_xO$ NWs.

4.2 Theoretical background

In this section, we briefly survey some models for explanation of ferromagnetism in diluted magnetic semiconductor. Then we introduce the behavior of superparamagnetism in single domain system. Finally, we demonstrate an analytic method for magnetic force microscopy which is applied to fit out data.

4.2.1 Ferromagnetism in diluted magnetic semiconductor

The origin of ferromagnetism in diluted magnetic semiconductor (DMS) has drawn intense interest and theoretical argument since the magnetic dipole moments, provided by the implanted transition metal ions, are separated too far to generate the exchange interaction. In the spirit of RKKY theory, a mechanism of carrier-induced ferromagnetism has been proposed in which the localized spins are coupled with the mediating of free carrier [37, 138]. For the case of insulating or low carrier concentration DMS, the ferromagnetism is taken into account the disorder of the magnetic impurities, in which the carriers are allowed to hop only between the transition metal dopants [139]. The localized spins due to the transition metal ions interact with a much lower number of weakly bound carriers, leading to bound magnetic polarons (BMP) [140]. On the basis of BMP picture, Coey *et al.* proposed that the ferromagnetic exchange in dilute ferromagnetic oxides or nitrides, such as Co ions doped in GaN, TiO₂, and ZnO matrix, is mediated by shallow donor electron [44]. The carrier generated by the donor defect is confined in a hydrogenic orbital with a range of five to nine angstrom. As the number of donor defect increases, the hydrogenic orbitals overlap to form an impurity band, which interacts with the 3d orbits of magnetic cation leading a ferromagnetic exchange coupling. Fig. 4.1 shows a schematic diagram of bound magnetic polaron in ZnO doped with Co ions. The white circles represent nonmagnetic cations, Zn, and some cation sites are replaced by magnetic cations, Co, which are represented by red circles with an arrow representing a magnetic moment. The rectangles represent the oxygen vacancies which donate excess electron to form hydrogenic orbitals, which is represented by large blue circles. The magnetic moments with the hydrogenic orbitals are ferromagnetic coupled to form a ferromagnetic domain.

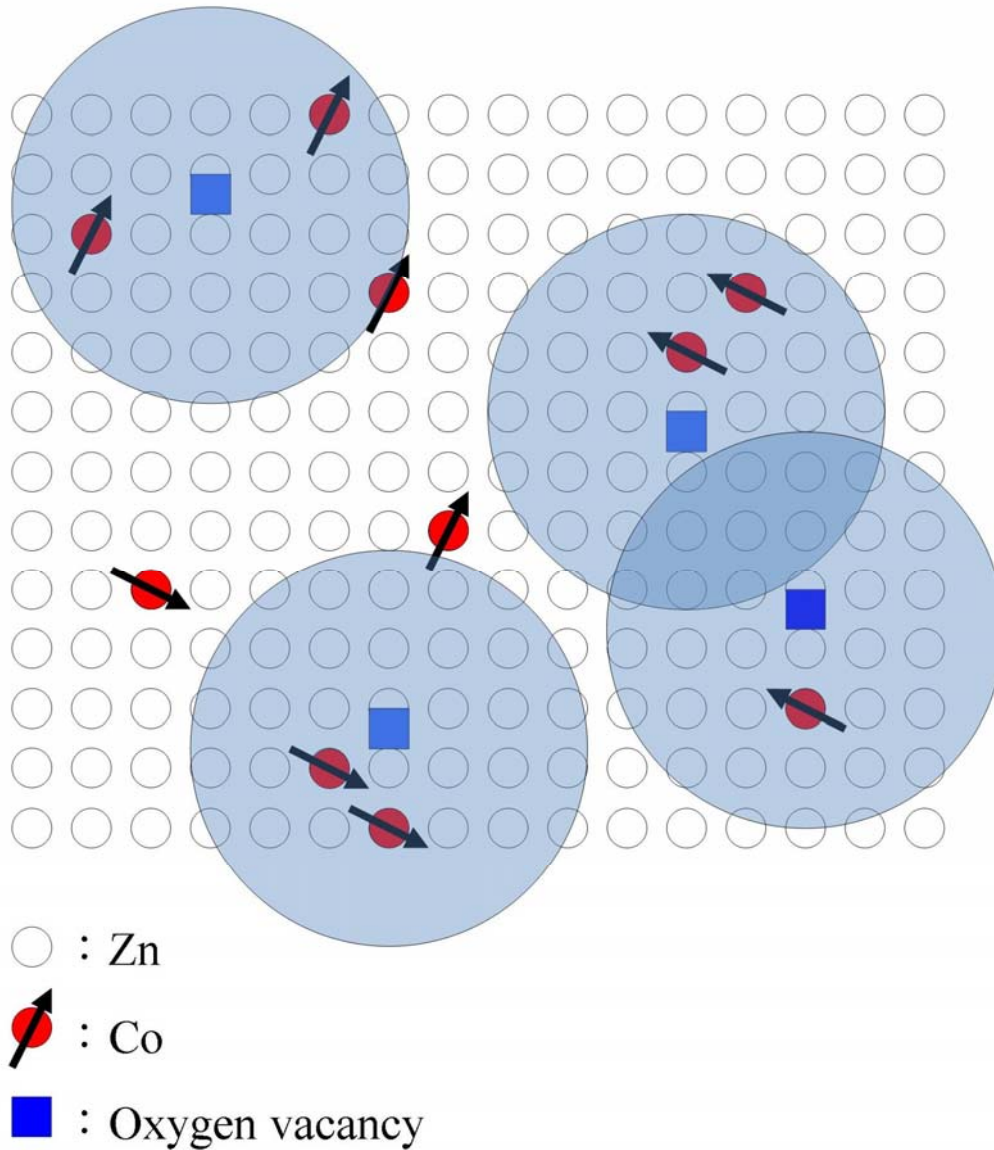


Figure 4.1: The schematic diagram of bound magnetic polaron in ZnO doped with Co ions. The white circles represent Zn atom. Co ions are represented by red circles with an arrow representing a magnetic moment. The rectangles represent the oxygen vacancies which donate excess electron to form hydrogenic orbitals, which is represented by large blue circles.

4.2.2 Superparamagnetism

To reduce the total energy, the sum of the magnetostatic and domain wall energy, a bulk ferromagnetic crystal tends to spontaneously break into a number of domains forming a multi-domain structure [137]. As the crystal becomes smaller, the domain wall energy becomes considerable in comparison with the magnetostatic energy. Thus the single-domain is the lowest total energy state for a tiny ferromagnetism crystal. For a small single-domain particle, its anisotropy energy would become so small that could be overcome by the thermal fluctuation. The temperature at which the thermal energy overcomes the anisotropy energy is called “blocking temperature”, T_B . The spontaneous magnetization of a single-domain particle is destroyed to exhibit a “superparamagnetic” state at the temperature above T_B . Experimentally, we can observe some behaviors in a superparamagnetic system. First, when the magnetization is plotted as function of H/T , the curves measured at different temperatures will superimpose. It can be understood that the magnetization of a paramagnetic system is a function of the variable $\mu H/k_B T$. Second, the coercivity will shrink with the temperature and obey the relation

$$H_C(T) = H_C(0)[1 - (T/T_B)^{1/2}]. \quad (4.1)$$

When the temperature is higher than T_B , there is no hysteresis. Third, the field cooled and zero-field cooled (FC-ZFC) measurements show a “Lambda shape” and usually the branch point is indicated as the blocking temperature T_B . Fig. 4.2 shows a typical FC-ZFC curve of a single domain system. This behavior comes from the random oriented dipole moments in a superparamagnetic system at low temperature are unblocked with the increasing temperature. At the same time, the magnetization resulted from the unblocked dipole moments is weakened by the thermal fluctuation.

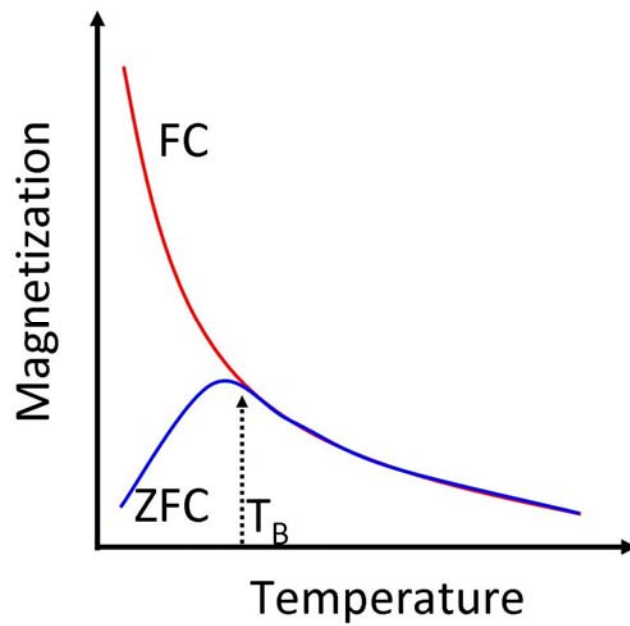


Figure 4.2: The typical FC-ZFC curve of a superparamagnetic system with Lambda shape. The branch point of the curve indicates the blocking temperature.

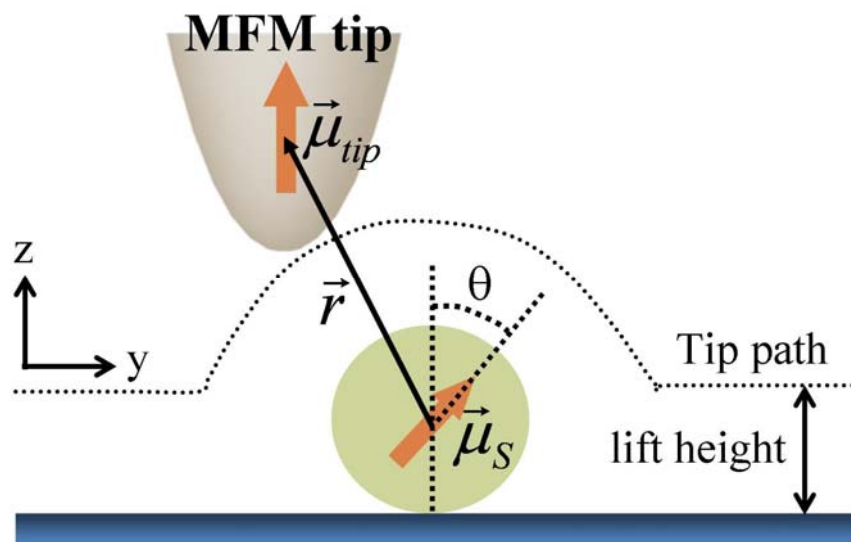
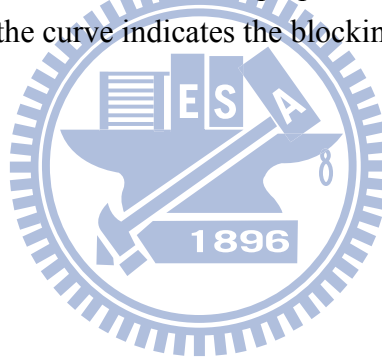


Figure 4.3: The schematic for modeling the tip and sample as two point magnetic dipoles. The origin of this coordinate is at the center of sample.

4.2.3 Magnetic force microscopy

Nowadays a tapping/lift technique is usually employed for magnetic force microscopy. This technique allows us to take topographical and magnetic data simultaneously by scanning twice on the same scan line. The first scanning, which is very close to the sample surface, is a normal tapping mode for taking the topographical data. When performing the second scanning, the tip follows the same trajectory of the first scanning and is lifted with a distance, typically 10 to 100 nm, to eliminate the contribution of Van der Waals force. A MFM image usually records the phase of tip oscillation. As the oscillation is subjected to a force, the phase difference $\Delta\delta$ obeys the relation

$$\Delta\delta = \frac{Q}{k_e} F', \quad (4.2)$$

where Q is the quality factor, k_e is the spring constant, and F' is the force gradient.

A method was proposed for analyzing MFM data which modeled the tip and sample as two point magnetic dipoles [141, 143]. Fig. 4.3 shows the schematics of this model. Consider a tip with a dipole moment m_{tip} is magnetized along the z axis, there will be a force gradient acting on the tip

$$F' = \nabla(m_{tip} \cdot \vec{H}_s) = m_{tip} \frac{\partial^2 (\vec{H}_s \cdot \hat{z})}{\partial z^2}, \quad (4.3)$$

where \vec{H}_s is the stray field comes from the sample, and \hat{z} is the normal direction of the surface. The stray field \vec{H}_s of the sample at the position of tip \vec{r} is

$$\vec{H}_s = \frac{3(\vec{\mu} \cdot \vec{r})\vec{r}}{r^5} - \frac{\vec{\mu}}{r^3}, \quad (4.4)$$

where $\vec{\mu}$ is magnetic dipole moment of sample. In yz plane, which means $x = 0$, the $\vec{r} = x\hat{x} + y\hat{y} + z\hat{z}$ and $\vec{\mu} = m_s(\sin\theta\hat{y} + \cos\theta\hat{z})$. Then incorporating Eq. (4.1), (4.2), and (4.3), we obtain

$$\Delta\delta = \frac{Q}{k_e} m_{ip} m_s \left[\frac{9 \cos \theta}{(y^2 + z^2)^{5/2}} - \frac{45z(y \sin \theta + 2z \cos \theta)}{(y^2 + z^2)^{7/2}} + \frac{105z^3(y \sin \theta + z \cos \theta)}{(y^2 + z^2)^{9/2}} \right]. \quad (4.5)$$

Fitting the MFM data with Eq. (4.4), we can obtain the orientation θ and strength m_s of sample dipole moment.

4.3 Experiment

Cylindrical ZnO NWs were grown by using a vapor-phase transport process. A quartz tube treated as a growth chamber was inserted in a furnace. ZnO powders were placed in a crucible in the growth chamber and heated to 950°C. The chamber was maintained at 200 Pa with a constant flow of argon and a pumping system. For a purpose of controlling NW diameter, gold nanoparticles as catalysts with specified average diameters of 10, 20, 40, 70, and 100 nm were dispersed on quartz substrates. The substrates were positioned at the downstream end of the growth chamber and were maintained at 500-600°C. Cylindrical ZnO NWs with a controllable diameter were formed on substrates after a growth period of 8 h. The crystalline structure and morphology of ZnO NWs were analyzed by using field-emission scanning electron microscope (SEM, JEOL JSM 7000F) and transmission electron microscope (TEM, JEOL JEM-2010F).

The as-grown ZnO NWs were implanted by Co ions with doses of $(1-6) \times 10^{16}$ cm⁻². By using a tandem accelerator (NEC 9SDH-2), the implantation was performed at room temperature. An accelerating energy of 72 keV was used for NWs with average diameters larger than ~70 nm. Thinner NWs were implanted by Co ions with an acceleration energy of 40 keV. A beam current of either 150 or 600 nA/cm² was

used to make $Zn_{1-x}Co_xO$ NWs. The high beam current of 600 nA/cm^2 could somewhat turn out to be thermal treatment due to the high energy ion bombardment in a high vacuum. The chemical composition as well as Co element distribution in $Zn_{1-x}Co_xO$ NWs was inspected through energy dispersive x-ray (EDX) and electron energy loss spectroscopy (EELS) mapping. In order to study the origins of ferromagnetism in $Zn_{1-x}Co_xO$ NWs, some specimens were post-annealed in argon, in a high vacuum of 5×10^{-5} torr, or in oxygen at 600°C (or 450°C) for several hours. In particular, multiple steps of thermal annealing in a high vacuum were carried out to produce a gradual transition of magnetic states of this DMS material.

In addition to DMS $Zn_{1-x}Co_xO$ NWs, ZnO NWs sheathed in amorphous carbon with Co clusters were produced for comparison. These purposely fabricated samples were treated with the same thermal annealing process as that for DMS NWs. Co metal clusters in carbon coated ZnO NWs were intriguingly formed after a high-vacuum annealing. The morphology, crystalline structure and chemical composition of these comparative samples were analyzed in a similar way.

Magnetic properties of DMS $Zn_{1-x}Co_xO$ NWs and comparative samples (Co clusters on ZnO NWs) were measured by employing a SQUID magnetometer (Quantum Design MPMS-XL7) with the reciprocating sample option mode. Field cool (FC) and zero-field cool (ZFC) processes were conducted to obtain temperature dependent magnetization during the rising temperature sequence under an external magnetic field of 500 Oe. That is, the samples were subjected to oscillating with decreasing fields and were cooled from 300 K down to 2 K in a zero field. The samples were then warmed up to obtain ZFC magnetization as a function of temperatures in 500 Oe. They were cooled down in the same field and warmed up again to record the FC magnetization. Before NW growth, the magnetic susceptibility of a quartz substrate was estimated to be $\sim -1.1 \times 10^{-6} \text{ emu/cm}^3$ so that diamagnetic

contribution of the substrate can be subtracted from the total magnetization. Magnetic data were presented in unit of μ_B per Co where the amount of Co ions was evaluated by multiplying the ion dose per cm^2 with the substrate area.

After measurements of SQUID, the $\text{Zn}_{1-x}\text{Co}_x\text{O}$ NWs on quartz substrates were transferred to flat HOPG substrates by rubbing the two substrates with each other. The $\text{Zn}_{1-x}\text{Co}_x\text{O}$ NWs on HOPG substrate were surveyed by a field-emission SEM (JEOL JSM-7000F) to identify the location of individual NWs for taking MFM measurements. The MFM measurements and simultaneously topographic images were taken by using a scanning probe microscope (Seiko Instruments Inc., SPA 300HV) in the tapping/lift mode. A commercial magnetic tip (NanoWorld MFMR) with 40-nm thick cobalt alloy coating was used. The tip has a quality of $Q \sim 137$, a resonance frequency of ~ 75 kHz, a spring constant of $k \sim 2.8$ N/m, and a magnetic moment $m_{\text{tip}} \sim 10^{-13}$ emu. Before carrying out the MFM measurements, the tip was magnetized by placing a permanent magnet perpendicular to the cantilever at a distance of ~ 1 cm, where the stray field from the magnet was ~ 7000 Oe. The $\text{Zn}_{1-x}\text{Co}_x\text{O}$ NWs on the HOPG substrate were magnetized by the same approach in a direction perpendicular or parallel to the substrate. After the MFM measurements, the samples were in situ heated up above room temperature in high vacuum and cooled down to carry out MFM measurements again. All the MFM measurements were performed in atmosphere at room temperature.

4.4 Results and discussion

At first, we demonstrate the growth behavior, crystalline structure, and chemical

composition of ZnO NWs. A SQUID magnetometer is then employed to study annealing effect on the ferromagnetism of $Zn_{1-x}Co_xO$ NWs. Finally, we utilized MFM to verify the room-temperature ferromagnetism on an individual DMS NW.

4.4.1 Growth behavior and chemical composition

Fig. 4.4(a)-(d) display SEM images of cylindrical ZnO NWs with increasing average diameters. The cylindrical NWs with average diameters of 12, 19, 38, and 113 nm were grown by using gold-nanoparticle catalysts with average sizes of 10, 20, 40, and 100 nm, respectively. The NWs displaying in the same magnification SEM images demonstrate obviously distinct dimensions, implying a very well control of the NW diameter through the size of gold nanoparticles. All these ZnO NWs were synthesized with the same conditions of temperature and time. We found the diameter of the NWs were just controlled by and linearly depended on the size of gold catalysts. From the SEM images, we can also observe that the thinner NWs (Fig. 4.4(a) and (b)) tempted to exhibit a more bended shape in contrast to the thicker NWs being straight. Fig. 4.4(e)-(h) displays statistical distribution, which was examined from TEM images, of our ZnO NW diameters. The average diameters with statistical distributions are 12 ± 2.7 , 19 ± 3.2 , 38 ± 4.6 and 113 ± 20 nm for the various ZnO nanowires, corresponding to the standard deviations of 23%, 17%, 12% and 18%, respectively. This somewhat large deviation in NW diameter may come from a broad size distribution of the gold catalysts.

A high-resolution TEM image of an as-grown ZnO nanowire with 10-nm diameters is shown in Fig. 4.5(a). Evident atomic columns reveal single crystalline structure and the [0001] growth direction. The periodic lattice structure indicates a double layer spacing

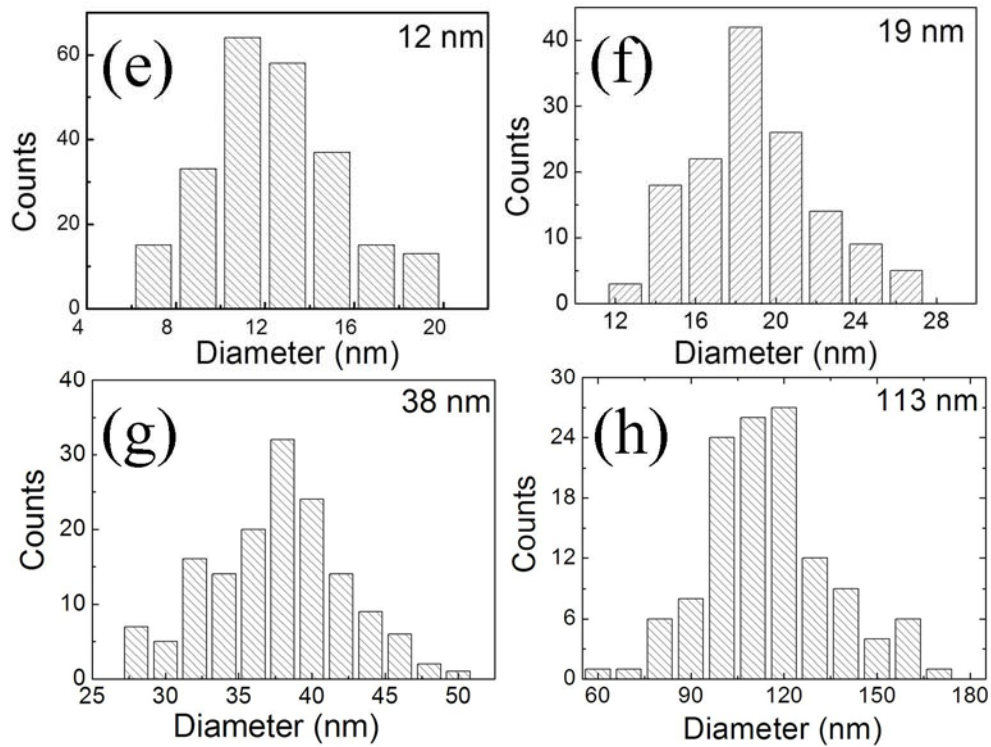
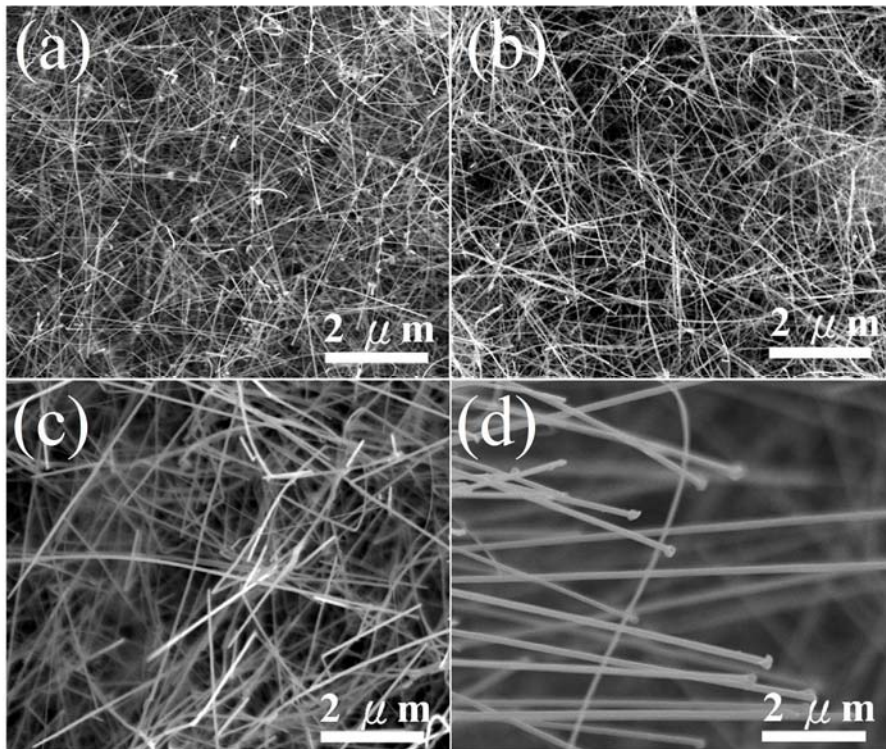


Figure 4.4: FESEM images of as-grown ZnO NWs with average diameters of (a) 12 nm, (b) 19 nm, (c) 38 nm, and (d) 113 nm. The corresponding statistical distributions are (e), (f), (g), and (h).

of 0.52 nm, in accordance with the distance between the (001) planes of the ZnO wurtzite structure. The inset of Fig. 4.5(a) shows the nano beam electron diffraction pattern of the 10-nm diameter ZnO nanowire with zone axis of $[1\bar{1}20]$. The electron diffraction pattern reveals fine dots, suggesting perfect lattice order free from those structure defects such as the orientational variations found in our previous work [49]. As-grown and pure ZnO NWs were doped by high energy Co ions to form $\text{Zn}_{1-x}\text{Co}_x\text{O}$ NWs. A TEM image of an as-implanted $\text{Zn}_{1-x}\text{Co}_x\text{O}$ NWs with an average diameter of 38 nm and a Co ion dose of $6 \times 10^{16} \text{ cm}^{-2}$ are demonstrated in Fig. 4.5(b). The as-implanted $\text{Zn}_{1-x}\text{Co}_x\text{O}$ NWs consist of lots of stacking faults, as designated by triangles in Fig. 4.5(b), and they exhibit a streaking of an electron diffraction pattern (see the inset). Although the bending feature can be detected in as-grown ZnO NWs, there are more stacking faults and an obvious streaking in an electron diffraction pattern discovered in as-implanted $\text{Zn}_{1-x}\text{Co}_x\text{O}$ NWs. It is proposed that these structure defects could mainly come from a high-energy Co ion bombardment during the ion implantation process. After a high-vacuum annealing, a TEM image of the same sample are shown in Fig. 4.5(c). We can see that the stacking faults, which were indicated as triangles, and streaking are removed after a thermal treatment. We notice that an annealing in a high vacuum at 600°C could help to recover structure disorders and defects. We also found that annealing at a higher temperature may cause a meltdown of ZnO NWs. A lower annealing temperature of 450°C was thereafter applied to subsequent experiments and no noticeable changes in morphology were observed after the thermal treatment.

In order to study the magnetic mechanism in $\text{Zn}_{1-x}\text{Co}_x\text{O}$ NWs, we have made a comparative sample, ZnO NWs sheathed in amorphous carbon by Co ion implantation. There are neither perceptible clusters nor nanocrystals before any thermal treatments. After a high-vacuum annealing, Co clusters, having a broad size distribution, could be

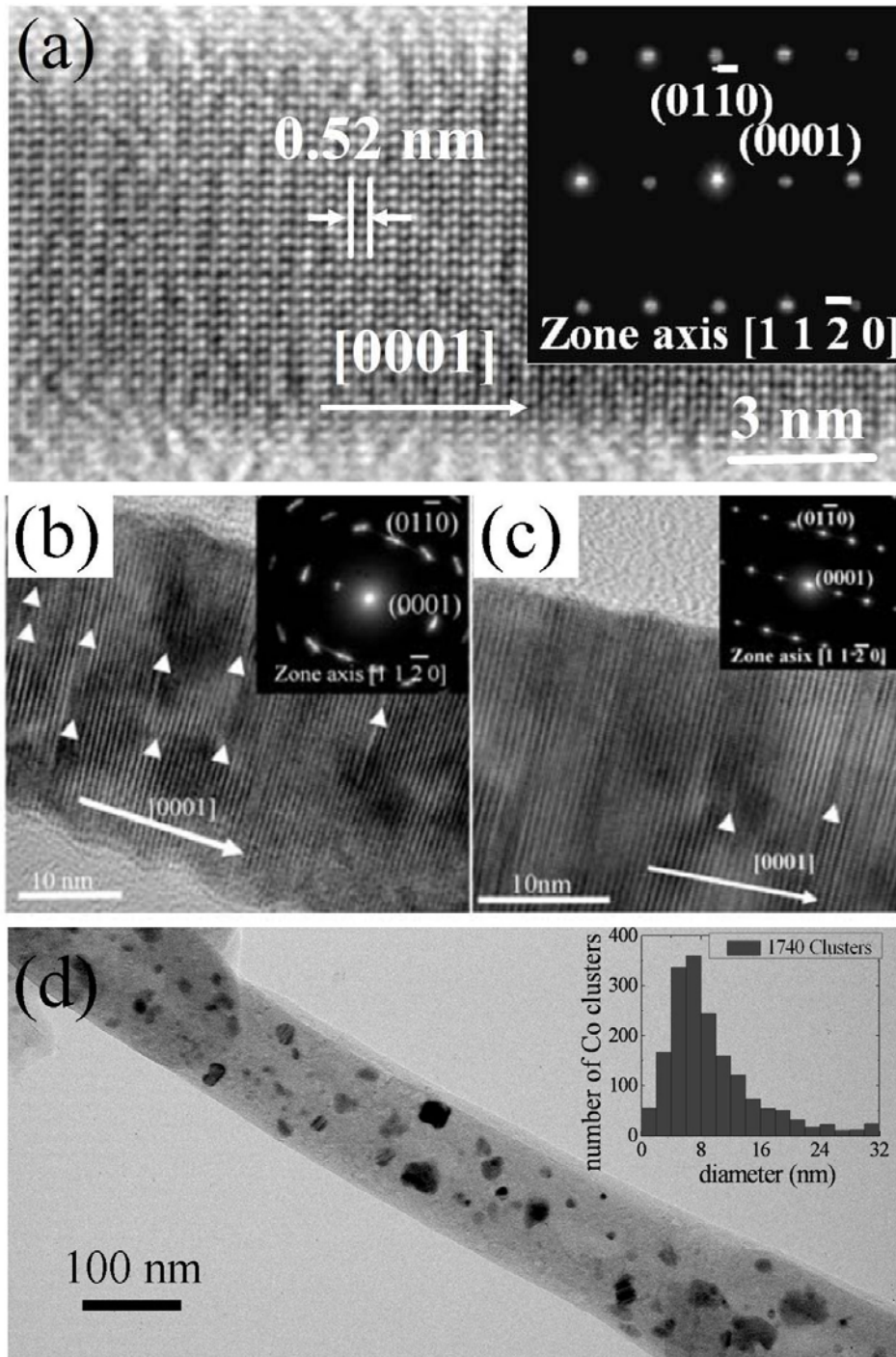


Figure 4.5: (a) High resolution TEM image of an as-grown ZnO NW with the diameter of 10 nm. The inset shows its corresponding nano beam electron diffraction pattern. High resolution TEM images of (b) as-implanted and (c) high-vacuum annealed $Zn_{1-x}Co_xO$ NWs. The inset in (b) and (c) displays corresponding electron diffraction patterns. (d) TEM image of a ZnO NW sheathed in carbon amorphous with Co clusters after high-vacuum annealing. The inset of (d) is the statistical distribution of Co-cluster diameters estimated from TEM images. The average diameter and standard deviation are 9.4 and 6.0 nm, respectively.

discovered in TEM images. Fig. 4.5(d) shows a typical TEM image of the Co clusters with a statistical distribution of diameters in the inset. The 40-nm diameter ZnO NW is embedded in a shell of carbon amorphous with a diameter of ~ 100 nm. The average diameter and standard deviation of the Co clusters are about 9.4 and 6.0 nm, respectively. This sample was fabricated by Co ion implantation with a dose of 4×10^{16} cm^{-2} and post-annealed in a high vacuum at 600°C . In contrast to the high-vacuum annealed $\text{Zn}_{1-x}\text{Co}_x\text{O}$ NWs, in which Co cluster have never been detected in TEM images (Fig. 4.5(c)), the sample of ZnO sheathed in amorphous carbon with Co-ion implantation exhibits obviously many Co clusters after a high-vacuum annealing. The result suggests that Co ions may have a longer diffusion length in amorphous carbon than that in ZnO.

The Co concentration of the as-implanted $\text{Zn}_{1-x}\text{Co}_x\text{O}$ nanowires was checked by using EDX. The atomic ratio between Co and Zn was used to determine the Co concentration of this particular nanowire being 10.9%. The average Co concentrations of our as-implanted nanowires are 4, 8 and 11% for the Co ion doses of $2, 4$ and 6×10^{16} per cm^2 , respectively. Noticeably, our EDX analysis indicates that the average value of Co concentration does not show apparent variations on nanowire diameters, once the same dose was used for implantation. In addition, we have carried out EELS mapping studies, shown in Fig. 4.6, to further confirm a homogeneous distribution of Co element in our $\text{Zn}_{0.92}\text{Co}_{0.08}\text{O}$ nanowires after annealing in a high vacuum. Fig. 4.6 also shows images of the O K and Zn L edges to corroborate the compositional mapping of EELS. The image of Co L edge sustains that no Co clusters exist in our $\text{Zn}_{0.92}\text{Co}_{0.08}\text{O}$ nanowires. Therefore, we can safely conclude that our $\text{Zn}_{0.92}\text{Co}_{0.08}\text{O}$ nanowires might be intrinsic DMS materials.

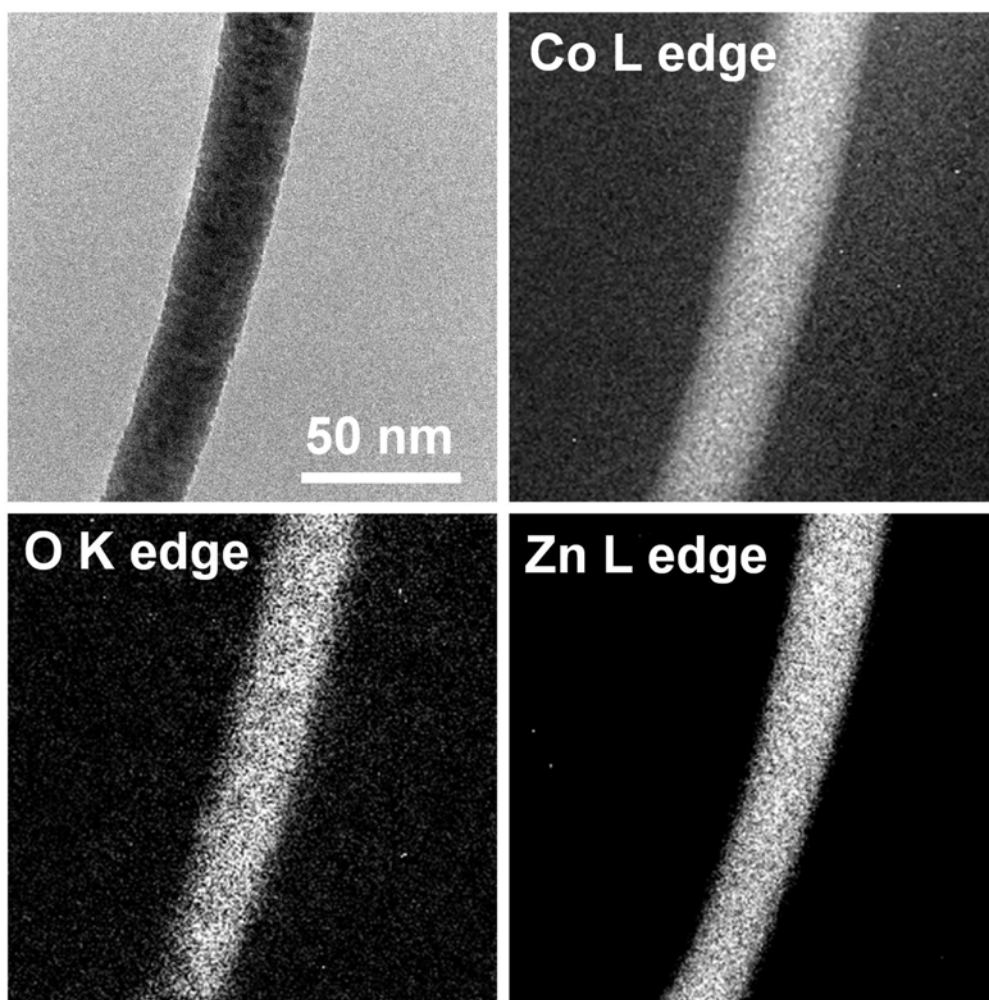


Figure 4.6: Bright-field image with compositional EELS mapping of the Co L, O K, and Zn L edges of the high-vacuum annealed $\text{Zn}_{0.92}\text{Co}_{0.08}\text{O}$ nanowires with an average diameter of 38 nm.

4.4.2 Annealing effects on magnetic properties

In a magnetic field of 500 Oe, temperature dependent magnetizations of various average diameters of $\text{Zn}_{0.92}\text{Co}_{0.08}\text{O}$ NWs are shown in Fig. 4.7(a). The magnetization per Co ion of as-implanted $\text{Zn}_{0.92}\text{Co}_{0.08}\text{O}$ NWs depends strongly on the NW diameter. Thicker NWs exhibit higher magnetization. In addition, magnetizations under field cooled (FC) and zero-field cooled (ZFC) procedures show a division into two separate curves with decreasing temperature. In a similar way, the transition temperature, at which the FC and ZFC magnetization curves bifurcate, is higher for the thicker NWs. The difference in FC and ZFC magnetization suggests an existence of small magnetic single-domains in $\text{Zn}_{0.92}\text{Co}_{0.08}\text{O}$ NWs. In addition, the high transition temperature implies larger magnetic single-domains existing in thicker NWs. Fig. 4.7(a) displays a non-vanishing and non-decreasing magnetization up to a room temperature, signifying a ferromagnetic ordering as well as RTFM. After annealing in a high vacuum, the temperature behavior of $\text{Zn}_{0.92}\text{Co}_{0.08}\text{O}$ NWs with an average diameter of 38 nm is displayed in Fig. 4.7(b), including reproduced data of as-implanted NWs for comparison. The temperature behavior demonstrates a much higher magnetization (a strong ferromagnetic state) and a coincidence and overlapping of FC and ZFC magnetization. This result indicates a growth and development of large magnetic domains, formed by nonaggregated Co ions in high-vacuum annealed $\text{Zn}_{0.92}\text{Co}_{0.08}\text{O}$ NWs.

This phenomena implies that a high-vacuum annealing produces oxygen vacancies (zinc interstitials), which could result in a ferromagnetic coupling between the Co ions, to enhance a ferromagnetic interaction between Co ions and to intensify a magnetic state. Since the as-implanted $\text{Zn}_{0.92}\text{Co}_{0.08}\text{O}$ NWs consist of the same concentration of oxygen vacancies (zinc interstitials), the size of magnetic domains of

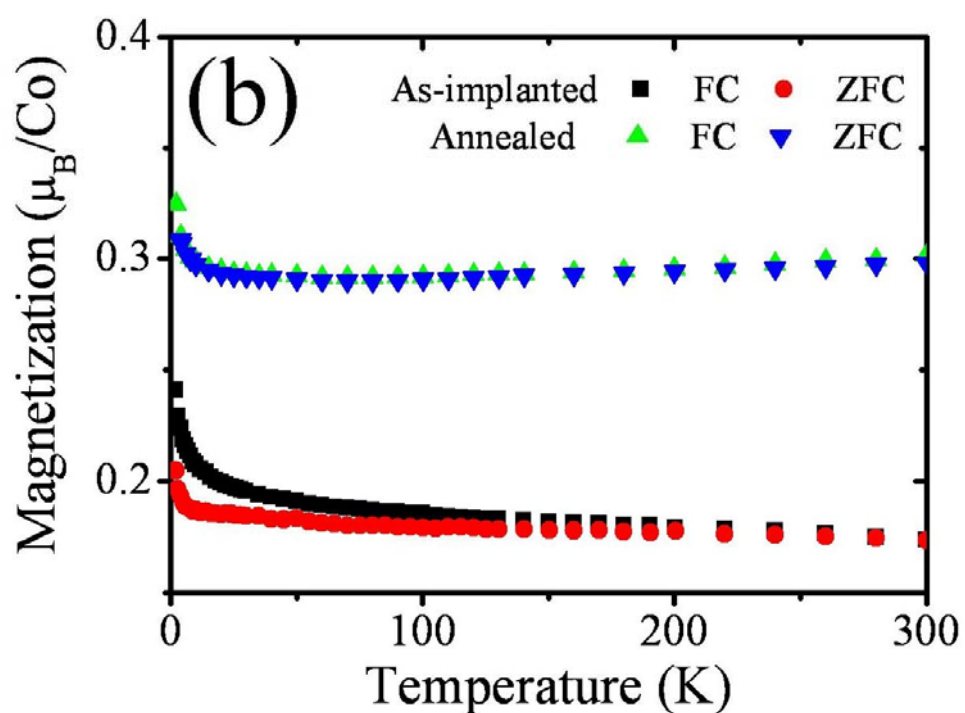
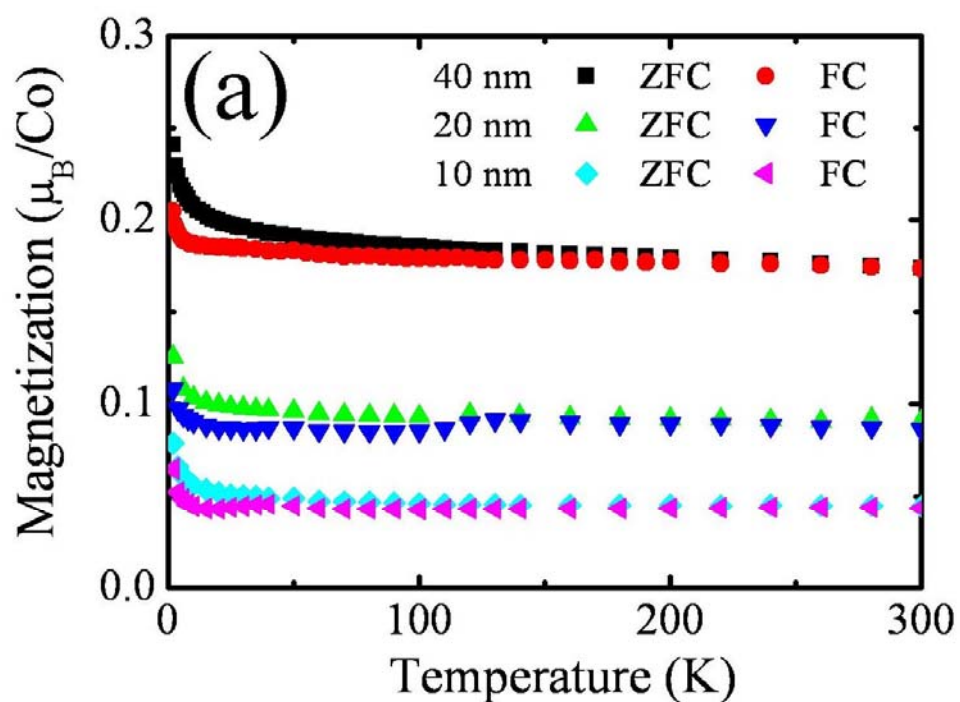


Figure 4.7: (a) FC and ZFC behaviors of temperature dependent magnetization of as-implanted $\text{Zn}_{0.92}\text{Co}_{0.08}\text{O}$ NWs with average diameters of 10, 20, and 40 nm. (b) FC and ZFC magnetizations of as-implanted and high-vacuum annealed $\text{Zn}_{0.92}\text{Co}_{0.08}\text{O}$ NWs with an average diameter of 40 nm. The annealing time is 12 h.

non-aggregated Co ions may be larger in thicker NWs. On the other hand, the size dependent magnetization could be owing to the generation of planar defects, stacking faults and streaking, during the ion bombardment process [38]. Moreover, planar defects could hinder an oxygen-vacancy mediated ferromagnetic ordering so as to abate magnetization and coercivity of thinner, as-implanted $Zn_{1-x}Co_xO$ NWs.

In addition to a temperature dependent behavior, data of field dependent magnetizations as well as hysteresis loops were taken at several different temperatures. Fig. 4.8 exhibits hysteresis loops of as-implanted $Zn_{1-x}Co_xO$ NWs. With an equal Co-concentration of 8%, Fig. 4.8(a) shows that thick NWs reveal a high magnetization and a larger hysteresis loop. Fig. 4.8(b) presents a similar manner of a size dependence to convince us of this general phenomena observed in as-implanted $Zn_{1-x}Co_xO$ NWs. The consequence of a high magnetization in thick NWs agrees with the temperature dependent magnetization delineated in Fig. 4.7(a).

We have argued that the implantation of a high beam current of 600 nA/cm^2 could somewhat introduce a high-vacuum annealing and create oxygen vacancies (zinc interstitials) in ZnO NWs so as to turn on an exchange interaction between non-aggregated Co ions. The Co ions occupying in a certain volume of a ZnO form a magnetic domain. If the ZnO is cut into smaller pieces such as NWs, the magnetic domain and magnetization (moment) will be abated and reduced. This splitting and diminishing of magnetic domains lead to the size effect observed in as-implanted $Zn_{1-x}Co_xO$ NWs. Moreover, the small hysteresis loop indicating a low coercive field (force) in thin $Zn_{1-x}Co_xO$ NWs may be due to a weak interaction between size-reduced magnetic domains or to planar defects (stacking faults and streaking) induced a reduction of ferromagnetic interactions.

We have observed an increase in magnetization from temperature dependent studies after a high-vacuum annealing, as shown in Fig. 4.7(b). To learn the annealing

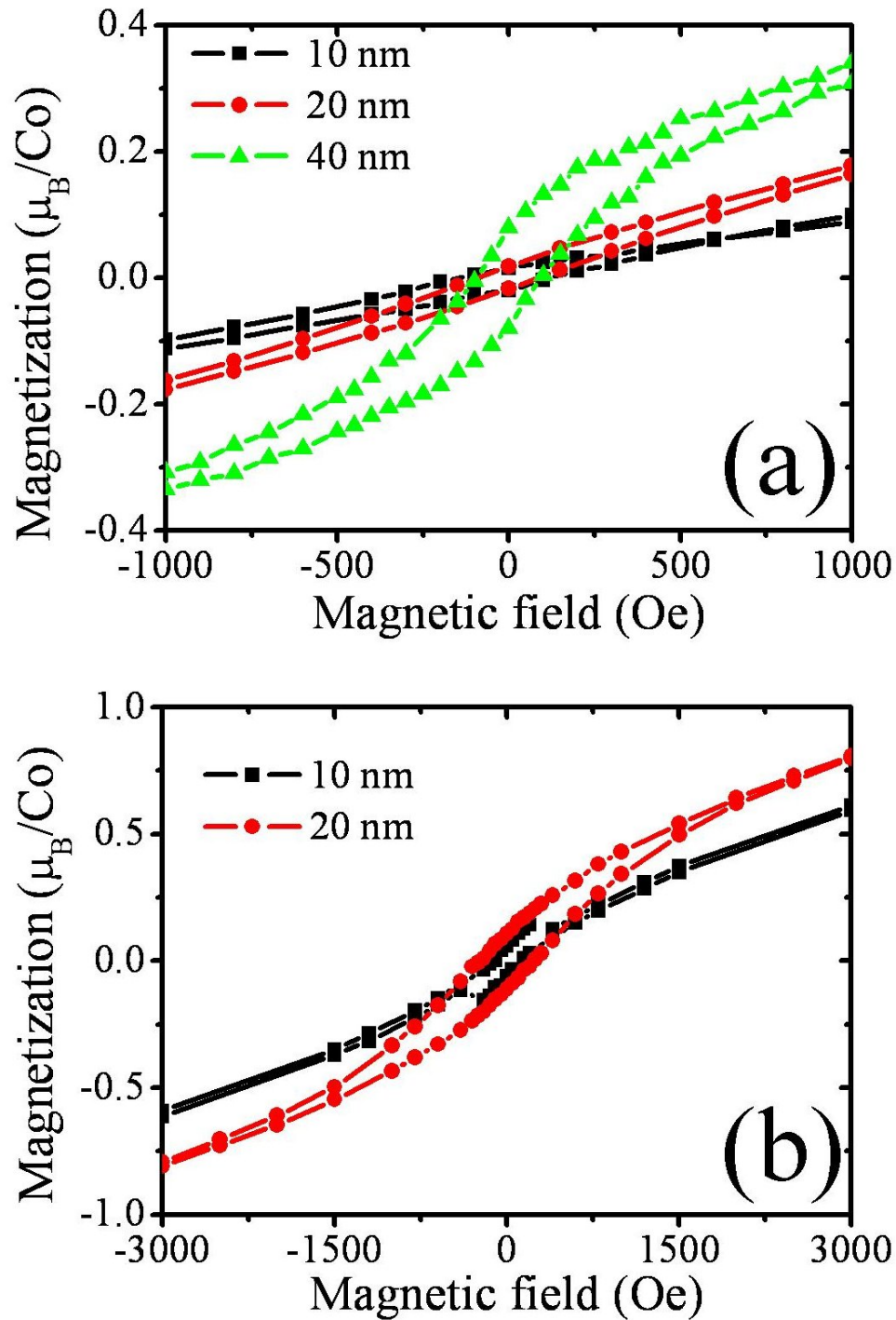


Figure 4.8: (a) Hysteresis loops of as-implanted $\text{Zn}_{0.92}\text{Co}_{0.08}\text{O}$ NWs with three different average diameters marked on graph. The data were taken at 5 K. (b) Hysteresis loops of as-implanted $\text{Zn}_{0.96}\text{Co}_{0.04}\text{O}$ NWs with two different average diameters marked on graph. The data were taken at 2 K.

effect, multiple steps of high-vacuum annealing for hours are employed and the field dependent magnetizations are investigated after each step of annealing. Fig. 4.9(a) demonstrates a change in hysteresis loops of $\text{Zn}_{0.92}\text{Co}_{0.08}\text{O}$ NWs with average diameters of 38 after each step of a high-vacuum annealing. The magnetization as well as the loop becomes higher and larger after several steps of high-vacuum annealing. In addition to the dependence of annealing time, different surface ratios of thin and thick NWs may give rise to dissimilar responses to annealing time. Fig. 4.9(b) reveals a larger increase and expansion in magnetization and field-dependent loops for thinner (19-nm average diameter) NWs. A decrease of annealing time and steps for thinner $\text{Zn}_{1-x}\text{Co}_x\text{O}$ NWs is due to a large surface-to-volume ratio for oxygen diffusion and a large increase in magnetization could be related to the above-mentioned reduction of magnetization in thinner NWs.

The results of multiple-step annealing imply a diffusion of composing elements in the $\text{Zn}_{1-x}\text{Co}_x\text{O}$ material. It has been confirmed from EDX, EELS mapping, and high-resolution TEM inspections that the annealing will not induce detectable diffusion and clustering of Co ions in the DMS NWs. We argued, therefore, that the annealing effect produces oxygen vacancies (zinc interstitials) to enhance an exchange interaction between Co ions. To confirm the creation of oxygen vacancies during the high-vacuum annealing process, the sample is annealed in oxygen to exhibit a weak magnetic state of a low magnetization and small a hysteresis loop and they are subsequently annealed in a high vacuum to recover a strong magnetic state in high-vacuum annealed $\text{Zn}_{1-x}\text{Co}_x\text{O}$ NWs. Fig. 4.9(c) shows the results of 100-nm $\text{Zn}_{0.92}\text{Co}_{0.08}\text{O}$ NWs at room temperature.

To learn more about the high-vacuum annealing enhancement of ferromagnetic ordering, temperature dependence of hysteresis loops of the 38-nm average diameter $\text{Zn}_{0.92}\text{Co}_{0.08}\text{O}$ NWs annealed for 6 hours are displayed in Fig. 4.10(a). An appreciable

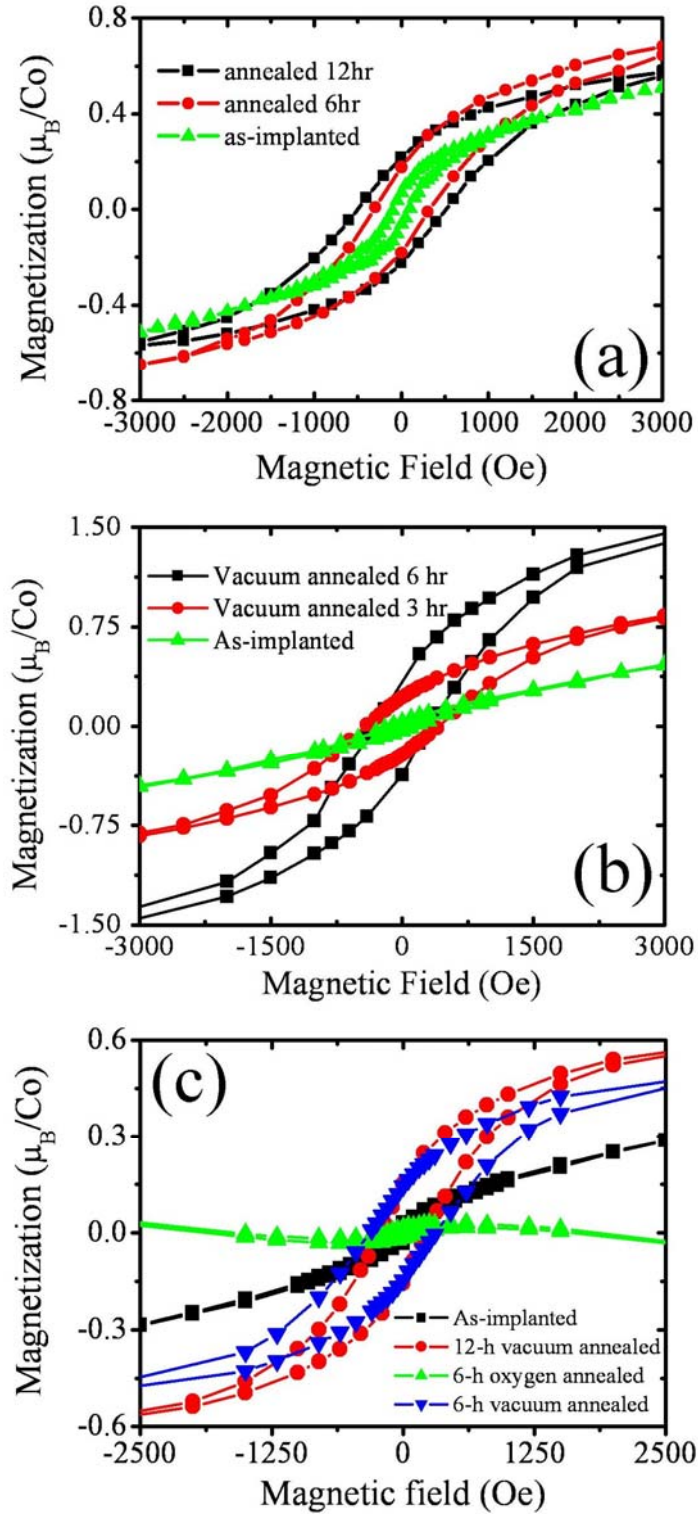


Figure 4.9: (a) Hysteresis loops, taken at 10 K, of as-implanted, 6-h vacuum annealed, and 12-h vacuum annealed $\text{Zn}_{0.92}\text{Co}_{0.08}\text{O}$ NWs with a 38-nm average diameter. (b) Hysteresis loops, taken at 2 K, of as-implanted, 3-h vacuum annealed, and 6-h vacuum annealed $\text{Zn}_{0.92}\text{Co}_{0.08}\text{O}$ NWs with a 19-nm average diameter. (c) Hysteresis loops, taken at 300 K, of as-implanted, 12-h vacuum annealed, 6-h oxygen annealed, and 6-h vacuum annealed $\text{Zn}_{0.92}\text{Co}_{0.08}\text{O}$ NWs with a 100-nm average diameter.

hysteresis loop as observed at 300 K clearly points to stabilized RTFM in these NWs. The field-dependent magnetization reveals only a minor temperature dependence of the saturated magnetization. On the other hand, a large increase in the coercive field with decreasing temperature is evident. The measured coercive field in Fig. 4.10(b) obeys a square-root temperature dependence. Such temperature behavior, which is in line with a superparamagnetic feature, can be described by Eq. (4.1). From the linear fit indicated in Fig. 4.10(b), a blocking temperature of ~ 700 K was deduced. Fig. 4.10(c) shows the temperature dependence of hysteresis loops and coercive fields for 19-nm average diameter $\text{Zn}_{0.92}\text{Co}_{0.08}\text{O}$ NWs. These thinner DMS NWs, which were annealed only for 3 h, already display a prominent hysteresis loop at room temperature. Thus, the stabilized RTFM in the $\text{Zn}_{0.92}\text{Co}_{0.08}\text{O}$ nanowires is again confirmed. It should be noted that the room-temperature hysteresis loop in these 19-nm average diameter NWs is considerably larger than that in the 38-nm ones. This observation points to a strong magnetic state in the former, the thin nanowires. The variation of the coercive field with the square root of temperature is shown in Fig. 4.10(d). The linear behavior suggests that our sample exhibits a characteristic of temperature-dependent coercivity coincident with a superparamagnetic feature. The blocking temperature inferred from the linear fit is ~ 2300 K.

If we assume that the temperature dependent coercivity is originated from Co clusters, we may estimate the cluster diameter according to the equation [136]:

$$T_B = \frac{K\langle V \rangle}{30k_B} \quad (4.6)$$

where T_B is the blocking temperature, $K \approx 5 \times 10^6$ erg/cm³ is the anisotropy energy of Co metal, k_B is the Boltzmann constant, and $\langle V \rangle$ is the average volume of Co clusters. Assume a spherical geometry for Co clusters, average diameters of ~ 9 and ~ 15 nm are derived for $T_B \sim 700$ and 2300 K, respectively. Such large clusters of ~ 9 nm in

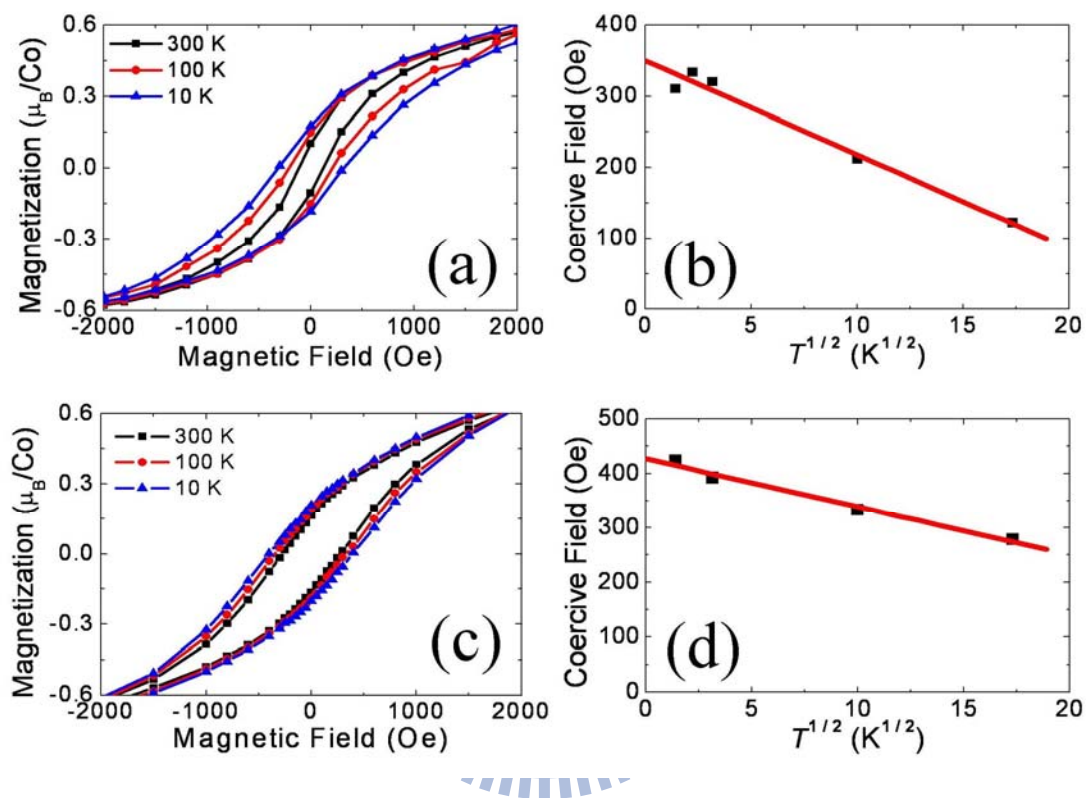


Figure 4.10: (a) Hysteresis loops of $\text{Zn}_{0.92}\text{Co}_{0.08}\text{O}$ NWs with (a) 38-nm and (c) 19-nm average diameter at several temperatures after annealing in a high vacuum for 6 h and 3 h, respectively. (b) and (d) are the coercive field, estimated from Fig. 13(a) and Fig. 13(c) respectively, as a function of square root of temperature.

diameter, if any exist, should be readily detectable. We had implemented HRTEM to carefully inspect our high-vacuum annealed nanowires. However, no microstructure was detected. Moreover, we have performed EDX and EELS mapping studies, which again confirmed a uniform distribution of Co ions in all of our DMS NWs. Therefore, we conclude that the observed square root temperature behavior of coercivity reflects an intrinsic characteristic of our DMS NWs. Moreover, Fig. 4.10(a) demonstrates a temperature independence of magnetization saturation that is consistent with the result shown in Fig. 4.7(b). The ferromagnetic ordering remains up to room temperature so the RTFM in the high-vacuum annealed $Zn_{1-x}Co_xO$ NWs is confirmed.

The temperature and field dependent magnetization of ZnO sheathed in amorphous carbon with Co clusters sample is displayed in Fig. 4.11 for a comparative study. As shown in Fig. 4.11(a), FC and ZFC magnetizations are separated into two parts with a decrease of temperature. The undeniable bifurcation of temperature dependent magnetization in FC and ZFC procedures stands for a superparamagnetic feature of Co clusters [135]. This feature will be evident if the Co clusters are mono-dispersed and uniform in size. As we have shown in Fig. 4.5(d), the Co clusters have a wide distribution and a standard deviation of ~ 6.0 nm in diameter that causes a relatively small deviation in FC and ZFC magnetization at low temperatures in comparison with ideal ferromagnetic colloids. Fig. 4.11(b) shows shrinkage of hysteresis loops as well as a decrease in coercive fields with increasing temperature indicating the superparamagnetism of the Co clusters. The blocking temperature is determined to be ~ 420 K via a least square fitting, shown as a red line in the inset of Fig. 4.11(b). The average diameter of ~ 9 nm can be estimated by using Eq. (4.6) with $T_B = 420$ K. The average diameter of ~ 9 nm agrees very well with that calculated from a statistical distribution of cluster diameters from TEM measurements (9.4 nm in Fig. 4.5(f)). This result sustains the analyses and deductions used in this work. It is

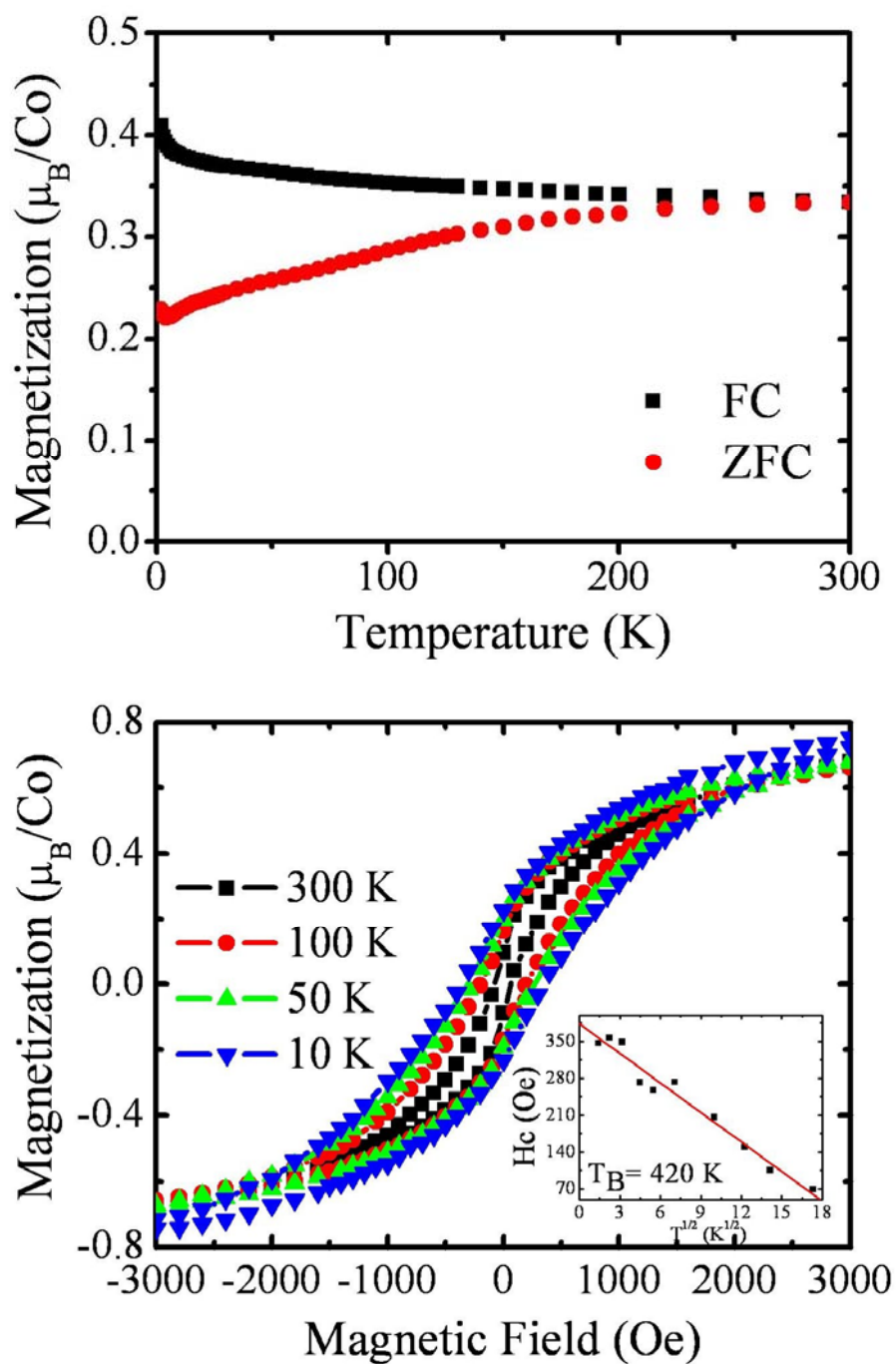


Figure 4.11: (a) FC and ZFC magnetization of ZnO sheathed in amorphous carbon with Co clusters. The Co ion dose and average diameter of ZnO are $4 \times 10^{16} \text{ cm}^{-2}$ and 38 nm, respectively, for this sample. (b) Hysteresis loops of ZnO sheathed in amorphous carbon with Co clusters. The inset shows the coercive field as a function of square root of temperature.

noted that all of the three characteristics of superparamagnetic Co clusters as well as ferromagnetic colloids have been observed. These features are a bifurcation of FC and ZFC magnetization, a temperature dependent coercive field, and the same average diameter evaluated from both TEM measurements and T_B estimations.

4.4.3 Characterization of magnetic domains by MFM

In contrast to SQUID magnetometry that measures the total magnetization resulted from every NWs on a quartz substrate, magnetic force microscopy (MFM) enables us to observe the ferromagnetic state of an individual NW. In a phase image of MFM measurements, the bright and dark contrasts represent the domain magnetized in the direction parallel and antiparallel, which means the interactions between sample and tip are attractive and repulsive, to the magnetic tip. Generally, the bright and dark contrast accompany with one another in a phase image. However, we sometimes observed a whole NW with only dark contrast, as shown in Fig. 4.12(b) with simultaneous topography image shown in Fig. 4.12(a). We sort out this kind of NW to be the non-ferromagnetic. The dark contrast comes from the abrupt protruding of the NW that affects the tip vibrating by van der Waals force instead of magnetic force. To confirm our conjecture, we carried out the MFM measurement on the pure ZnO NWs (without Co implantation), and obtained the same results. Except for the non-ferromagnetic NWs, the ferromagnetic NWs with bright and dark contrast can be grouped into two kinds: longitudinally and transversely magnetized, according to the distribution of contrasts. Fig. 4.12(c) - (f) show MFM images of these two kinds of ferromagnetic NWs with their simultaneously topographic images. Thus, the bright

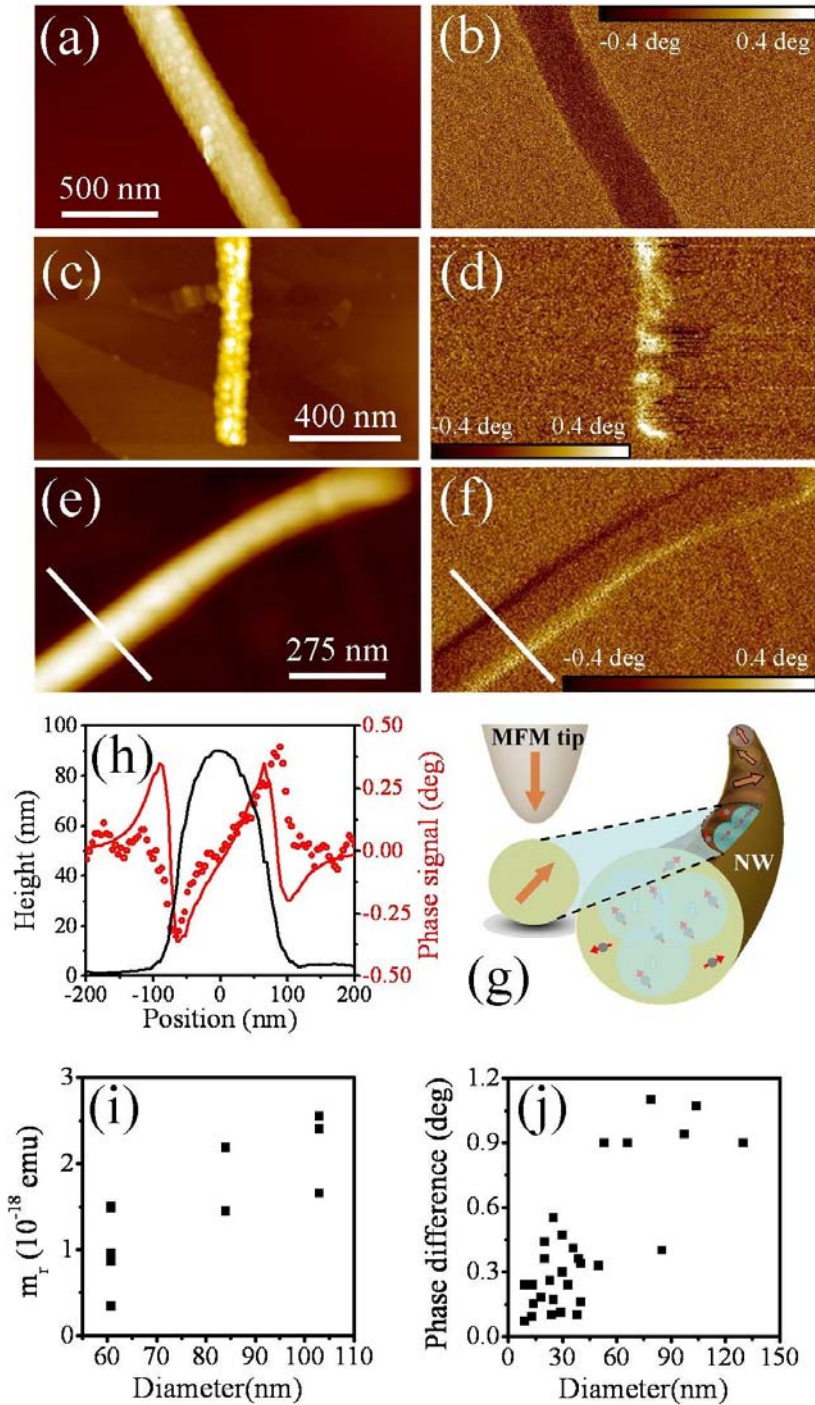


Figure 4.12: MFM images of (b) non-ferromagnetic, (d) longitudinally magnetized, and (f) transversely magnetized NWs with their simultaneous AFM images (a), (c), and (e). (h) Topographic (black line) and phase signal (red dot) profiles of (e) and (f) with fitting curve (red line). (g) Schematic for modeling the origin of the ferromagnetism in $Zn_{1-x}Co_xO$ NWs and their relative orientation of magnetization between a transverse single-domain and a MFM tip. (i) Calculated magnetic dipole moment of NWs as a function of their size. (j) Phase difference of MFM data as a function of NW diameter.

and dark areas that transversely distributed on the NW in Fig. 4.12(c) indicate that this NW was longitudinal magnetized which means the easy axis of magnetic domain are in the same direction of NW axis. On the other hand, we have also observed some NWs with bright and dark contrasts distributed along the NW edges which represented the transverse magnetization of the NWs, as shown in Fig. 4.12(f). In Fig. 4.12(h), the black line and red dot depicted the topographic and phase profile along the white line in Fig. 4.12(e) and (f). To further confirm the transverse magnetization, we adopted a model that approximates the magnetic tip and sample as two magnetic dipole moments, and the relative angle between two dipole moments determines the MFM image [141]. The red line in Fig. 4.12(h) shows our data was well fitted with this model and the relative angle was obtained to be 99° . The illustration in Fig. 4.12(g) shows the configuration of our $Zn_{1-x}Co_xO$ NWs. According to BMP model, implanted Co ions coupled with each other via shallow donor, which was resulted from oxygen deficiencies, and formed ferromagnetic domains. From the emergence of superparamagnetism in SQUID data, we can infer there are many single domains in the vacuum-annealed $Zn_{1-x}Co_xO$ NWs. These single domains which can be approximated as giant magnetic dipoles are magnetized independently therefore we can observe many bright-dark regions in MFM images. Provided the magnetic dipole moment of our commercial MFM tips is $\sim 10^{-13}$ emu, we can estimate the magnetic dipole moment of the NWs is 10^{-18} to 10^{-19} from the aforementioned fitting results. We have calculated the magnetic dipole moment of various sizes of our NWs and the results are shown in Fig. 4.12(i). The increasing magnetic dipole moment of the NWs with their size is in accord with our SQUID data. To further confirm this point, we measure the phase difference between bright and dark contrasts on individual NWs as a function of their size, since the phase difference qualitatively reflects the magnetization strength. In Fig. 4.12(j), the roughly linear dependence of the phase

difference, which is defined as difference between the average phase signal of bright and dark regions, on the NW diameter was observed in our NWs.

The transverse magnetization in NWs indicates the easy axes of domains are perpendicular to the axes of NWs. Once the NWs with transverse magnetization were magnetized by the permanent magnet, the domains were initiated in the same direction and we can take the MFM images like figure Fig. 4.12(f). Intriguingly, as we successively scanned this kind of NWs, however, some portion of the bright-dark contrasts in the NWs was reversed randomly. In Fig. 4.13(a), a NW was initially magnetized exhibiting bright at left side and dark at right side. After repeated scanning, from Fig. 4.13(b) to (d), the bright-dark regions were reversed randomly. The contrast reversal can also be observed in the results of using magnetic tips with single domain apex and attributed to the reversal of the apex domain [142]. The stray field induced by the NW at the position of MFM tip can be calculated by the relation $\vec{H} = 3(\vec{\mu} \cdot \vec{r})\vec{r} / r^5 - \vec{\mu} / r^3$, where \vec{H} is the stray field, $\vec{\mu}$ is the dipole moment of the NW which is in the order of 10^{-18} to 10^{-19} emu, and \vec{r} is the position vector from tip to NW. As the tip was located at the top of NW with a lift distance of 200 nm, the stray field induced by the NW at the tip is 10^{-2} to 10^{-3} Oe which is far less than the coercive field of out MFM tip, 300 Oe. With this result, we infer that magnetization reversal of the NWs was caused by the stray field of the magnetic tip. On the other hand, we can not observe the random magnetization reversal in the longitudinally magnetized NWs. The bright-dark contrast of this kind of NWs changed only when we applied a strong field by a permanent magnet. Fig. 4.13(e) and (f) show the MFM images of a longitudinally magnetized NWs before and after applying a field by a magnet and the white arrows indicate the place where the bright-dark contrasts change.

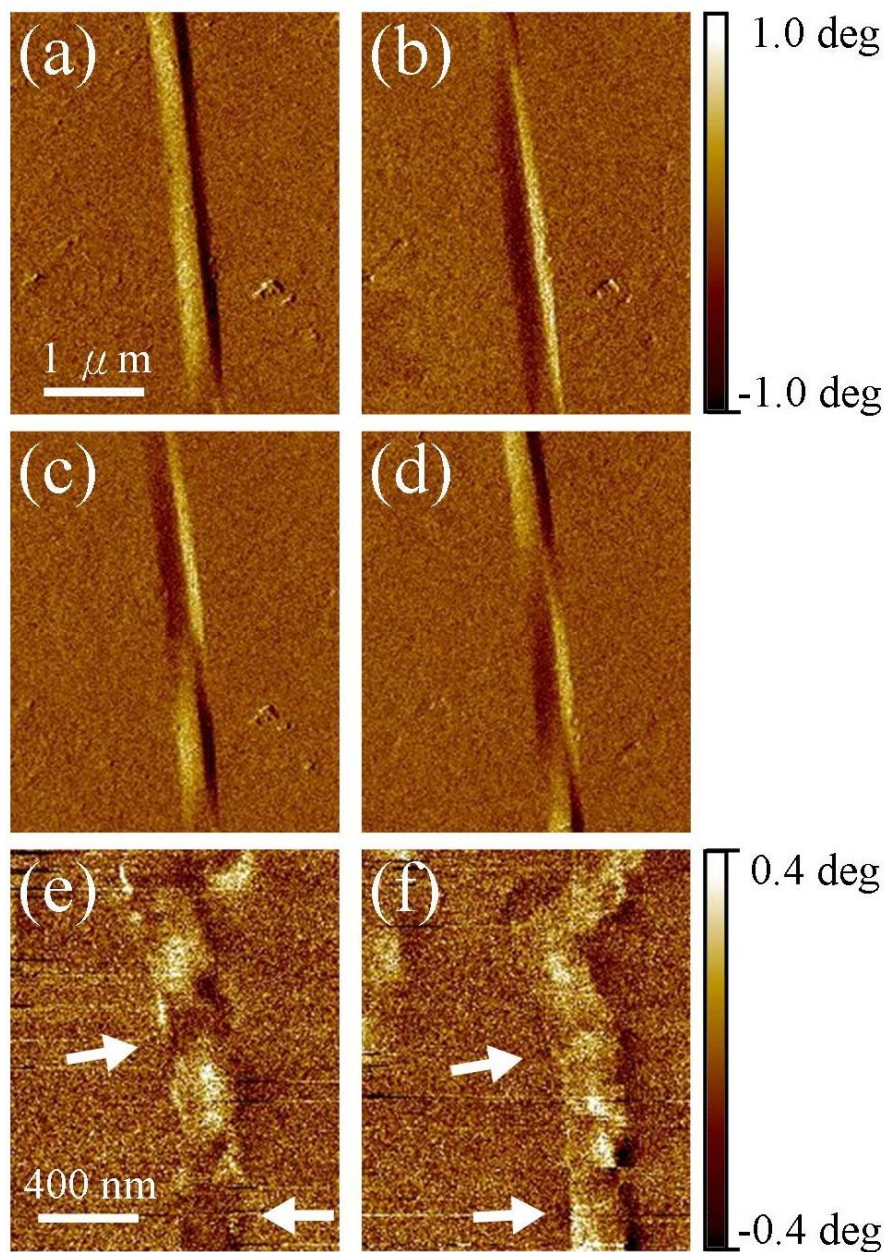


Figure 4.13: Successive magnetization reversal of a 50 nm diameter $\text{Zn}_{0.89}\text{Co}_{0.11}\text{O}$ NWs resulted from continuous scanning by a magnetic tip, in order of (a), (b), (c), and (d). MFM images of longitudinally magnetized NWs (e) before and (f) after applying a field by a magnet and the white arrows indicate the place where the bright-dark contrasts change.

To understand the dependence of magnetization of our RTFM NWs on the temperature, the samples were in situ heated up in high vacuum and then cooled down to obtain the remanent magnetization of the NWs. Fig. 4.14(a) to (b) show the MFM and its simultaneous topography image of a NW before heating. The MFM images of the same NW after heating up to 373 K and 673 K are shown in Fig. 4.14(c) and (d). The bright-dark contrast became weak as the heating temperature was increased. This result demonstrates the remanent magnetization of the ferromagnetic NWs was diminished by the thermal energy. Fig. 4.14(e) shows the phase difference as a function of temperature from room temperature to 673 K. For a single domain particle, the remanent magnetization is $M_r = M_i e^{-t/\tau}$ [137], where M_i is the initial state, $\frac{1}{\tau} = f_0 e^{-KV/k_B T}$, and f_0 is called frequency factor with a value of about 10^9 sec^{-1} . Thus the M_r should exponentially decay with temperature as in Fig. 4.14(e). From room temperature to 523 K, we have taken the MFM images of several NWs for each raised temperature and calculated their phase difference. The result is shown in Fig. 4.14(f), in which black squares represent the data from transverse magnetized NWs and red circles represent the data from an individual longitudinal NW. At low temperature, the fluctuation of phase difference of transverse magnetized NWs is considerable probably resulted from the large variation of NW diameter ranging from 20 to 120 nm, since the phase difference is proportional to the diameter. The phase difference decrease with a shrinking fluctuation as the heating temperature is raised and almost vanishes at about 600 K. We have also measured the temperature dependence of phase difference on an individual longitudinal magnetized NW and observed that phase difference did not change with the heating temperature, as shown in Fig. 4.14(f). The result indicates the longitudinal NWs has a strong coercivity and implies a high Cuire or blocking temperature.

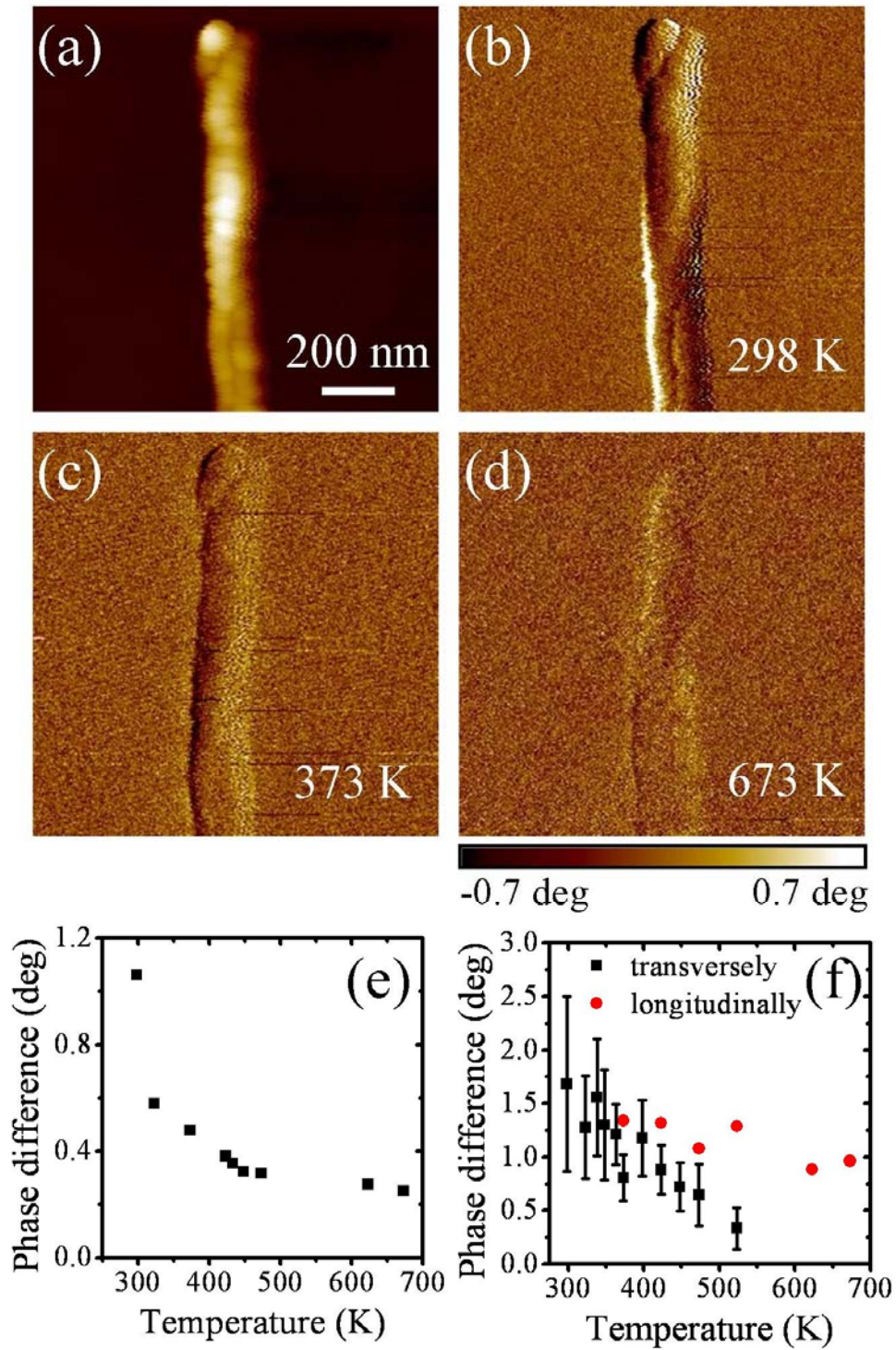


Figure 4.14: MFM images of Zn_{0.89}Co_{0.11}O a NW (b) before and after heating up to (c) 373 K and (d) 673 K. (e) Phase difference of MFM data of an individual Zn_{0.89}Co_{0.11}O NW as a function of heating temperature. (f) Phase difference of MFM data of different transversely magnetized NWs represented as black squares and a longitudinally magnetized NW represented as red circles.

Chapter 5

Conclusion

In this thesis, we have studied physical phenomena in low dimensional nanostructures, including self-assembly and collective charge transport in zero-dimensional quantum dots (QDs) and ferromagnetism in one-dimensional nanowires (NWs).

In the topic of self-assembly behaviors of QDs, we prepared various kinds of 2D growth patterns by dropping toluene-dissolved PbSe QD suspension on a hot graphite substrate. These growth patterns have been extensively analyzed, and related phase diagram, pair bond energy, and growth mechanisms have accordingly been studied. The pair bond energy, $\varepsilon = 59$ meV, between PbSe QDs is derived from a simple analysis of substrate temperature and coverage dependences of island density. This determines the states of growth patterns on 2D Lennard-Jones phase diagram. Another analysis on occurrences of small clusters in thermal equilibrium gives a pair bond energy of ~ 32 meV during cluster formation. Moreover, with a low coverage, a scaled function of island size distribution was used to determine the critical nucleus size of either 0 or 1 for this system. A decrease of the wavelength in spinodal patterns was summarized due to both the undercooling temperature below the critical-point temperature and the restricted evolution time for pattern formation. Through a comparison of patterns at different temperatures, the diffusion-limited aggregation

reveals cluster and single-particle diffusions at temperatures of near and above, respectively, the solvent boiling point. The interplay between spinoal decomposition and diffusion-limited aggregation is under control by using substrate temperature so as to make 2D PbSe QD islands on a flat graphite surface.

After knowing the mechanism of self-assembly of 2D QD arrays, we prepared these arrays with various sizes on flat gold surfaces and used the low-temperature STM to measure their tunneling spectra at both room temperature and 78 K. By estimating the separation distance between QDs, the inter-dot capacitance between the PbSe QDs is two orders of magnitude larger than both the tip-to-array and array-to-substrate capacitances, leading to a strong inter-dot coupling and a long screening length. The characteristic I - V of the QD array is fitted with the scaling power law $I \propto (V - V_{\text{th}})^{\zeta}$ of the Middleton–Wingreen model to extract threshold voltages V_{th} and the scaling exponents ζ . A drop in V_{th} , which presents Coulomb blocking voltage, and a rise in ζ , which presents conduction channels, were found to be consistent with the theoretical model when the QD number increases from 1 to 80. Meanwhile, a saturation tendency for arrays with QD numbers greater than 100 has been perceived both in V_{th} and ζ for data acquired at 78 K. An enhancement in the collective behavior of interdot couplings through the addition of PbSe QDs has been explored.

Subsequently, we extend our samples from zero-dimensional to one-dimensional DMS NW. Various average diameters, which can be well regulated by using gold nanoparticles as catalysts, of single-crystalline cylindrical ZnO NWs with a [0001] growth direction are synthesized by using the vapor transport method. The as-grown ZnO NWs are implanted with different doses of Co ions to form $\text{Zn}_{1-x}\text{Co}_x\text{O}$ NWs. The as-implanted $\text{Zn}_{1-x}\text{Co}_x\text{O}$ NWs possess a high density of bombardment-induced structure defects and exhibit either a paramagnetic or a weak ferromagnetic state.

Thinner as-implanted $Zn_{1-x}Co_xO$ NWs exhibit a larger hysteresis loop and a higher magnetization. This NW-diameter dependence indicates that a bulk magnet with a large magnetic domain is divided into many pieces of NWs with lots of small-size domains. Annealing in a high vacuum reduces structural, planar defects of stacking faults and streaking, and creates point defects of oxygen vacancies (zinc interstitials) in $Zn_{1-x}Co_xO$ NWs to induce a strong ferromagnetic state. By using EDX mapping, it is observed that Co ions are randomly distributed without any aggregations in both as-implanted and annealed $Zn_{1-x}Co_xO$ NWs. The annealing effect further supports the idea of oxygen vacancies induced ferromagnetic interactions between Co ions. After high-vacuum annealing, more oxygen vacancies are generated and the magnetic domains grow up. The superparamagnetic features gradually disappear in the high-vacuum annealed $Zn_{1-x}Co_xO$ NWs. The ferromagnetic properties are observed at room temperature to assure the RTFM in the high-vacuum annealed $Zn_{1-x}Co_xO$ NWs, and to confirm the T_C above room temperature. In particular, ZnO NWs sheathed in amorphous carbon with Co clusters have been produced for comparison and corroborating our measurements and analyses of DMS $Zn_{1-x}Co_xO$ NWs.

In addition, the domain structure of individual DMS NWs was inspected by employing MFM. Longitudinally magnetized and transversely magnetized NWs were observed. The magnetic moment, which is calculated by an approximation model, as well as the phase difference of transversely magnetized NWs increases with the NW size. The domains of transversely magnetized NWs are easily influenced indicating the weak coercivity of this kind of NWs. The phase difference, representing remanent magnetization, of transversely magnetized NWs decrease exponentially with the temperature. This result is in accord with our conjecture that the implanted Co ions are coupled as bound magnetic polaron to form a single domain system in NWs, which exhibit the superparamagnetic behaviors.

Reference

- [1] M. A. Kastner, *Physics today* **46(1)**, 24 (1993).
- [2] C. T. Black, C. B. Murray, R. L. Sandstrom, and S. Sun, *Science* **290**, 1131 (2000).
- [3] D. V. Talapin and C. B. Murray, *Science* **310**, 86 (2005).
- [4] M. D. Fischbein and M. Drndic, *Appl. Phys. Lett.* **86**, 193106 (2005).
- [5] G. Konstantatos, I. Howard, A. Fischer, S. Hoogland, J. Clifford, E. Klem, L. Levina and E. H. Sargent, *Nature* **442**, 180 (2006).
- [6] B. A. Korgel and D. Fitzmaurice, *Phys. Rev. Lett.* **80**, 3531 (1998).
- [7] T. P. Bigioni, X. M. Lin, T. T. Nguyen, E. I. Corwin, T. A. Witten and H. M. Jaeger, *Nat. Mater.* **5**, **265** (2006).
- [8] M. Maillard, L. Motte, A. T. Ngo, and M. P. Pileni, *J. Phys. Chem. B* **104**, 11871 (2000).
- [9] N. D. Denkov, O. D. Velev, P. A. Kralchevsky, I. B. Ivanov, H. Yoshimura, and K. Nagayama, *Nature* **361**, 26 (1993).
- [10] B. G. Prevo and O. D. Velev, *Langmuir* **20**, 2099 (2004).
- [11] M. P. Pileni, *J. Phys. Chem. B* **105**, 3358 (2001).
- [12] J. A. Nenables, G. D. T. Spiller, and M. Hanbücken, *Rep. Prog. Phys.* **47**, 399 (1984).
- [13] G. Ge and L. Brus, *J. Phys. Chem. B* **104**, 9573 (2000).
- [14] J. Tang, G. Ge and L. Brus, *J. Phys. Chem. B* **106**, 5653 (2002).
- [15] C. B. Murray, S. Sun, W. Gaschler, H. Doyle, T. A. Betley, and C. R. Kagan, *IBM J. Res. Dev.* **45**, 47 (2001).

- [16] L. E. Brus, *J. Chem. Phys.* **80**, 4403 (1984).
- [17] U. Banin, Y. Cao, D. Katz, and O. Millo, *Nature* **400**, 542 (1999).
- [18] B. Alpers, I. Rubinstein, and G. Hodes, *Appl. Phys. Lett.* **75**, 1751 (1999).
- [19] E. P. A. M. Bakkers and D. Vanmaekelbergh, *Phys. Rev. B* **62**, R7743 (2000).
- [20] P. Liljeroth, P. A. Z. van Emmichoven, S. G. Hickey, H. Weller, B. Grandidier, G. Allan, and D. Vanmaekelbergh, *Phys. Rev. Lett.* **95**, 086801 (2005).
- [21] C. P. Collier, R. J. Saykally, J. J. Shiang, S. E. Henrichs, and J. R. Heath, *Science* **277**, 1978 (1997).
- [22] S. H. Kim, and G. M. Ribeiro, D. A. A. Ohlberg, R. S. Williams, and J. R. Heath, *J. Phys. Chem. B* **103**, 10341 (1999).
- [23] P. Liljeroth, K. Overgaag, A. Urbieto, B. Grandidier, S. G. Hickey, and D. Vanmaekelbergh, *Phys. Rev. Lett.* **97**, 096803 (2006).
- [24] D. Steiner, A. Aharoni, U. Banin, and O. Millo, *Nano Lett.* **6**, 2201 (2006).
- [25] S. H. Kim, G. Medeiros-Ribeiro, D. A. A. Ohlberg, R. S. Williams, and J. R. Heath, *J. Phys. Chem. B* **103**, 10341 (1999).
- [26] T. S. Mentzel, V. J. Porter, S. Geyer, K. MacLean, M. G. Bawendi, and M. A. Kastner, *Phys. Rev. B* **77**, 075316 (2008).
- [27] C. I. Durüoz, R. M. Clarke, C. M. Marcus, and J. S. Harris Jr., *Phys. Rev. Lett.* **74**, 3237 (1995).
- [28] A. J. Rumberg, T. R. Ho, and J. Clarke, *Phys. Rev. Lett.* **74**, 4714 (1995).
- [29] A. A. Middleton and N. S. Wingreen, *Phys. Rev. Lett.* **71**, 3198 (1993).
- [30] A. Bezryadin, R. M. Westervelt, and M. Tinkham, *Appl. Phys. Lett.* **74**, 2699 (1999).
- [31] K. Elteto, X. M. Lin and H. M. Jaeger, *Phys. Rev. B* **71**, 205412 (2005).
- [32] R. Parthasarathy, X. M. Lin and H. M. Jaeger, *Phys. Rev. Lett.* **87**, 186807 (2001).

- [33] H. Fan, K. Yang, D. M. Boye, T. Sigmon, K. J. Malloy, H. Xu, G. P. L'opez, and C. J. Brinker, *Science* **304**, 567 (2004).
- [34] M. O. Blunt, M. Šuvakov, F. Pulizzi, C. P. Martin, E. Pauliac-Vaujour, A. Stannard, A. W. Rushforth, B. Tadić, and P. Moriarty, *Nano Lett.* **7**, 855 (2007).
- [35] S. J. Pearton, C. R. Abernathy, D. P. Norton, A. F. Hebard, Y. D. Park, L. A. Boatner, and J. D. Budai, *Mater. Sci. Eng. R* **40**, 137 (2003).
- [36] S. A. Wolf, D. D. Awschalom, R. A. Buhrman, J. M. Daughton, S. von Molnár, M. L. Roukes, A. Y. Chtchelkanova, and D. M. Treger, *Science* **294**, 1488 (2001).
- [37] T. Dietl, H. Ohno, F. Matsukura, J. Cibert, and D. Ferrand, *Science* **287**, 1019 (2000).
- [38] K. Sato, and H. Katayama-Yoshida, *Jpn. J. Appl. Phys.* **40**, L334 (2001).
- [39] K. Ueda, H. Tabata, and T. Kawai, *Appl. Phys. Lett.* **79**, 988 (2001).
- [40] S. J. Han, J. W. Song, C. H. Yang, S. H. Park, J. H. Park, Y. H. Jeong, and K. W. Rhie, *Appl. Phys. Lett.* **81**, 4212 (2002).
- [41] M. Venkatesan, C. B. Fitzgerald, J. G. Lunney, and J. M. D. Coey, *Phys. Rev. Lett.* **93**, 177206 (2004).
- [42] H. J. Lee, S. Y. Jeong, C. R. Cho, and C. H. Park, *Appl. Phys. Lett.* **81**, 4020 (2002).
- [43] D. A. Schwartz, and D. R. Gamelin, *Adv. Mater.* **16**, 2115 (2004).
- [44] Z. Jin, T. Fukumura, M. Kawasaki, K. Ando, H. Saito, T. Sekiguchi, Y. Z. Yoo, M. Murakami, Y. Matsumoto, T. Hasegawa, and H. Koinuma, *Appl. Phys. Lett.* **78**, 3824 (2001).
- [45] M. Bouloudenine, N. Viart, S. Colis, J. Kortus, and A. Dinia, *Appl. Phys. Lett.* **87**, 052501 (2005).
- [46] P. Sati, C. Deparis, C. Morhain, S. Schäfer, and A. Stepanov, *Phys. Rev. Lett.* **98**,

137204 (2007).

- [47] J. H. Park, M. G. Kim, H. M. Jang, S. Ryu, and Y. M. Kim, *Appl. Phys. Lett.* **84**, 1338 (2004).
- [48] B. Martínez, F. Sandiumenge, L. Balcells, J. Arbiol, F. Sibieude, and C. Monty, *Phys. Rev. B* **72**, 165202 (2005).
- [49] W. B. Jian, Z. Y. Wu, R. T. Huang, F. R. Chen, J. J. Kai, C. Y. Wu, S. J. Chiang, M. D. Lan, and J. J. Lin, *Phys. Rev. B* **73**, 233308 (2006).
- [50] Z. Y. Wu, F. R. Chen, J. J. Kai, W. B. Jian, and J. J. Lin, *Nanotechnology* **17**, 5511 (2006).
- [51] N. Khare, M. J. Kappers, M. Wei, M. G. Blamire, and J. L. MacManus-Driscoll, *Adv. Mater.* **18**, 1449 (2006).
- [52] M. Gacic, G. Jakob, C. Herbort, H. Adrian, T. Tietze, S. Brück, and E. Goering, *Phys. Rev. B* **75**, 205206 (2007).
- [53] H. S. Hsu, J. C. A. Huang, Y. H. Huang, Y. F. Liao, M. Z. Lin, C. H. Lee, J. F. Lee, S. F. Chen, L. Y. Lai, and C. P. Liu, *Appl. Phys. Lett.* **88**, 242507 (2006).
- [54] J. M. D. Coey, M. Venkatesan, and C. B. Fitzgerald, *Nat. Mater.* **4**, 173 (2005).
- [55] W. Hansen, T. W. Smith, K. Y. Lee, J. A. Brum, C. M. Knoedler, J. M. Hong, and D. P. Kern, *Phys. Rev. Lett.* **62**, 2168 (1989).
- [56] S. M. Reimann, and M. Manninen, *Rev. Mod. Phys.* **74**, 1283 (2002).
- [57] A. P. Alivisatos, *Science* **271**, 933 (1996).
- [58] W. B. Jian, W. Lu, J. Fang, S. J. Chiang, M. D. Lan, C. Y. Wu, Z. Y. Wu, F. R. Chen, and J. J. Kai, *J. Chem. Phys.* **124**, 064711 (2006).
- [59] C. B. Murray, C. R. Kagan, M. G. Bawendi, *Science* **270**, 1335 (1995).
- [60] L. Motte, F. Billoudet, and M. P. Pileni, *J. Phys. Chem.* **99**, 16425 (1995).
- [61] Z. L. Wang, *Adv. Mater.* **10**, 13 (1998).
- [62] E. Rabani, D. R. Reichman, P. L. Geissler, and L. E. Brus, *Nature* **426**, 271

(2003).

- [63] X. M. Lin, H. M. Jaeger, C. M. Sorensen, and K. J. Klabunde, *J. Phys. Chem. B* **105**, 3353–3357 (2001).
- [64] J. J. Urban, D. V. Talapin, E. V. Shevchenko, C. R. Kagan, and C. B. Murray, *Nat. Mater.* **6**, 115 (2007).
- [65] M. O. Blunt, C. P. Martin, M. Ahola-Tuomi, E. Pauliac-Vaujour, P. Sharp, P. Nativo, M. Brust, and P. J. Moriarty, *Nat. Nanotechnol.* **2**, 167 (2007).
- [66] W. Cheng, N. Park, M. T. Walter, M. R. Hartman, and D. Luo, *Nat. Nanotechnol.* **3**, 682 (2008).
- [67] J. A. Barker, D. Henderson, and F. F. Abraham, *Physica* **106A**, 226 (1981).
- [68] S. Toxvaerd, *Phys. Rev. Lett.* **44**, 1002 (1980).
- [69] D. Walton, *J. Chem. Phys.* **37**, 2182 (1962).
- [70] M. C. Bartelt, and J. W. Evans, *Phys. Rev. B* **46**, 12675 (1992).
- [71] J. G. Amar, and F. Family, *Phys. Rev. Lett.* **74**, 2066 (1995).
- [72] J. W. Cahn, *J. Chem. Phys.* **42**, 93 (1965).
- [73] T. A. Witten, and L. M. Sander, *Phys. Rev. Lett.* **47**, 1400 (1981).
- [74] S. Sun, and C. B. Murray, *J. Appl. Phys.* **85**, 4325 (1999).
- [75] C. B. Murray, C. R. Kagan, M. G. Bawendi, *Annu. Rev. Mater. Sci.* **30**, 545 (2000).
- [76] J. A. Stroschio, and D. T. Pierce, *Phys. Rev. B* **49**, 8522 (1994).
- [77] V. Sofonea, and K. R. Mecke, *Eur. Phys. J. B* **8**, 99 (1999).
- [78] P. Meakin, *Phys. Rev. Lett.* **51**, 1119 (1983).
- [79] M. Kolb, R. Botet, and R. Jullien, *Phys. Rev. Lett.* **51**, 1123 (1983).
- [80] R.J. Birgeneau and P. M. Horn, *Science* **232**, 329 (1986).
- [81] K. K. Likharev, *Proc. IEEE* **87**, 606 (1999).
- [82] R. B. Laibowitz, and P. J. Stiles, *Appl. Phys. Lett.* **18**, 267 (1971).

- [83] K. Yano, T. Ishii, T. Hashimoto, T. Kobayashi, F. Murai, K. Seki, *IEEE Trans. Electron Devices* **41**, 1628 (1994).
- [84] L. Guo, E. Leobandung, and S. Y. Chou, *Science* **275**, 649 (1997).
- [85] S. Tiwari, F. Rana, H. Hanafi, A. Hartstein, E. F. Crabbe, and K. Chan, *Appl. Phys. Lett.* **68**, 1377 (1996).
- [86] L. Ma, S. Pyo, J. Ouyang, Q. Xu, and Y. Yang, *Appl. Phys. Lett.* **82**, 1419 (2003).
- [87] J. Ouyang, C. W. Chu, D. Sieves, and Y. Yang, *Appl. Phys. Lett.* **86**, 123507 (2005).
- [88] J. H. Jung, J. Y. Jin, I. Lee, T. W. Kim, H. G. Roh, and Y. H. Kim, *Appl. Phys. Lett.* **88**, 112107 (2006).
- [89] F. Li, D. I. Son, J. H. Ham, B. J. Kim, J. H. Jung, and T. W. Kim, *Appl. Phys. Lett.* **91**, 162109 (2007).
- [90] D. L. Klein, P. L. McEuen, J. E. Bowen Katari, R. Roth, and A. P. Alivisatos, *Appl. Phys. Lett.* **68**, 2574 (1996).
- [91] D. L. Klein, R. Roth, A. K. L. Lim, A. P. Alivisatos, and P. L. McEuen, *Nature* **389**, 699 (1997).
- [92] R. Parthasarathy, X. M. Lin, K. Elteto, T. F. Rosenbaum, and H. M. Jaeger, *Phys. Rev. Lett.* **92**, 076801 (2004).
- [93] H. R. Romero, and M. Drndic, *Phys. Rev. Lett.* **95**, 156801 (2005).
- [94] C. P. Li, C. H. Wu, K. H. Wei, J. T. Sheu, J. Y. Huang, U. S. Jeng, and K. S. Liang, *Adv. Funct. Mater.* **17**, 2283 (2007).
- [95] R. Wilkins, E. Ben-Jacob, and R. C. Jaklevic, *Phys. Rev. Lett.* **63**, 801 (1989).
- [96] R. P. Andres, T. Bein, M. Dorogi, S. Feng, J. I. Henderson, C. P. Kubiak, W. Mahoney, R. G. Osifchin, and R. Reifenberger, *Science* **272**, 1323 (1996).
- [97] W. H. Press, B. P. Flannery, S. A. Teukolsky, and W. T. Vetterling, *Numerical Recipes.*, New York: Cambridge University Press, p.523 (1986).

- [98] M. Amman, R. Wilkins, E. Ben-Jacob, P. D. Maker, and R. C. Jaklevic, *Phys. Rev. B* **43**, 1146 (1991).
- [99] L. Wang, M. E. Taylor, and M. E. Welland, *Surf. Sci.* **322**, 325 (1995).
- [100] C. A. Leatherdale, and M. G. Bawendi, *Phys. Rev. B* **63**, 165315 (2001).
- [101] S. A. Blanton, R. L. Leheny, M. A. Hines, and P. Guyot-Sionnest, *Phys. Rev. Lett.* **79**, 865 (1997).
- [102] I. Giaever and H. R. Zeller, *Phys. Rev. Lett.* **20**, 1504 (1968).
- [103] M. Kardar, G. Parisi, and Y. C. Zhang, *Phys. Rev. Lett.* **56**, 889 (1986).
- [104] G. A. Prinz, *Science* **282**, 1660 (1998).
- [105] M. N. Baibich, J. M. Broto, A. Fert, F. Nguyen Van Dau, F. Petroff, P. Eitenne, G. Creuzet, A. Friederich, and J. Chazelas, *Phys. Rev. Lett.* **61**, 2472 (1988).
- [106] G. Binasch, P. Grünberg, F. Saurenbach, and W. Zinn, *Phys. Rev. B* **39**, 4828 (1989).
- [107] J. S. Moodera, L. R. Kinder, T. M. Wong, and R. Meservey, *Phys. Rev. Lett.* **74**, 3273 (1995).
- [108] B. Dieny, V. S. Speriosu, S. S. P. Parkin, B. A. Gurney, D. R. Wilhoit, and D. Mauri, *Phys. Rev. B* **43**, 1297 (1991).
- [109] J. K. Furdyna, *J. Appl. Phys.* **64**, R29 (1988).
- [110] H. Ohno, *Science* **281**, 951 (1998).
- [111] T. Story, R. R. Galazka, R. B. Frankel, and P. A. Wolff, *Phys. Rev. Lett.* **56**, 777 (1986).
- [112] M. Sawicki, T. Dietl, J. Kossut, J. Igalson, T. Wojtowicz, and W. Plesiewicz, *Phys. Rev. Lett.* **56**, 508 (1986).
- [113] H. Ohno, A. Shen, F. Matsukura, A. Oiwa, A. Endo, S. Katsumoto, and Y. Iye, *Appl. Phys. Lett.* **69**, 363 (1996).
- [114] T. Hayashi, H. Shimada, H. Shimizu, and M. Tanaka, *J. Cryst. Growth* **201/202**,

689 (1999).

- [115] Y. Ohno, D. K. Young, B. Beschoten, F. Matsukura, H. Ohno, and D. D. Awschalom, *Nature* **402**, 790 (1999).
- [116] H. Ohno, D. Chiba, F. Matsukura, T. Omiya, E. Abe, T. Dietl, Y. Ohno, and K. Ohtani, *Nature* **408**, 944 (2000).
- [117] D. Chiba, M. Yamanouchi, F. Matsukura, and H. Ohno, *Science* **301**, 943 (2003).
- [118] M. Yamanouchi, D. Chiba, F. Matsukura, and H. Ohno, *Nature* **428**, 539 (2004).
- [119] Y. Matsumoto, M. Murakami, T. Shono, T. Hasegawa, T. Fukumura, M. Kawasaki, P. Ahmet, T. Chikyow, S. Koshihara, and H. Koinuma, *Science* **291**, 854 (2001).
- [120] T. Toyosaki, T. Fukumura, Y. Yamada, K. Nakajima, T. Chikyow, T. Hasegawa, H. Koinuma, and M. Kawasaki, *Nat. Mater.* **3**, 221 (2004).
- [121] S. Cho, S. Choi, G. B. Cha, S. C. Hong, Y. Kim, Y. J. Zhao, A. J. Freeman, J. B. Ketterson, B. J. Kim, Y. C. Kim, and B. C. Choi, *Phys. Rev. Lett.* **88**, 257203 (2002).
- [122] R. Janisch, P. Gopal, and N. A. Spaldin, *J. Phys. Condens. Mater.* **17**, R657 (2005).
- [123] C. Klingshirn, *Chem. Phys. Chem.* **8**, 782 (2007).
- [124] S. J. Pearton, D. P. Norton, K. Ip, Y. W. Heo, and T. Steiner, *J. Vac. Sci. Technol. B* **22**, 932 (2004).
- [125] S. Lany and A. Zunger, *Phys. Rev. B* **72**, 035215 (2005).
- [126] D. C. Look, J. W. Hemsky, and J. R. Sizelove, *Phys. Rev. Lett.* **82**, 2552 (1999).
- [127] D. C. Look, G. C. Farlow, P. Reunchan, S. Limpijumnong, S. B. Zhang, K. Nordlund, *Phys. Rev. Lett.* **95**, 225502 (2005).
- [128] S. Lany and A. Zunger, *Phys. Rev. Lett.* **98**, 045501 (2007).
- [129] C. G. Van de Walle, *Phys. Rev. Lett.* **85**, 1012 (2000).

- [130] J. R. Neal, A. J. Behan, R. M. Ibrahim, H. J. Blythe, M. Ziese, A. M. Fox, and G. A. Gehring, *Phys. Rev. Lett.* **96**, 197208 (2006).
- [131] Z. H. Zhang, X. Wang, J. B. Xu, S. Muller, C. Ronning, and Q. Li, *Nat. Nanotechnol.* **4**, 523 (2009).
- [132] A. J. Behan, A. Mokhtari, H. J. Blythe, D. Score, X. H. Xu, J. R. Neal, A. M. Fox, and G. A. Gehring, *Phys. Rev. Lett.* **100**, 047206 (2008).
- [133] Q. Xu, L. Hartmann, S. Zhou, A. Mcklich, M. Helm, G. Biehne, H. Hochmuth, M. Lorenz, M. Grundmann, and H. Schmidt, *Phys. Rev. Lett.* **101**, 076601 (2008).
- [134] A. S. Risbud, N. A. Spaldin, Z. Q. Chen, S. Stemmer, and R. Seshadri, *Phys. Rev. B* **68**, 205202 (2003).
- [135] C. P. Bean, and J. D. Livingston, *J. Appl. Phys.* **30**, 120S (1959).
- [136] M. E. McHenry, S. A. Majetich, J. O. Artman, M. DeGraef, and S. W. Staley, *Phys. Rev. B* **49**, 11358 (1994).
- [137] B. D. Cullity. *Introduction to Magnetic Materials*. Addison-Wesley, London, 1972.
- [138] H. Akai, *Phys. Rev. Lett.* **81**, 3002 (1998).
- [139] M. Berciu and R. N. Bhatt, *Phys. Rev. Lett.* **87**, 107203 (2001).
- [140] A. C. Durst, R. N. Bhatt, and P. A. Wolff, *Phys. Rev. Lett.* **65**, 235205 (2002).
- [141] Y. Henry, K. Ounadjela, L. Piraux, S. Dubois, J. M. George, and J. L. Duvail, *Eur. Phys. J. B* **20**, 35 (2001).
- [142] A. Schwarz and R. Wiesendanger, *Nanotoday* **3**, 28 (2008).
- [143] D. G. Ramlan, S. J. May, J. G. Zheng, J. E. Allen, B. W. Wessels, and L. J. Lanhon, *Nano. Lett.* **6**, 50 (2006).

Curriculum vitae

Personal data

Name: 歐逸青 (Yi-Ching Ou)

Birthday: April 7, 1978 at Changhua, Taiwan.

Education

- 2006/9 ~ 2011/1 Ph.D.
in Institute of Physics, National Chiao Tung University, Hsinchu, Taiwan.
- 2004/9 ~ 2006/7 Master
in Institute of Physics, National Chiao Tung University, Hsinchu, Taiwan.
- 1996/9 ~ 2000/6 Bachelor
in Department of Engineering and System Science, National Tsing Hua University, Hsinchu, Taiwan.



Publications List

1. Yi-Ching Ou, Konstantin S. Zhuravlev, Jiye Fang, and Wen-Bin Jian, Interplay of Spinodal and Diffusion-Limited Aggregation in Formation of Nanocrystal Assembled Two-Dimensional Islands, *J. Phys. Chem. C*, **114**, 17416 (2010).
2. Yi-Ching Ou, Zhong-Yi Wu, Fu-Rong Chen, Ji-Jung Kai and Wen-Bin Jian, Characterization of Room-Temperature Ferromagnetic $Zn_{1-x}Co_xO$ Nanowires, **Nanowires, Paola Prete (Ed.), ISBN: 978-953-7619-79-4, INTECH, 2010.**
3. Yi-Ching Ou, Song-Fun Cheng, and Wen-Bin Jian, Size dependence in tunneling spectra of PbSe quantum-dot arrays, *Nanotechnology* **20**, 285401 (2009).
4. Yi-Ching Ou, Jiun-Ji Wu, Jiye Fang, and Wen-Bin Jian, Probing Capacitive Coupling and Collective Transport in PbSe Quantum-Dot Arrays Using Scanning Tunneling Spectroscopy, *J. Phys. Chem. C* **113**, 7887 (2009). Cover Art of Issue 18 of JPC C (May 7, 2009).

5. I-Jan Chen, Yi-Ching Ou, Zhong-Yi Wu, Fu-Rong Chen, Ji-Jung Kai, Juhn-Jong Lin, and Wen-Bin Jian, Size Effects on Thermal Treatment and Room-Temperature Ferromagnetism in High-Vacuum Annealed ZnCoO Nanowires, *J. Phys. Chem. C* **112**, 9168 (2008).
6. Wen-Bin Jian, I-Jan Chen, Tai-Ching Liao, Yi-Ching Ou, Cheng-Hsun Nien, Zhong-Yi Wu, Fu-Rong Chen, Ji-Jung Kai, and Juhn-Jong Lin, Size dependent magnetization and high-vacuum annealing enhanced ferromagnetism in $Zn_{1-x}Co_xO$ nanowires, *J. Nanosci. Nanotechnol.* **8**, 202 (2008).

